Carbon nanostructures for femtosecond mode-locked lasers in the 1.0 to 2.1 micrometer wavelength range

DISSERTATION

zur Erlangung des akademischen Grades

DOCTOR RERUM NATURALIUM

(Dr. rer. nat.)

im Fach Physik

eingereicht an der

Mathematisch-Naturwissenschaftlichen Fakultät

der Humboldt-Universität zu Berlin

von

M.-Eng. Andreas Schmidt

Präsident der Humboldt-Universität zu Berlin

Prof. Dr. Jan-Hendrik Olbertz

Dekan der Mathematisch-Naturwissenschaftlichen Fakultät

Prof. Dr. Elmar Kulke

Gutachter:
1. Prof. Dr. Valdas Pasiskevicius
2. Prof. Dr. Thomas Elssser
3. Prof. Dr. Oliver Benson

Tag der mündlichen Prüfung: 03. November 2015

During the course of this work, the following publications have been communicated.

[1] V. Jambunathan, A. Schmidt, X. Mateos, M. C. Pujol, U. Griebner, V. Petrov, C. Zaldo, M. Aguiló, and F. Díaz. Crystal growth, optical spectroscopy, and continuous-wave laser operation of co-doped (ho,tm):klu(wo4)2 monoclinic crystals. *J. Opt. Soc. Am. B*, 31(7):1415–1421, Jul 2014

[2] S. D. Di Dio Cafiso, E. Ugolotti, A. Schmidt, V. Petrov, U. Griebner, A. Agnesi, W. B. Cho, B. H. Jung, F. Rotermund, S. Bae, B. H. Hong, G. Reali, and F. Pirzio. Sub-100-fs cr:yag laser mode-locked by monolayer graphene saturable absorber. *Opt. Lett.*, 38(10):1745–1747, 2013

[3] S D Di Dio Cafiso, E Ugolotti, A Schmidt, V Petrov, U Griebner, A Agnesi, W B Cho, Y G Zhang, S Y Choi, F Rotermund, G Reali, and F Pirzio. Sub-50 fs mode-locking of a Cr:YAG laser using an SWCNT-SA. *Laser Physics Letters*, 10(8):085801, 2013

[4] A. Schmidt, P. Koopmann, G. Huber, P. Fuhrberg, S. Y. Choi, D.-I. Yeom, F. Rotermund, V. Petrov, and U. Griebner. 175 fs $Tm:Lu_2o_3$ laser at 2.07 µm mode-locked using single-walled carbon nanotubes. *Opt. Express*, 20(5):5313–5318, 2012

[5] F. Rotermund, W. B. Cho, S. Y. Choi, I. H. Baek, J. H. Yim, S. Lee, A. Schmidt, G. Steinmeyer, U. Griebner, D. I. Yeom, K. Kim, and V. Petrov. Mode-locking of solid-state lasers by single-walled carbon-nanotube based saturable absorbers. *Quantum Electronics*, 42(8):663, 2012

[6] E. Ugolotti, A. Schmidt, V. Petrov, Jun Wan Kim, D.-I. Yeom, F. Rotermund, Sukang Bae, Byung Hee Hong, A. Agnesi, Christian Fiebig, Götz Erbert, Xavier Mateos, Magdalena Aguiló, Francesc Diaz, and U. Griebner. Graphene mode-locked femtosecond Yb:KLuW laser. *Applied Physics Letters*, 101(16):161112, 2012

[7] A. Schmidt, S. Y. Choi, D.-I. Yeom, F. Rotermund, Xavier Mateos, Martha Segura, Francesc Diaz, Valentin Petrov, and U. Griebner. Femtosecond pulses near 2 µm from a Tm:KLuW laser mode-locked by a single-walled carbon nanotube saturable absorber. *Applied Physics Express*, 5(9):092704, 2012

[8] X. Mateos, M. Segura, W. B. Cho, A. Schmidt, F. Rotermund, M. C. Pujol, J. J. Carvajal, M. Aguilo, F. Diaz, V. Panyutin, U. Griebner, and V. Petrov. Pulsed 2-micron lasers based on Tm^{3+}-doped monoclinic double tungstate crystals. *Proc. SPIE*, 8039:803902–803902–9, 2011

[9] V. Jambunathan, A. Schmidt, X. Mateos, M. C. Pujol, J. J. Carvajal, M. Aguiló, F. Díaz, U. Griebner, and V. Petrov. Continuous-wave co-lasing in a monoclinic co-doped (Ho,Tm):$KLu(WO_4)_2$ crystal. *Laser Physics Letters*, 8(11):799, 2011

[10] A. Yoshida, A. Schmidt, V. Petrov, C. Fiebig, G. Erbert, J. Liu, H. Zhang, J. Wang, and U. Griebner. Diode-pumped mode-locked yb:ycob laser generating 35 fs pulses. *Opt. Lett.*, 36(22):4425–4427, 2011

[11] V. Petrov, X. Mateos, A. Schmidt, S. Rivier, U. Griebner, H. Zhang, J. Wang, J. Li, and J. Liu. Passive mode-locking of acentric yb-doped borate crystals. *Laser Physics*, 20(5):1085–1090, 2010

[12] J. J. Carvajal, G. Ciatto, X. Mateos, A. Schmidt, U. Griebner, V. Petrov, G. Boulon, A. Brenier, A. Pe na, M. C. Pujol, M. Aguiló, and F. Díaz. Broad emission band of yb3+ in the nonlinear nb:rbtiopo4 crystal: origin and applications. *Opt. Express*, 18(7):7228–7242, Mar 2010

[13] W. B. Cho, A. Schmidt, S. Y. Choi, V. Petrov, U. Griebner, G. Steinmeyer, S. Lee, D.-I. Yeom, and F. Rotermund. Mode locking of a Cr:YAG laser with carbon nanotubes. *Opt. Lett.*, 35(16):2669–2671, 2010

[14] A. Schmidt, V. Petrov, U. Griebner, R. Peters, K. Petermann, G. Huber, C. Fiebig, K. Paschke, and G. Erbert. Diode-pumped mode-locked yb:lusco3 single crystal laser with 74 fs pulse duration. *Opt. Lett.*, 35(4):511–513, Feb 2010

[15] W. B. Cho, J. H. Yim, S. Y. Choi, S. Lee, A. Schmidt, G. Steinmeyer, U. Griebner, V. Petrov, D.-I. Yeom, K. Kim, and F. Rotermund. Boosting the non linear optical response of carbon nanotube saturable absorbers for broadband mode-locking of bulk lasers. *Advanced Functional Materials*, 20(12):1937–1943, 2010

[16] A. Schmidt, S Rivier, V Petrov, U Griebner, G Erbert, A Gross, V Wesemann, S Vernay, and D Rytz. 65 fs diode-pumped diffusion-bonded Yb:$KY(WO_4)_2$/$KY(WO_4)_2$ laser. *Electronics letters*, 46(9):641–643, 2010

[17] A. Yoshida, A. Schmidt and H. Zhang, J. Wang, J. Liu, C. Fiebig, K. Paschke, G. Erbert, V. Petrov, and U. Griebner. 42-fs diode-pumped yb:ca4yo(bo3)3 oscillator. *Opt. Express*, 18(23):24325–24330, Nov 2010

[18] W. B. Cho, A. Schmidt, J. H. Yim, S. Y. Choi, S. Lee, F. Rotermund, U. Griebner, G. Steinmeyer, V. Petrov, X. Mateos, M. C. Pujol, J. J. Carvajal, M. Aguiló, and F. Díaz. Passive mode-locking of a Tm-doped bulk laser near 2 µmusing a carbon nanotube saturable absorber. *Opt. Express*, 17(13):11007–11012, 2009

[19] A. Schmidt, S. Rivier, W. B. Cho, J. H. Yim, S. Y. Choi, S. Lee, F. Rotermund, D. Rytz, G. Steinmeyer, V. Petrov, and U. Griebner. Sub-100 fs single-walled carbon nanotube saturable absorber mode-locked Yb-laser operation near 1 μm. *Opt. Express*, 17(22):20109–20116, 2009

[20] A. Schmidt, U. Griebner, H. Zhang, J. Wang, M. Jiang, J. Liu, and V. Petrov. Passive mode-locking of the yb: Cngg laser. *Optics Communications*, 283(4):567–569, 2010

[21] A. Schmidt, S. Rivier, G. Steinmeyer, J. H. Yim, W. B. Cho, S. Lee, F. Rotermund, M. C. Pujol, X. Mateos, M. Aguiló, F. Díaz, V. Petrov, and U. Griebner. Passive mode locking of Yb:KLuW using a single-walled carbon nanotube saturable absorber. *Opt. Lett.*, 33(7):729–731, 2008

Contents

Chapter 1

Motivation

During the last two decades ultrashort laser pulses have become an irreplaceable tool in industry, medicine and basic research. By means of nonlinear frequency conversion, their emission covers a broad range of available wavelengths from the deep vacuum ultraviolet below 200 nm [1] into the terahertz region at wavelengths up to 1000 µm [2]. Each of the laser parameters has been driven to the extreme, be it the pulse duration short than 2 cycles of the electric field [3], stability (e.g., carrier envelope phase- [4] or frequency stability [5]), peak power [6] or repetition rate [7]. The main part of the pulsed laser sources are seeded by mode-locked oscillators. The latter rely on either the nonlinear Kerr effect or an optical element, *e.g.*, a saturable absorber (SA), to initiate and maintain pulsed operation.

Commonly semiconductor saturable absorber mirrors (SESAMs, [8]) are used to mode-lock different laser types. Despite their proven suitability for mode-locking, they need to be specifically designed, and their applicability is limited to the designed wavelength range. Their production requires sophisticated processes, and an additional post-processing is essential to obtain applicable relaxation times. Due to their layout, SESAMS are commonly incorporated at one end of a linear laser cavity, with a fixed beam spot size on the absorber defined by resonator geometry.

Single-walled carbon nanotubes (SWCNTs) and graphene are carbon nanosystems which display an ultrafast third order susceptibility, classifying them as potential candidates for mode-locking. Fiber lasers represent the first laser types successfully mode-locked using SAs based on carbon nanostructures [9, 10]. The samples may introduce non-saturable losses exceeding 15 %, which are, however, tolerated by fiber lasers [11].

Such high losses are intolerable for operation of bulk solid state lasers, in particular for quasi three-level lasers, *e.g.*, lasers exploiting the Yb^{3+} laser active ion, the unrivaled laser dopant for high-power ultrashort pulse generation around 1.0 µm.

Hence, the question arose whether tailoring carbon nanostructure SAs for operation in bulk lasers is possible, and whether those novel mode-lockers are a match to SESAMs. In first place, mimicking SESAMs was not the main goal, but exploiting similar physical processes, and intrinsic differences between carbon nanostructure SAs and SESAMs, to obtain the best mode-locking performance possible.

In this thesis, the physical processes underling mode-locking with carbon nanosystems, in particular nanotubes and graphene, are studied in a wide range of operation conditions of solid-state lasers.

The saturable absorbers based on SWCNTs and graphene are compared to each other in the context of operation in one wavelength region, considering their specific parameters. Furthermore, SWCNT and graphene-SAs feature a spectrally broadband applicability which is discussed as well.

After this motivation, the thesis introduces the carbon nanostructures under study with focus on their optical properties. In the third chapter, the ultrafast relaxation, as well as saturation processes of SWCNT and graphene SAs are discussed, and the assessment of their parameters is outlined. This chapter finally touches on similarities to SESAMS. Chapter 4 is dedicated to the generation of ultrashort laser pulses, the processes involved, their mathematical description and possible obstacles of laser operation. In chapter 5 the experimental results are presented, including the absorber characterization and some of the first applications of carbon nanostructures in mode-locked bulk lasers. The chapter is split into results obtained with SWCNT-SAs and graphene-SAs. The discussion of the laser results completes the chapter, and chapter 6 finally concludes this work listing its highlights.

Chapter 2

Carbon nanostructures

Carbon research experienced several boosts by the discovery of unique carbon based structures. The so-called bucky balls are spherical compounds composed of at least 20 carbon atoms with C_{60} being their most popular representative. Since their discovery in 1985 [12] they have inspired almost 22 000 publications in this field[1]. C_{60} fullerene research was honored with the Nobel prize in chemistry, awarded to Sir Harold Walter Kroto, Robert Curl and Richard Smalley in 1996. Another key step in carbon research was the discovery of SWCNTs in 1993 by Ijiima *et al.* [13].

Graphene, under study since 1947 [14–16], is the most recently synthesized carbon structure. It is closely related to the former two and the groundbreaking research on this unique material was honored with the Nobel prize in physics 2010 to Andre Geim and Konstantin Novoselov.

SWCNTs and graphene show saturable absorption suitable for mode-locking, *i.e.*, they are a potential replacement for ultrafast SESAMs. While SESAMs demand challenging and expensive fabrication processes like metal organic chemical vapor deposition, metal organic phase vapor epitaxy, or molecular beam epitaxy, fabrication of SWCNT and graphene SAs is simple in comparison.

Graphene's intrinsic broadband absorption is applicable over a wide wavelength range from the ultraviolet (UV) into the far infrared spectral region [17–20]. The absorption band of SWCNTs is controllable by varying the tube diameter defined by their chirality. SWCNT-SAs may be modified to be applicable over a broad range of wavelengths as well, boosting their versatility.

This chapter introduces carbon nanostructures and focuses on graphene and SWCNTs. Starting from the band structure, different effects altering the absorption features are introduced and compared to optical transmission measurements.

[1] According to the search via www.sciencedirect.com

2.1 Classification and description

Nanostructures may be classified according to their dimensionality. In the case of carbon-based nanostructures it is possible to distinguish 0D quantum dots and fullerenes, 1D quantum wires and nanotubes, the 2D graphene, and finally 3D stacks of graphene known as graphite. In this work the 1D and 2D structures graphene and SWCNTs as well as their suitability for mode-locking are studied in detail.

Graphene is a 2D monolayer of carbon atoms arranged in a benzene-ring structure (honeycomb structure), wherein each carbon atom is bound to its three neighbouring carbon atoms by a σ-bond formed by the combination of p_x and p_y orbitals mixing into the sp^2 hybrid orbital. The remaining p_z orbitals are oriented out of plane, hybridizing to the π-band and the π^*-band. The latter are the reason for most of graphene's electric properties.

Graphene is said to be a semi-metal, because it was demonstrated that charge carriers in graphene mimic massless Dirac fermions [21, 22] with Fermi velocities on the order of those found in metals ($\approx 10^6\,\mathrm{m{\cdot}s^{-1}}$). Graphene monolayer extraction from graphite, was first shown by Novoselov *et al.* in 2004 [23, 24] and this carbon allotrope may be regarded as source material for all other carbon nanostructures as illustrated in figure 2.1 [25].

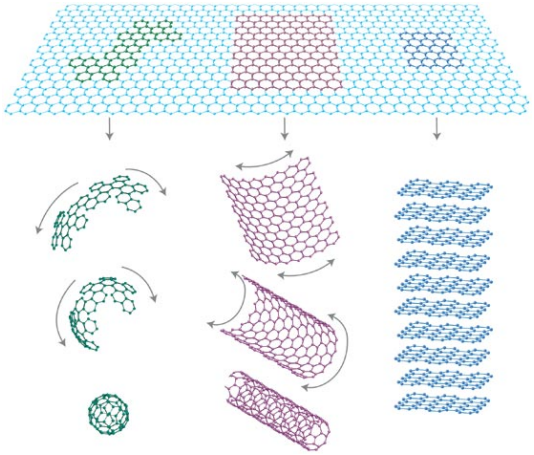

Figure 2.1: *Theoretical construction of fullerenes, SWCNTs, and graphite (bottom, from left to right) from graphene (top), which may be understood as a basis structure for the three carbon nanostructures. Figure from [25]*

SWCNTs may be understood as a rolled up sheet of graphene. This picture is actually only a helpful visualization, as, *e.g.*, during SWCNT growth by CVD using a catalyst, SWCNTs grow directly as a tube from the catalyst [26] without graphene as key precursor. In this work, the term 'nanotube' refers solely to the single-walled representatives of carbon nanotubes with a diameter of several nanometers and a length of some µm.

2.2 Graphene

2.2.1 Bandstructure and Density of States

Graphene behaves like a zero-gap semiconductor, and the electronic structure of a perfect single layer of graphene can be calculated by the tight binding model resulting in the 2D energy dispersion [27]

$$E^{\pm}_{\mathrm{g2D}}(\mathbf{k}) = \frac{\epsilon_{2\mathrm{p}} \pm t\omega(\mathbf{k})}{1 \mp s\omega(\mathbf{k})} \; . \tag{2.1}$$

Here, s describes the overlap of the electronic wave functions, t is the nearest neighbor hopping integral, and $\epsilon_{2\mathrm{p}}$ the site energy of the 2p orbital. E^{+} and E^{-} correspond to the π^{*} and π energy bands, respectively. Figure 2.3 shows the energy dispersion relation of graphene and the high symmetry points in k-space. The function

$$\omega(\mathbf{k}) = \sqrt{1 + 4\cos\frac{\sqrt{3}k_{\mathrm{x}}a}{2}\cos\frac{k_{\mathrm{y}}a}{2} + 4\cos^2\frac{k_{\mathrm{y}}a}{2}} \tag{2.2}$$

is used, and $t = 3.013\,\mathrm{eV}$, $s = 0.129$ and $\epsilon_{2\mathrm{p}} = 0$ are assumed for calculating the electronic structure of graphene as a function of the 2D wave vector $\mathbf{k} = \binom{k_{\mathrm{x}}}{k_{\mathrm{y}}}$. The conduction and the valence band touch each other at the six K- and K′-points in the reciprocal lattice of k-space. Close to the K and K′-points $E^{\pm}_{\mathrm{g2D}}(\mathbf{k})$ can be approximated linearly and is represented by two opposing cones [18, 27]

$$E(k) \approx \frac{\pm 3t\mathbf{k}a}{2} \; . \tag{2.3}$$

Here a is the carbon-to-carbon distance of 1.42 Å. This approximation is valid for low energies of $\mathrm{E} < 3\,\mathrm{eV}$ [27]. This linear behavior has been predicted [14, 28] and proven experimentally [22, 23]. Considering that the Fermi velocity is given by [29]

$$v_{\mathrm{F}} = \frac{\sqrt{3}ta}{2\hbar} \; , \tag{2.4}$$

it is possible to express the energy dispersion in graphene by

$$E(k) \approx \frac{\pm 3tka}{2} = \pm\frac{1}{\sqrt{3}}\hbar v_{\mathrm{F}}k \; . \tag{2.5}$$

This conical band structure demonstrates the character of charge carriers in graphene to behave like massless Dirac fermions traveling at a constant speed independent on their energy. The Fermi velocity in graphene is $v_{\mathrm{F}} \approx 10^{6}$ m/s [29, 30] and the

metallic character of graphene originates from the fact that its Fermi velocity is on the same order of magnitude as in metals.

Graphene's energy dispersion, approximated by equation (2.3), is used to calculate its **density of states** (DOS; states per graphene unit cell), which reads

$$g(E) = \frac{4}{3\sqrt{3}\pi}\frac{1}{t^2}E \ . \tag{2.6}$$

Equation (2.6) shows a linear dependence on the energy, *i.e.*, the number of electronic states increases linearly with energy, whereas approaching the K- and K'-points, the number of available states converges to zero.

2.2.2 Linear transmission

At energies below 3 eV, graphene shows an almost uniform broadband absorption. In reference [18] the absorption is deduced from the real part of the frequency-dependent optical conductivity $\sigma(\omega)$ and for a free standing graphene sheet under normal incidence in between two media, the transmission is given by [18]

$$T = \sqrt{\frac{\epsilon_2}{\epsilon_1}}\frac{4(\epsilon_1\epsilon_0)^2}{\left|(\sqrt{\epsilon_1\epsilon_2}+\epsilon_1)\epsilon_0+\sqrt{\epsilon_1}\sigma(\omega)/c\right|^2} \ , \tag{2.7}$$

with the electric permittivities $\epsilon_1\epsilon_0$ and $\epsilon_2\epsilon_0$ describing the surrounding media and the speed of light c. Equation (2.7) can be further simplified if vacuum is assumed and the frequency dependence of the optical conductivity $\sigma(\omega)$ is neglected, *i.e.*, $\sigma(\omega) \approx \sigma_0 = \frac{\pi e^2}{2h} = \frac{e^2}{4\hbar}$. Thus, the transmission is given by

$$T = \frac{1}{\left|1+\pi\cdot\alpha+\frac{\pi^2}{4}\cdot\alpha^2\right|} = \frac{1}{\left(1+\frac{\pi}{2}\cdot\alpha\right)^2} \approx 1-\pi\alpha \ , \tag{2.8}$$

using the fine structure constant $\alpha = \frac{e^2}{2\epsilon_0 ch} = \frac{e^2}{4\epsilon_0 c\hbar\pi} \approx 137^{-1}$ and a power series expansion of $\pi\alpha/2$ around 0. In figure 2.2 the calculated transmission according to equation (2.7) and the approximated transmission of equation (2.8) are plotted versus wavelength. The nearest neighbor hopping integral was set to $t = 3.1$ eV and the chemical potential to $\mu = 0.1\,eV$ or $\mu = 0.2\,eV$, respectively.

The comparison of the measured transmission of the single-layer graphene sample already shows a good agreement with the approximation. Within the wavelength range of interest between 1 and 2.1 µm, marked by the vertical gray lines and indicated by the double-headed arrow, the deviation of the transmission from calculations [equations (2.7) and (2.8)] is less than 0.3%.

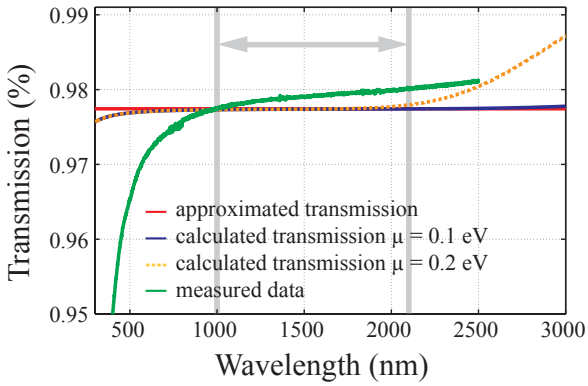

Figure 2.2: *The calculated transmission of graphene according to equation 2.7 (blue and dashed orange) for two chemical potentials and the approximated transmission in accordance with equation 2.8(red), the green curve represents the measured transmission of the single-layer graphene sample and the gray lines and the arrow indicate the wavelength range of interest (1-2.1 µm).*

The curve shape of the measured transmission is only approximately described by the model of equation (2.7) taking a chemical potential $\mu \neq 0\,\mathrm{eV}$ into account. In the following a physical model is introduced that improves the agreement of measurement and theory.

The Fano resonance of graphene

The optical conductivity of graphene shows a van Hove singularity (vHs) [31] due to the saddle point of the energy dispersion (*cf.* figure 2.3). This vHs is applicable for describing the transmission of graphene below 500 nm [32, 33], as it is located at UV wavelengths of about 250 nm [34, 35], being additionally redshifted [19, 36] due to the generation of excitons. These excitons display a binding energy of 400 - 600 meV, by which the energy of the direct interband transition calculated in the single particle picture is decreased [36, 37].

At graphene's saddle point M, the excitonic resonance couples with a continuum of states, which is formed by the band from the M to the K-Point. Figure 2.3 illustrates this continuum (red line) and the excitonic resonance (initial and final energy indicated by the red dots). Compared to the energy dispersion in the single particle picture, which is represented by the surface plot, the excitonic resonance is located at lower energies.

The coupling of a discrete state to a continuum of states is known as Fano resonance, which is characterized by an asymmetric line shape [38, 39]. This Fano model may be applied to graphene's measured absorption line in the UV, and the

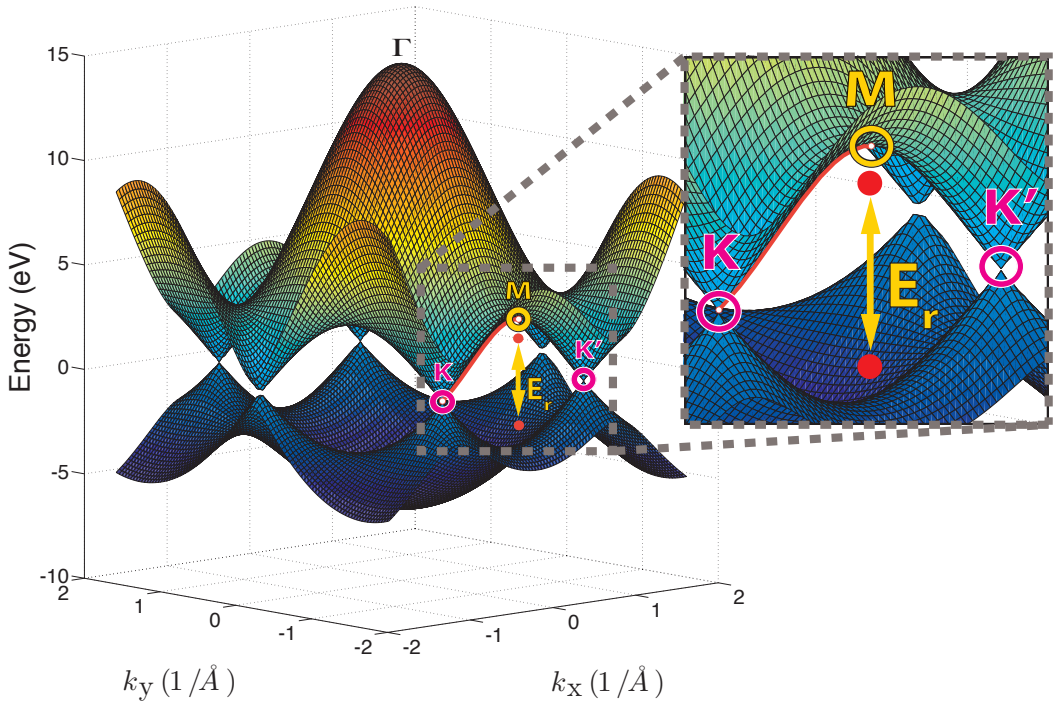

Figure 2.3: *Calculated energy dispersion relation for graphene for a single particle in the tight binding approach. The K and K'-points (magenta), the saddle point M (yellow) and the Γ point (black) are the high symmetry points in k-space. The red line illustrates the band forming the continuum that couples with the excitonic resonance (red dots). The transition energy E_r between the latter is approximately 400 - 600 meV smaller than the transition energy in the single-particle picture (i.e., the points are 200-300 meV below and above the conduction and valence band, respectively).*

fit excellently matches the measured data from the UV into the near-infrared (NIR) spectral region. The absorption is modeled by [37]

$$A_{\text{Fano}}(E) = C\left(1 + \frac{q^2-1}{1+s^2} + \frac{2qs}{1+s^2}\right) = C\frac{(s+q)^2}{1+s^2}, \text{ with } \quad s = 2\frac{E-E_r}{\gamma} \ . \tag{2.9}$$

The terms in equation (2.9) represent the constant continuum of states associated with the Dirac cones, the Lorentzian resonance of the vHs in the UV, and the coupling of the former two. The parameters are a scaling parameter C, the Fano parameter q, as well as the energy E_r and the width γ of the Lorentzian resonance.

Figure 2.4 shows the linear transmission of a graphene sample and the Fano fit to the data, which gives a very good agreement with the resonance and even describes graphene's transmission up to wavelengths of 2500 nm. The corresponding fitting parameters are $C = 0.3121$, $E_\text{r} = 4.9069\,\text{eV}$, $\gamma = 2.4978\,\text{eV}$ and a Fano parameter of $q = -5.3997$.

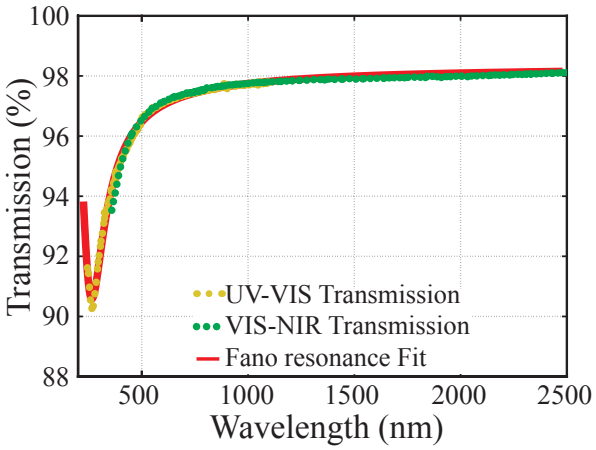

Figure 2.4: *Two separate transmission measurements of graphene in the UV-VIS (yellow-dotted) and VIS-NIR (green-dotted). Using equation* (2.9) *an excellent fit (red curve) is obtained, describing the UV behavior as well as the linear increase in the NIR.*

2.2.3 Layer number and optical quality

For the assessment of graphene's number of layers and its quality, Raman spectroscopy is the tool of choice. In Raman spectra of graphene the most striking features are the G and 2D band. The G-band, located at a Raman shift of about $1600\,\text{cm}^{-1}$ stems from the doubly degenerate phonon mode at the Brillouin zone center. This mode is composed of the in-plane longitudinal and transversal optical

phonon branches, and may be understood as vibrations of graphene's sublattices A and B against each other [40].

If two in-plane optical phonons are involved in the Raman scattering, the 2D band is detected. The D band occurs if an in-plane optical phonon and a defect are involved in the Raman scattering and its height is a measure of the number of defects in the graphene sample [41]. Even for a vanishing D-line peak the 2D-line peak is present, but its shape and bandwidth change with the graphene layer number [42, 43]. The ratio of the integrated G-line peak and the 2D-line peak is about 0.2 for a single layer of graphene [42].

Figure 2.5 shows the Raman spectrum of a graphene sample under study. The absence of the D-line peak indicates high sample quality (low defect density) and the shape of the 2D-line peak as well as the G to 2D ratio corroborate the presence of single layer graphene. The homogeneity of the sample is assessed by measurement of the peak ratio across the sample (inset).

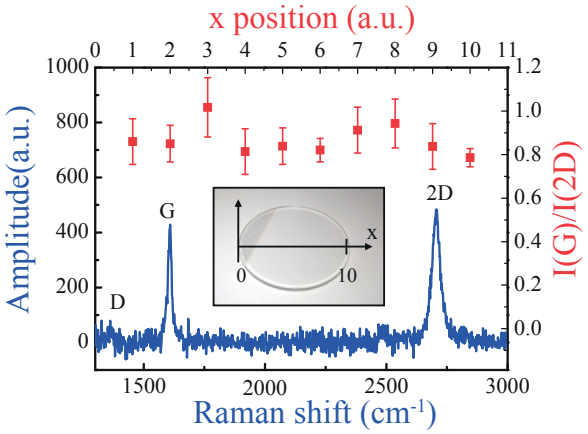

Figure 2.5: *Raman spectrum of the graphene-SA applied in this work. The G and 2D-line peaks are present, whereas the latter is the overtone of the D-line peak around 1350 cm^{-1}, whose absence indicates a negligible number of defects in the sample [42]. The ratio of the G and 2D-line peaks $\frac{I(\mathrm{G})}{I(\mathrm{2D})}$ indicates single layer coverage [42, 43] with a very good homogeneity (inset). Figure from reference [44].*

2.3 Single-walled carbon nanotubes

2.3.1 Bandstructure and Density of States

Figure 2.6(a) shows a graphene sheet, its unit vectors $\mathbf{a}_1$ and $\mathbf{a}_2$, the translation and chiral vectors $\mathbf{T}$ and $\mathbf{C_h}$ and an example of an (n,m)=(4,2) chiral vector. The chiral vector comprises the roll-up direction and the circumference of the nanotube, thus defining the structure of the nanotube completely, whereas $\mathbf{T}$ and $\mathbf{C}_h$ span a rectangle representing the nanotube unit cell of the 1D lattice.

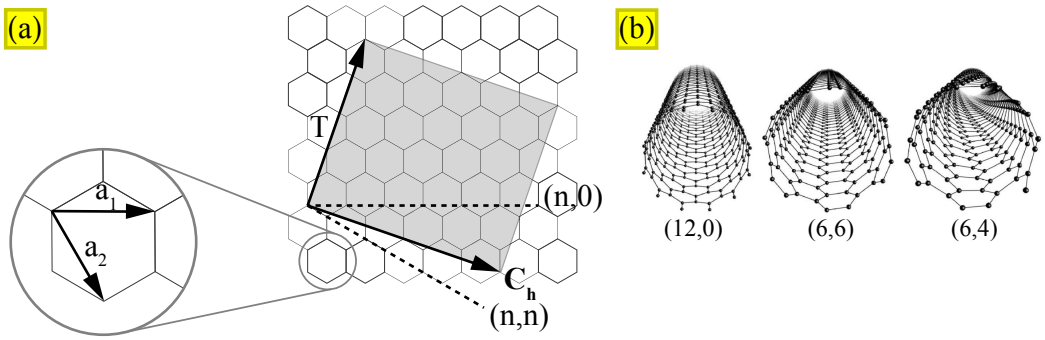

Figure 2.6: ***(a)*** *A schematic of a 2D graphene sheet and definitions of the lattice vectors showing the construction of a (n,m)=(4,2) nanotube. The limiting chiral case of a zigzag nanotube* $(n,0)$ *and armchair nanotube* (n,n) *are indicated by the dashed lines.* ***(b)*** *Structure of the three types of SWCNTs, showing a zigzag (12,0), armchair (6,6) and chiral (6,4) nanotube (from left to right). Figure from [45].*

There are basically the three types of nanotubes and those rolled up along the chiral vector with $(0,m)$ or $(n,0)$ are called zigzag nanotubes, SWCNTs rolled up along (n,n) are called armchair nanotubes and all other nanotubes are chiral nanotubes [figure 2.6(b)].

A nanotube with $n-m=3q$ and $q \in \mathbb{N}^0$ is metallic, whereas all nanotubes with $q \notin \mathbb{N}^0$ are semiconducting. Concerning metallic nanotubes, only armchair (n,n) nanotubes are truly always metallic, as nanotubes fulfilling $n-m=3l$ and $l \in \mathbb{N}$ have a tiny band-gap due to effects of the tube curvature [26, 45, 46]. The electronic structure of SWCNTs is derived starting from the electronic properties of graphene. The energy dispersion relations of a (n,m) SWCNT read [27]

$$E_\zeta^\pm(k) = E_{\mathrm{g2D}}^\pm(\mathbf{k}) \left(k\frac{\mathbf{K}_2}{|\mathbf{K}_2|} + \zeta \mathbf{K}_1 \right) , \tag{2.10}$$

with $\left(-\frac{\pi}{T} < k < \frac{\pi}{T} \text{ and } \zeta = 1, \cdots, N\right)$. In equation (2.10) the band structure of graphene [see equation (2.1)] is used. $T = \sqrt{3}\pi d_t/d_R$ represents the magnitude of

the translational vector $\mathbf{T}$, $N = 2(n^2 + m^2 + nm)/d_R$ is the number of hexagons within the SWCNT unit cell and $d_t = a\sqrt{n^2 + m^2 + nm}/\pi$ the nanotube diameter. The wave vector k is oriented along the nanotube axis.

The vectors $\mathbf{K}_1$ and $\mathbf{K}_2$ represent discrete unit wave vectors in k-space along the circumferential direction and along the nanotube axis, respectively [27]. This boundary condition results in N discrete $\mathbf{k}$ vectors and $2N$ energy dispersion curves according to equation (2.10). Those curves are obtained by cutting the energy dispersion surface of graphene (figure 2.3) along the lines defined by $\mathbf{K}_1$ and $\mathbf{K}_2$ and are shown in figure 2.7(a) for a (13,0) nanotube.

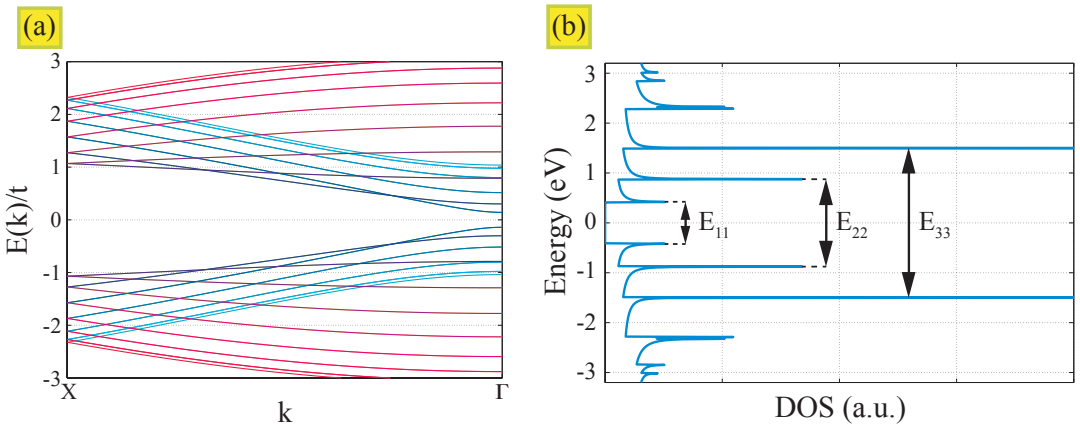

Figure 2.7: ***(a)*** *The calculated energy dispersions according to eqn.* (2.10) *for a (13,0) - nanotube with a diameter on the order of 1 nm. Color coding is used to distinguish the subbands in the valence and conduction band with different index* ζ. ***(b)*** *The calculated density of states for an individual free-standing (13,0) - nanotube. The arrows indicate the first three interband transitions* E_{ii} *for* $i = 1 \cdots 3$. *As this nanotube species is semiconducting, it features a band gap of about 0.8 eV with a zero density of states between the corresponding vHs'. The latter are due to the 1D nature of single-walled carbon nanotubes.*

Density of states

From the $2N$ energy dispersions shown in figure 2.7(a), the DOS for carbon nanotubes is computable. The DOS corresponds to the number of available electronic states per energy interval $^{\Delta N}/_{\Delta E}$ and its shape depends strongly on the dimensionality of the structure under study. For carbon nanotubes a general expression for the DOS reads [26]:

$$D(E) = \frac{T}{2\pi N} \sum_{\pm} \sum_{\zeta=1}^{N} \int \frac{1}{\left| \frac{\mathrm{dE}_{\mathrm{i}}^{\pm}(\mathrm{k})}{\mathrm{dk}} \right|} \delta(E_{\zeta}^{\pm}(k) - E)\mathrm{dE} \tag{2.11}$$

The term $\left(\left|{}^{\mathrm{dE}_{\mathrm{i}}^{\pm}(\mathrm{k})}/_{\mathrm{dk}}\right|\right)^{-1}$ introduces van Hove singularities (vHs') [31] for a flat progression of the energy dispersions. Equation (2.11) can be expressed as [47, 48]

$$D(E) = \frac{a\sqrt{3}}{\pi^2 R t} \sum_{\pm} \sum_{\zeta=1}^{N} \frac{|E|}{\sqrt{E^2 - \epsilon_\zeta^2}} \ , \tag{2.12}$$

whereas $R = 1/2 \cdot d_t$ denotes the nanotube radius and ϵ_ζ the energy difference of the vHs and the Fermi level. With the relation $\epsilon_\zeta = E_\zeta/2$, for the first semiconducting and metallic transitions one obtains [27]

$$E_{\zeta=1}^{\mathrm{S}} = 2(at/d_{\mathrm{t}}) \quad \text{and} \tag{2.13}$$

$$E_{\zeta=1}^{\mathrm{M}} = 6(at/d_{\mathrm{t}}) \quad . \tag{2.14}$$

Here E_ζ represents the energy of the bandgap of the transition between the vHs of the valence and the corresponding vHs of the conduction band with index ζ and the superscript denotes whether the transition is metallic or semiconducting.

Those vHs' are characteristic for quantum wires and dominate the DOS of 1D structures [26, 49–54]. In figure 2.7(b), the numerical calculation of the DOS for a (13,0) nanotube is shown. As such a nanotube is semiconducting, the DOS shows a bandgap with a zero DOS between the vHs' of the E_{11}-transition. This transition yields a bandgap of $E_{11} \approx 0.82\,\mathrm{eV}$, corresponding to a transition wavelength of $\approx 1.5\,\mu\mathrm{m}$, whereas longer wavelengths wont be absorbed by this SWCNT. Further transitions E_{pp}, $p = 2, 3, \ldots$ are also present between the corresponding vHs' in the conduction and valence band [figure 2.7(b)].Using equations (2.13) and (2.14), the so-called Kataura plot is obtained, in which the bandgaps of SWCNTs are plotted as a function of the SWCNT diameter [55]. The plot is reproduced in figure 2.8 and allows to state that

(1) By selecting nanotubes of a defined chirality (defining the diameter), it is possible to precisely tailor the desired absorption and combination of absorption features, and
(2) A sample containing nanotubes of a certain diameter distribution yields a distribution of bandgap energies and consequently smeared out absorption peaks.

Please note that figure 2.8 does not include the trigonal warping effect splitting the transition energies into two peaks [27].

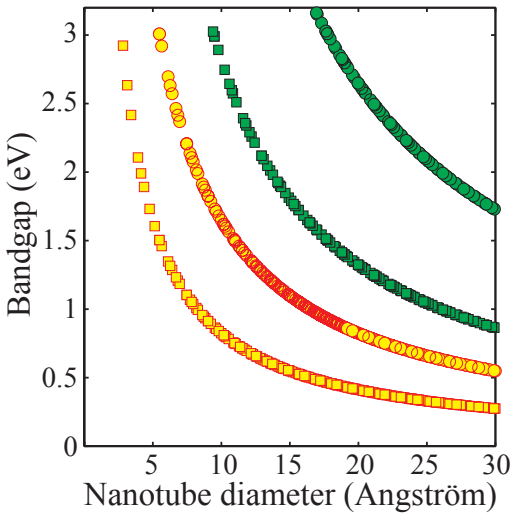

Figure 2.8: *Calculated bandgap energies of the electronic E_{11} and E_{22} transitions of individual free-standing SWCNTs vs. nanotube diameter. The plot is reproduced according to equations 2.13 and 2.14, respectively. Semiconducting nanotubes are plotted in yellow and metallic in green. The squares denote the corresponding E_{11} transition, circles the E_{22} transition.*

2.3.2 Free-standing SWCNTs, excitons, Coulomb renormalization & the dielectric background

The Kataura plot (figure 2.8) actually describes *free standing* SWCNT-samples, treating charge carriers in the single particle picture. This model needs to be extended to accurately describe the absorption of real samples. The correction terms presented in the following stem from excitonic effects, Coulomb renormalization, and the influence of the relative permittivity of the background (the embedding layer).

The observed absorption and fluorescence spectra of individual nanotubes differ from tight binding calculations (*cf.* [50, 56]) because of the fact that optical excitations originate from *excitons* [57–60], which has been confirmed by two photon excitation luminescence experiments [61–63].

Figure 2.9 shows the E_{11} transition and its according excitonic states. States labeled with 'u' have odd symmetry and - being two photon forbidden - allow only single photon transitions. Excitonic states labeled with 'g' show even symmetry, are two photon allowed and thus permit only transitions involving two photons [62].

The interband transitions E_{ii} (free-particle picture) yield a negligible oscillator strength compared to the excitonic transition, consequently only the latter is detectable in optical spectra [64, 65], complicating the correlation of the vHs' energy and the energy of the excitonic transition.

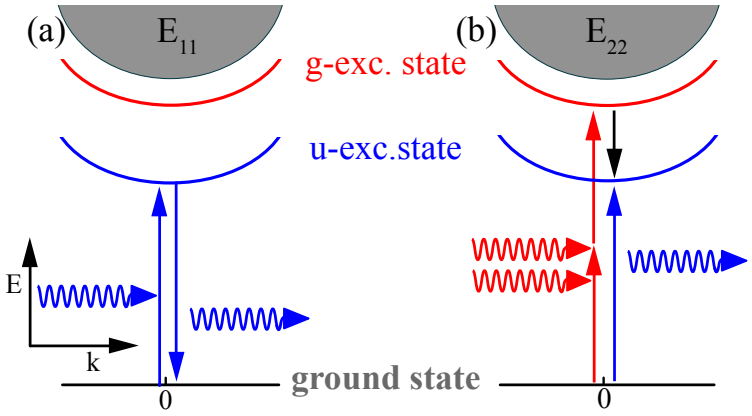

Figure 2.9: *Schematic of one and two-photon absorption in SWCNTs and the excitonic states involved; (a) The u-excitonic state is one-photon-active. The incident photon (frequency ν_{abs}) is absorbed in the u-state and relaxes from this state to the ground state, emitting a photon of the same frequency $\nu_{em} = \nu_{abs}$. (b) The two-photon-active g-excitonic state is forbidden for one photon processes. Hence, two photons (red) are necessary for transitions to the g-state. The system relaxes non-radiatively (black) to the one-photon-active u-state and relaxes subsequently to the ground state (blue). With $\nu_{abs} < \nu_{em}$, whereas $2 \cdot \nu_{abs} \neq \nu_{em}$. Figure reproduced from [62].*

Based on the hydrogen atom, the excitonic binding energy for the E_{11} transition may be estimated at approximately 260 meV and the exciton radius is on the order of 2.1 nm [60, 66–70], *i.e.*, the exciton binding energy E^{11}_{exc} is larger than in 3D ($\approx$0...70 meV) or 2D semiconductors ($\approx$5...100 meV), and the exciton radius indicates an extension of the excitons outside the nanotube into the embedding layer.

In reference [71] exciton binding energies $E^{11}_{\text{exc}} \approx 300$ meV and $E^{22}_{\text{exc}} \approx 420$ meV are calculated for a 1 nm diameter SWCNT of, *i.e.*, the calculation is almost matched by the estimation of $E^{11}_{\text{exc, est.}} \approx 260$ meV. The decrease in transition energy due to the exitonic binding energy results in a red-shift of the corresponding absorption peak. However, further effects additionally alter the transition energy, partially counterbalancing or increasing this red-shift due to the excitonic binding energy.

Coulomb renormalization (CR) due to attractive or repulsive Coulomb interaction between electrons and holes or electrons and electrons increases the transition energies by $\Delta E^{11}_{\text{CR}} \approx$520 meV and $\Delta E^{22}_{\text{CR}} \approx$690 meV [71], whereas the *dielectric constant of the background* $\epsilon_{\text{r, bg}}$ changes the transition energies by $\Delta E^{11}_{\text{bg}} \approx -100$ meV and $\Delta E^{22}_{\text{bg}} \approx -140$ meV if a dielectric constant of $\epsilon_r \approx 2$ is assumed [71].

Figure 2.10 schematically shows the transition energy E_{11} of a (13,0) nanotube, whereas calculations are based on free-standing single particles (black). The figure also depicts the influence of CR, the excitonic binding energy and the background ϵ_r - included one after the other - on the transition energy (red, blue, green).

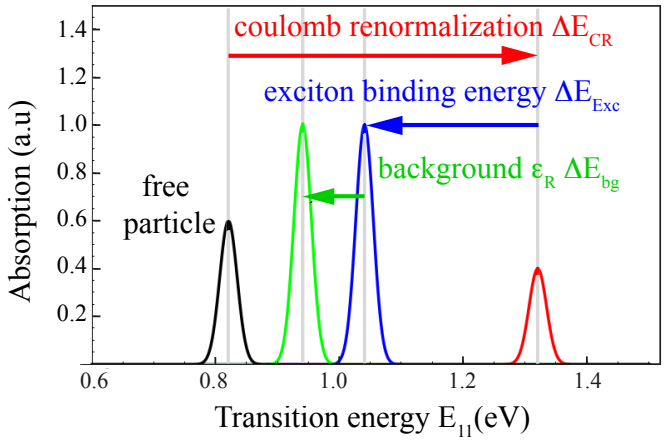

Figure 2.10: *Schematic of the SWCNT absorption of a (13,0) nanotube (diameter of about 1 nm) as a function of E_{11} transition energy in eV. The black curve denotes the absorption using the tight binding model of a free particle, the red curve additionally considers Coulomb renormalization. The blue curve includes the excitonic binding energy and the green curve adds the effects of the background dielectric constant.*

The plot of figure 2.10 indicates that, compared to the model including CR, excitonic binding energy and the dielectric background, the tight-binding model underestimates the transition energy, which is confirmed by empiric studies [72].

2.3.3 Linear transmission

Equation (2.14) and (2.13) may be used to calclulate the spectral position of absorption features for a given nanotube. These calculated absorption maxima need to be corrected by the exciton binding energy, the CR, and the background permittivity as shown in the previous section.

In the samples under study, SWCNTs of *Unidym Inc.* are used, that are produced by the high pressure carbon monoxide gas phase deposition (HipCO) method (see section 2.3.4). These SWCNTs are specified with a diameter between 0.8 and 1.2 nm. If an average diameter of 1 nm and the effects mentioned in the previous section are considered, E_{11} is calculated using $E_{11} = E_{11,\,\mathrm{free}} + \Delta E^{11}_{\mathrm{CR}} - E^{11}_{\mathrm{exc}} + \Delta E^{11}_{\mathrm{bg}} = 940\,\mathrm{meV}$, which corresponds to a wavelength of 1320 nm, being 215 nm smaller than the measured transmission minimum of the SWCNT-SA assigned to the E_{11} transition.

In figure 2.11 the transmission of a SA based on *Unidym* SWCNTs is plotted as function of wavelength. The green shaded regions denote the calculated transition energies of the E_{11} and E_{22} transitions, applying the supplier-specified tube diameter of $0.8\,nm \lesssim d_t \lesssim 1.2\,nm$ and equation (2.13). These regions further include the

changes in transition energy due to the different effects described in the previous section.For the E_{22} transition, a $\Delta E^{22}_{\mathrm{CR}} = +690\,\mathrm{meV}$, $E^{22}_{\mathrm{exc}} = -420\,\mathrm{meV}$ and $\Delta E^{22}_{\mathrm{bg}} = -140\,\mathrm{meV}$ were assumed [71]. The calculated spectral position of the E_{22} transition is overestimated by approximately 90 nm (140 meV), but the range still includes the measured transmission minimum.

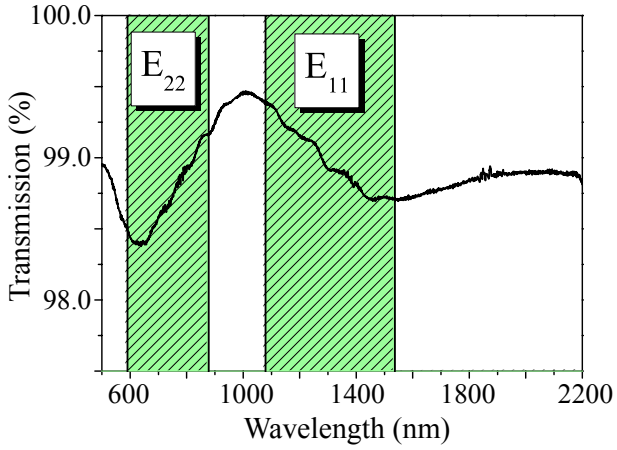

Figure 2.11: *Measured absorption spectrum of a HipCO SWCNT-SA (black solid line) and the calculated distribution of E_{11} and E_{22} transition energies (green shaded). The correction terms ΔE^{ii}_{CR}, E^{ii}_{exc} and ΔE^{ii}_{bg} are assumed for the latter.*

Bundling - a topological effect

As shown in figure 2.11, the correction terms introduced so far do not allow an accurate match of the theoretic and measured transmision minima. The observed red-shift of the measured absorption may be explained by the topology of the SWCNT sample, which does not consist of individual SWCNTs, but of bundles of SWCNTs. Bundling may influence the transition energies by introduction of a red-shifts of up to several hundred meV [73, 74]. Therefore, the theoretical calculation requires a further correction term considering bundling and a value of $\Delta E_{\mathrm{bund}} \approx$-135 meV needs to be introduced to match theory and measurement.

Figure 2.12 illustrates the same transmission curve of the HipCO sample as figure 2.11, but in the calculation of the absorption ranges (blue shaded) an additional correction term due to bundling has been considered. As can be seen from these figures 2.11 and 2.12, the correction terms allows to match the measured and calculated energy of the E_{11} transition, but seems invalid for the E_{22} transition using the given parameters.

To visualize SWCNT bundling, imaging techniques as scanning- and transmission electron microscopy need to be applied, as those are capable to resolve individual SWCNTs and their bundles, which is shown in figure 2.13 by one scanning (a)

and two transmission electron micrographs of a SWCNT-SA (b and c). The low resolution TEM measurement [figure 2.13(a)] denotes interweaved SWCNTs, and higher resolution SEM micrographs [figure 2.13(b) and (c)] allow resolving SWCNTs that are bundled with each other.

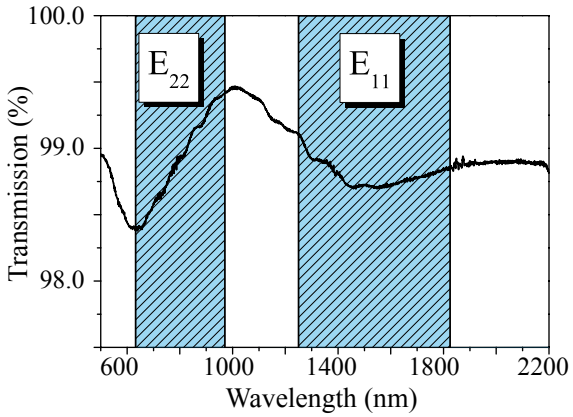

Figure 2.12: *Measured absorption spectrum of a HipCO SWCNT-SA (black solid line) and the calculated distribution of E_{11} and E_{22} transition energies (blue shaded), considering the correction terms ΔE^{ii}_{CR}, E^{ii}_{exc}, ΔE^{ii}_{bg} and ΔE_{bund}*

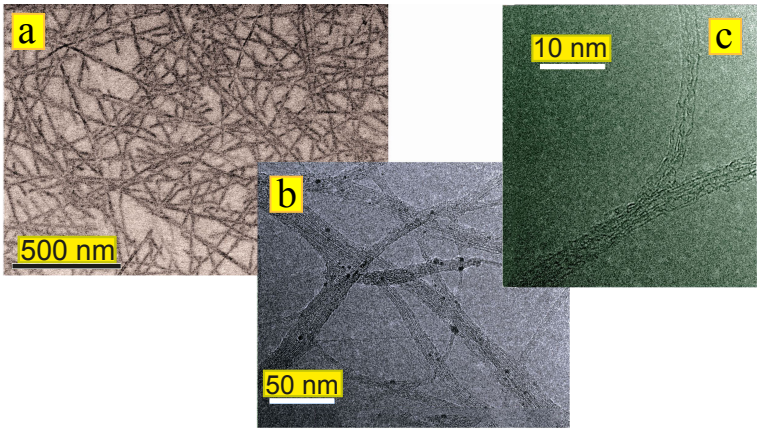

Figure 2.13: *a) The scanning electron micrograph of the SWCNT-SA already shows that individual SWCNTs are not free standing, but in contact to each other. b) and c) The transmission electron micrographs recorded at different resolution show that SWCNTs are bundled. Image reproduced from [75].*

2.3.4 Transmission spectra of *real world* SWCNT-SAs

Two eminent techniques of SWCNT growth are the synthesis by an arc discharge and the before mentioned HipCO method. In the first, the soot produced by an arc-discharge between two carbon electrodes contains different carbon nanostructures, like bucky balls and SWCNTs [70]. The fabrication of SWCNTs by the HipCO process is a chemical vapor deposition technique, as the SWCNTs are grown from the gas phase (with carbon monoxide feedstock) under high pressure (up to 10 bar) and temperatures around 1000°C [76].

Figures 2.11 and 2.12, both show the transmission spectrum of a HipCO SWCNT-SA. The two local minima represent the two lowest semiconducting interband transitions E_{11} and E_{22}. Obviously, *real world* SAs do not show the same sharp absorption peaks as theoretical plots (*cf.*, figure 2.7(b)). The large number of SWCNTs present, varying in diameter and chirality, smears out the sharp absorption features of individual SWCNTs, resulting in a smooth curve progression.

In most samples, it is not possible to determine all SWCNT species present, however, measuring the Raman shift of the sample under study allowed to identify the most prevalent SWCNT species. This is possible due to the radial breathing mode (RBM), an unique Raman resonance of nanotubes spectrally isolated from other resonances. The RBM is located at Raman shifts in the range of 120 to 350 cm^{-1}, and due to the radius dependence of its frequency, the RBM allows for an (n, m) assignment [77]. Figure 2.14 (a) shows the Raman spectrum of a HipCO SWCNT-SA. The local maxima in the frequency range of the RBM, that may be assigned to different SWCNT species, namely SWCNTs of chiralty (10,2), (12,1), (10,5), (9,7) and (13,3), corresponding to tube diameters between 0.84 and 1.17 nm.

Figure 2.14 (b) shows the transmission of two HipCO-made SWCNT-SAs (yielding differeent SWCNT concentrations) and the wavelength corresponding to the E_{11}-transition of the identified SWCNTs. Compared to the transmission spectrum of an arc-made SWCNT-SA [figure 2.15(a)], the basic absorption features are similar in both measurements, but their spectral position is shifted towards longer wavelengths for the arc-made SWCNTs, which is due to their larger commonly obtained mean diameter.

Arc-made SWCNTs show an absorption around 1.0 and 1.9 µm, consequenly their operation range covers lasers around 1 and 2 µm (*i.e.*, based on Yb and Tm). The residual absorption above 2 µm allows for application in lasers at this wavelength range. However, a sample based on arc-made SWCNTs is *not* useful for the emission wavelengths of chromium (Cr) between 1.25 and 1.5 µm. The hipCO-made SWCNT-SA covers the wavelength range of the two Cr-lasers (forsterite and YAG, not excluding other possible lasers suitable for mode-locking in this wavelength range), located around 1.25 and 1.5 µm. For lasers emitting around 1 and

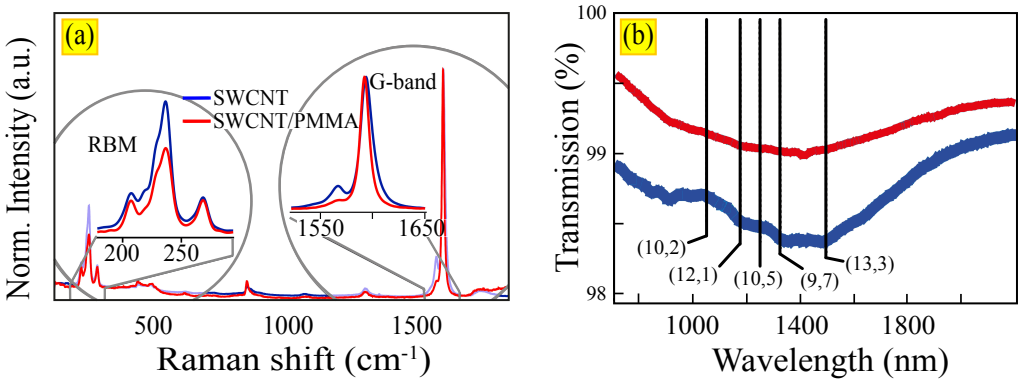

Figure 2.14: *(a) Raman spectrum of a HipCO SWCNT-SA, showing the radial breathing mode around 200-250 cm^{-1}. The radial breathing mode consists of different local maxima with frequencies $\omega_{i,\ RBM}$, suitable to identiy SWCNTs with chiralities (13,3), (9,7), (10,5), (12,1), and (10,2). (b) Transmission of two HipCO-made SWCNT-SAs of different SWCNT concentration. The lowest transition energy E_{11} of each of the identified semiconducting SWCNTs is marked in (b). Figure from [75].*

2 µm (*e.g.* Yb & Tm), this device is not applicable. However, individual HipCO samples presented in the course of this work showed sufficient absorption around 1 µm and have been applied near this wavelength.

2.3.5 Expansion of the optical response

As described in the previous section, the absorption of SWCNTs depends on the tube diameter, coarsely influenced by the production process. Figures 2.15(a) and (b) show the transmission spectra of arc-made and HipCO-made SWCNTs with the two lowest semiconducting interband transitions E_{11} and E_{22}, and for the arc-made SWCNTs additionally the first metallic transition E_{11}^{M}. Metallic SWCNTs are inherently present in each production process, whereas purification of the yield os possible [78, 79]. The gray bars in the figure indicate the spectral region of usable absorption, complementing one another. Consequentlly, incorporating the differently produced SWCNTs into one element, a SA with an octave spanning absorption from $\approx$1.0 to 2.1 µm is obtained. The transmission of the HipCO + arc-made SWCNT-SA is shown in figure 2.15(c), displaying an almost uniform absorption over a whole octave.

Several HipCO + arc-made SWCNT-SAs working in transmission were produced. One of them has been used for mode-locking of 4 different bulk laser types, namely Yb:KLuW at 1.07 µm, Cr:forsterite at 1.24 µm, Cr:YAG at 1495 µm and the Tm:KLuW laser operating at 2,07 µm [75, 80].

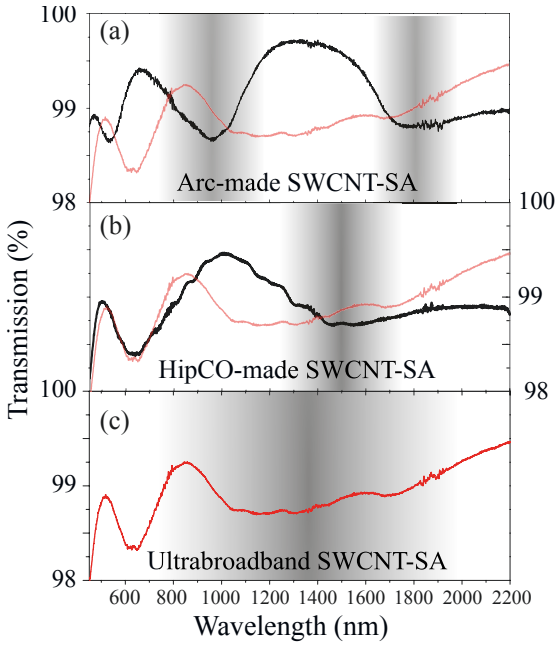

Figure 2.15: *Measured optical transmission of an arc-made SWCNT-SA (a) and a HipCO-made SWCNT-SA (b). The optical response is largely extended incorporating both differently produced SWCNTs in one element. The obtained absorption covers the wavelength range from 1.0 to 2.1 µm (c). The gray bars indicate the spectral region of applicable absorption, and the curve of (c) is re-plotted in (a) and (b) for comparison.*

Chapter 3

Relaxation dynamics & saturable absorption

In order to implement carbon nanostructures as mode-locking element into a laser, it is essential to know the saturation and relaxation behavior of the element. Mode-locking does not require recovery times on the order of the achieved pulse duration as ultrashort pulses are achieved with slow saturable absorbers as well [*cp.* chapter 4 & [81]]. Relaxation of the absorber, however, is preferentially happening on a time scale shorter than the round trip time $T_{\mathrm{R}} = \frac{2 \cdot l}{c}$, with the resonator length l and the speed of light c. This condition is usually not critical in the laser cavity setups used in this work, yielding $\approx 100\,\mathrm{MHz}$ repetition rate and a round trip time on the order of 10 ns.

This chapter addresses the relaxation behavior of optically excited carbon nanostructures, sketches the processes involved and explains the measurement of the relevant time constants. It furthermore gives a comparison to SESAMs.

3.1 Ultrafast processes in semiconductors

3.1.1 Relaxation regimes in Semiconductors

Figure 3.1 depicts the four relaxation regimes of semiconductors according to reference [82]. Loose idendification of those regimes is possible for every relaxing semiconductor system, whereas the excact temporal extend, as well as the amount of adjacent regime overlap, are specific for each individual semiconductor system under study. The processes incorporated in the relaxation of a many-particle system are characterized by individual time dependent scattering rates.

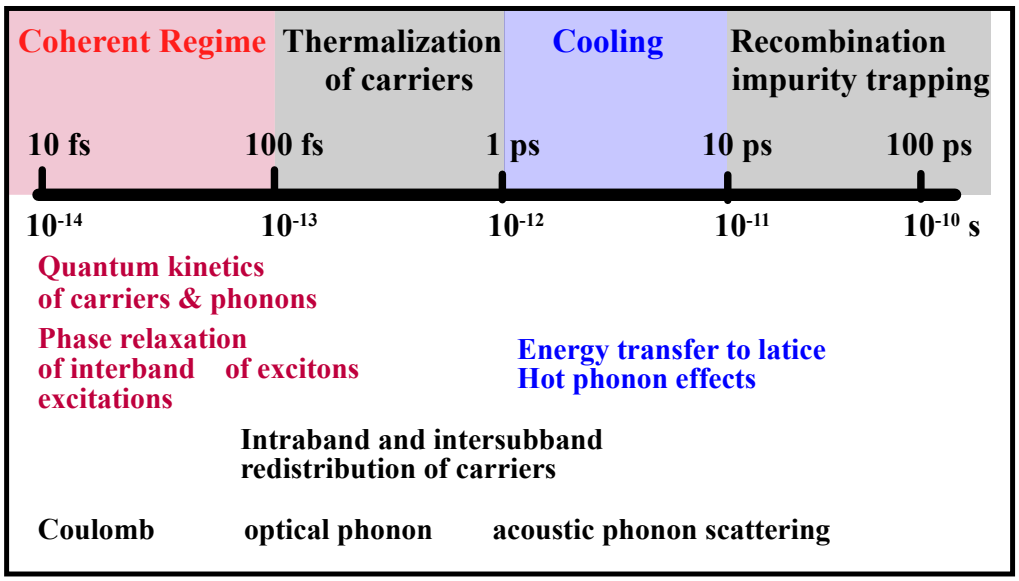

Figure 3.1: *Relaxation regimes in semiconductors after relaxation (top row) and according time scales. The main effects occuring within the regimes (below timeline) and the scattering mechanisms (bottom row) are given as well. Although limits of the regimes are drawn clearly, different relaxation regimes overlap in time. Coulomb scattering does not stop after 100 fs but wont be the dominating process after the coherent regime. Figure according to [82].*

3.2 Relaxation dynamics in graphene & SWCNTs

Directly after, respectively during excitation with an ultrashort pulse, *i.e.* at time $t \approx 0$, the distribution of carriers and holes is described by a

Nonequilibrium carrier distribution.

If an ultrashort pulse centered at 1.5 eV with a 0.6 eV bandwidth (corresponding to a Ti:sapphire laser similar to the one used in [83], figure 3.3(a) shows an exemplary spectrum) excites a graphene sample, electrons are generated at +0.75 eV in the conduction band and holes at -0.75 eV in the valence band. If no relaxation occurs during excitation, the structure of the spectrum is reflected in the distribution of electrons and holes. This is simplified in figure 3.3(b), showing the Dirac cone and a schematic plot of the nonequilibrium carrier density distribution at $t \approx 0$ [1].

A nonequilibrium carrier distribution is generated in SWCNTs as well. Here, the excitation may be resonant to the band edge of the n^{th} subband in the valence and

[1] Additionally, the excitation by (commonly) polarized radiation induces an spatially anisotropic carrier distribution, which relaxes mainly via cop-scattering within 50 fs [71].

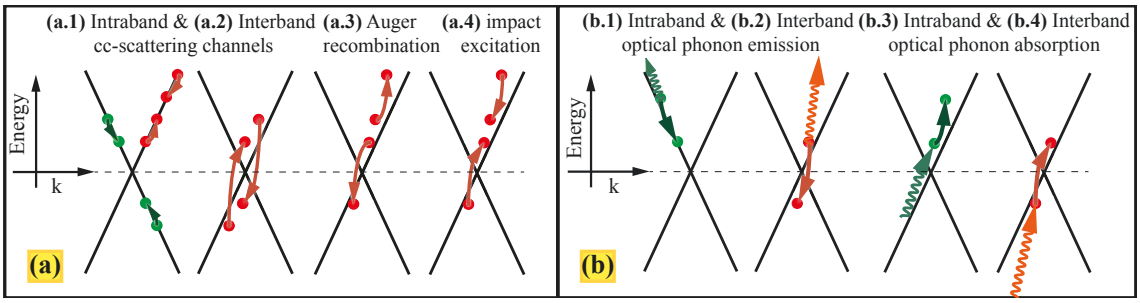

Figure 3.2: ***(a)*** *Possible transitions of carrier-carrier scattering in graphene. The Dirac cone close to the K-point is indicated by the black lines. Intraband relaxation channels (a.1) and interband relaxation channels (a.2) show an unchanged number of carriers in the bands. Coulomb-induced Auger processes change the number of carriers in the conduction and valence band. Auger recombination (a.3) reduces the number of carriers in the conduction band, whereas impact excitation (a.4) increases their number.* ***(b)*** *Different possible transitions of carrier optical phonon-scattering in graphene: (b.1) & (b.2) Denote processes emitting an optical phonon, whereas in (b.3) & (b.4), an optical phonon is annihilated. Images reproduced from [71].*

conduction band or off-resonant to those bands. The structured DOS of SWCNTs may alter the shape of the carrier distribution function but not its nonequilibrium character. The subsequent relaxation regime, namely the

Nonthermal regime

includes the *coherent regime* and the *thermalization regime*, whereas both regimes contribute to equilibration of the sample under study. The coherent regime is characterized by a prevalence of Coulomb mediated carrier-carrier scattering (cc-scattering), illustrated for graphene in figure 3.2(a).

Carrier optical phonon scattering (cop-scattering) dominates the relaxation of the system during thermalization and, as well as cc-scattering, contributes to flattening of the nonequilibrium distribution of electrons and holes. Cop-scattering dissipates excess energy to the lattice along the Dirac cone with characteristic steps of $E_{\text{opt}}^{\text{phon}} \approx 200\,meV$. Possible cop-scattering processes in graphene are depicted in figure 3.2(b). In SWCNTs and graphene, the nonequilibrium carrier distribution relaxes to a thermal Fermi-Dirac distribution of 'hot' electrons and holes [2] within about the first 200 fs [83].

After equilibration, the Fermi-Dirac statistics describes the occupation probabil-

[2] Separate Fermi-distributions and -levels are discussed in [83].

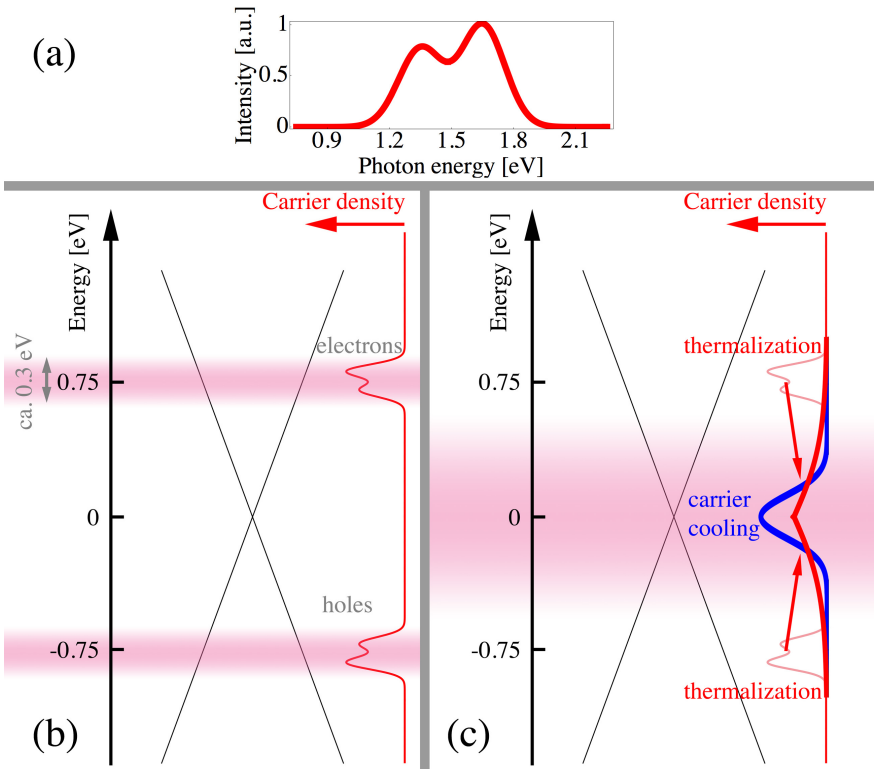

Figure 3.3: *Relaxation processes in graphene after optical excitation with an ultrashort pulse. (a) the structured optical spectrum of the incident pulse. (b) The crossing gray lines denote the linear energy dispersion of graphene near the Dirac point. Excitation with an ultrashort pulse generates structured carrier densities (red) - electrons in the conduction band and holes in the valence band. (c) The nonequilibrium carrier densities (pale red) thermalize ultrafast towards a hot Fermi distribution for electrons and holes (red). Subsequently they are altered due to carrier cooling (blue), governed by cop- and cap-scattering. Figure following reference [84].*

ity of an electronic state, given by

$$w(E) = \frac{1}{\exp\left(\frac{E-\mu}{k_\mathrm{B}T_\mathrm{C}}\right)+1}\ , \tag{3.1}$$

with the Energy E, the chemical potential μ, the Boltzmann constant k_B, and the carrier temperature T_C. Consequently, T_C suffices to describe the carrier distribution of a given fermion ensemble. In an excited system the carrier temperature T_C may temporarily be on the order of several thousand degree Kelvin [71, 83, 84], being substantially higher than the lattice temperature T_L of the sample.

Carrier cooling & recombination

Inelastic phonon scattering allows for energy dissipation from the system of charged carriers to the lattice, cooling the 'hot' charge carriers from $T_C > T_L$ to $T_C \cong T_L$. In addition to cop-scattering, scattering of charge carriers with acoustic phonons sets in on a picosecond timescale. In contrast to optical phonons, acoustic phonons have an arbitrary energy, that is, however, in general smaller than $E_{\text{opt}}^{\text{phon}}$.

In graphene and SWCNTs the contribution of cap-scattering becomes important for the relaxation of charged carriers with an excess energy below $E_{\text{opt}}^{\text{phon}}$. Relaxation of those carriers with optical phonons is not possible and occurs on a picosecond timescale [71, 85]. Cc-scattering may still occur but the probability of this scattering process is negligible due to the decreased density of scattering partners.

Their recombination is either phonon assisted (SRH - process) or radiative, *i.e.* a photon is emitted spontaneously during recombination. Auger recombination is assumed negligible in this regime of relaxation [71]. Recombination and cooling is described by the relaxation time τ_2, which is of the order of a few picoseconds for graphene [83], and of the order of 5 - 20 ps for SWCNTs [86].

The relaxation steps of a graphene sample after an exemplary excitation with an ultrashort pulse is shown in figure 3.3.

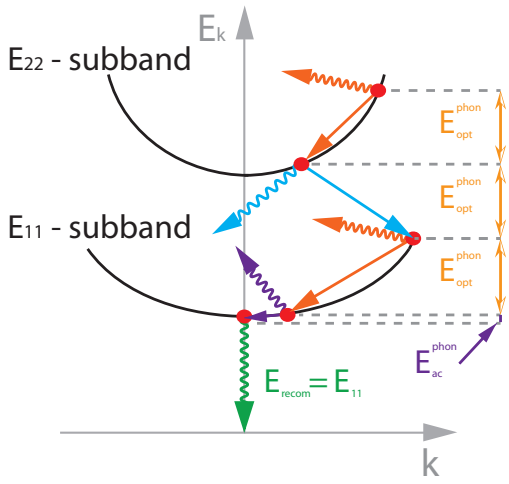

Figure 3.4: *Relaxation paths in SWCNTs. Optical phonons exhibit an energy of ≈200 meV, depicted by the yellow arrows. Intraband scattering with optical phonons (orange) relaxes the carriers within the subbands, emitting an optical phonon (orange wavy line). Inter-subband relaxations due to carrier optical phonon-scattering occurs as well (light blue). Carrier acoustic phonon-scattering (purple) is essential if the charged carriers relaxed close to the band edge of the lowest conduction band. Here the energy that needs to be dissipated to the lattice is smaller than E_{opt}^{phon}, and scattering with optical phonons is not relevant any longer. Scattering with acoustic phonons allows an energy dissipation E_{ac}^{phon} of arbitrary height. Carrier recombination (green) is the final step of relaxation.*

3.3 Saturation effects in carbon nanostructures

Nanotubes and graphene, display an optical transmission which depends nonlinearly on the incident power. In both systems, charged carriers are excited from the valence to the conduction band by absorbing a photon. With increasing fluence, the rise of the number of occupied states and the electron depletion in the valence band prevent the absorption of subsequent incident photons. This state filling is called Pauli blocking, leading to a characteristic decrease of the absorption with increasing incident intensity.

The previous section explained different relaxation regimes of carbon nanostructures in detail. Under the assumption of a slow saturable absorber, it has proven helpful to integrate the temporal dependence out and write the transmission simply as a function of the fluence F [87]. The fluence is defined as pulse energy per area, *i.e.*, the temporal integral over the intensity. Therefore, if the pulse duration is shorter than the absorber recovery time, the nonlinear transmission can be written as

$$T(F_{\mathrm{P}}) = T_{\mathrm{ns}} \cdot \frac{ln[1 + T_{\mathrm{lin}}/T_{\mathrm{ns}}(e^{S} - 1)]}{S} \ , \tag{3.2}$$

with the non-saturable transmission T_{ns}, the linear transmission for small signals T_{lin}, and the saturation parameter

$$S = \frac{F_{\mathrm{i}}}{F_{\mathrm{sat}}} \ . \tag{3.3}$$

$F_{\mathrm{i}} = \frac{E_{\mathrm{i}}}{A}$ and F_{sat} represent the incident and the saturation fluence, respectively. E_{i} is the incident pulse energy and A the irradiated area. This model function has proven highly successful to understand pulse energy dynamics on the microsecond time scale, *e.g.*, due to Q-switching.

The nonlinear transmission is therefore characterized by the following three parameters:

Non-saturable losses $\Delta T_{\mathrm{ns}} = 1 - T_{\mathrm{ns}}$ represent the contribution to the absorption that may not be saturated, even with infinite pulse energy, thus, the minimum SA transmission obtainable. Two processes contributing to the nonsaturable losses are scattering at rough surfaces and defects in a homogenious SA structure.

The **modulation depth** $\Delta T_{\mathrm{mod}} = T_{\mathrm{ns}} - T_{\mathrm{lin}}$ is the maximum change in the transmission. The modulation depth for a reflective SA is $\Delta R_{\mathrm{mod}} = R_{\mathrm{ns}} - R_{\mathrm{lin}}$. With increasing modulation depth the suppression of cw-laser background becomes more effective, and a pulsed operation is favored. However, a higher modulation depth also leads to an increased tendency toward Q-switching [88].

The **saturation fluence** F_{sat} represents the fluence needed to decrease the transmission or reflection to the $1/e$-value ($\approx 37\%$) with respect to the modulation depth, ΔT_{mod} respectively ΔR_{mod}.

If physically relevant, two photon absorption (TPA) may be included into this model function by multiplying equation (3.2) with e^{-F_{P}/F_2}, whereas F_2 indicates the fluence at which the transmission dropped to $1/e$ (37 %) due to TPA. F_2 can be related to material parameters like the TPA absorption coefficient β_{TPA} and the absorption length z by [87]

$$F_2 \approx \frac{\tau_{\mathrm{P}}}{\beta_{\mathrm{TPA}} \cdot z} \quad . \tag{3.4}$$

SESAMs are known to show non negligible TPA [89]. In carbon nanostructures, TPA is expected as well (see for instance figure 2.9, indicating two-photon allowed excitonic transitions), but in SWCNTs, the fluence F_2^{SWCNT} depends strongly on the wavelength of illumination. Using a Ti:sapphire laser at a central wavelength of 800 nm, TPA has been observed in a SWCNT absorber [90], whereas measurements of the nanotube absorber in other wavelength regions under study did not show TPA at the available fluence of 200 $\frac{\mu\mathrm{J}}{\mathrm{cm}^2}$ and above [75, 91]. In graphene no TPA is observed in the experiment.

3.4 Comparison of the saturable absorbers

Physical principles of absorption and saturation

The underlying physical principles of absorption and saturable absorption are identical in SESAMs and nanostructure-SAs. Electrons in the valence band are excited to the conduction band via dipole-allowed transitions, and If approximated by a two-level system, the absorption coefficient (*cf.* section 4.1.1) is given by [92]

$$\alpha = \sigma_{12} N_1 = -\frac{\frac{dI}{dx}\big|_{\mathrm{abs}}}{I} \ , \tag{3.5}$$

with the absorption cross section being related to the Einstein coefficient by

$$\sigma_{12} N_1 = B_{12}\, h\, f_{12}/c \ . \tag{3.6}$$

From the excited state, the system relaxes within the decay time. Saturable absorption occurs in both types of SAs under excitation with sufficiently high fluence to initiate Pauli blocking, *i.e.*, a depletion and filling of the states in the valence and conduction band, respectively.

The relaxation time of a pristine semiconductor is in the order of 1 ns, therefore SESAMs used for mode-locking of lasers need to be designed to show a shorter relaxation time on the order of picoseconds or faster.

SESAM defect centers & SWCNT bundling

The reduced relaxation time of a SESAM compared to an untreated semiconductor is achieved by means of surface geometries or the generation of defect centers by ion implantation. Both methods decrease the effective relaxation time but the latter additionally increases the losses due to newly generated scattering centers.

The measured 70-300 fs recovery times of the E_{11} transition (section 5.1) are about 2 to 8 times faster than the previously reported values for the E_{22} transition in SWCNT-SAs based on the arc-discharge method [93] and other previous reports [94]. This acceleration is attributed to the nanotube bundling, in particular to their pronounced tendency to cling together [95]. The acceleration, however, is obtained at the expense of increased scattering and consequently larger non-saturable losses. To balance non-saturable losses and the accelerated relaxation, control of the alignment and spatial distribution is crucial. Equivalent considerations have to be made regarding the defect density in SESAMs [96, 97].

Tailoring the modulation depth

The modulation depth of a SA determines the discrimination of the mode-locked regime against cw operation of the laser. A sufficiently high modulation depth is necessary to guarantee pulsed operation. However, a high modulation depth increases the probability for q-switching (see section 4.5.1), and is connected with an increase of the overall absorption and the non-saturable losses. In case of SESAMs, the modulation depth is increased by fabrication of multiple quantum wells [98] or by introducing a resonant SESAM design [99].

The absorption of a single layer of graphene amounts to $\approx 2.3\,\%$. A simple way of increasing the absorption of the element is to incorporate several layers of graphene into the absorber which results in a stepwise increase of the absorption. To ensure an independent absorption of each of the layers, they are individually grown and manually transfered on each other. Doing so the graphene layers are stacked in no particular order and are expected to behave like the sum of n individual monolayers of graphene. Actually this is only partially true. The absorption behaves like expected and increases approximately in steps of 2.3 % (figure 3.5). The saturation fluence of the bilayer sample ($24\,\frac{\mu J}{cm^2}$), however, does not amount to twice the value of the monolayer sample ($14.5\,\frac{\mu J}{cm^2}$), indicating that the relaxation behavior of

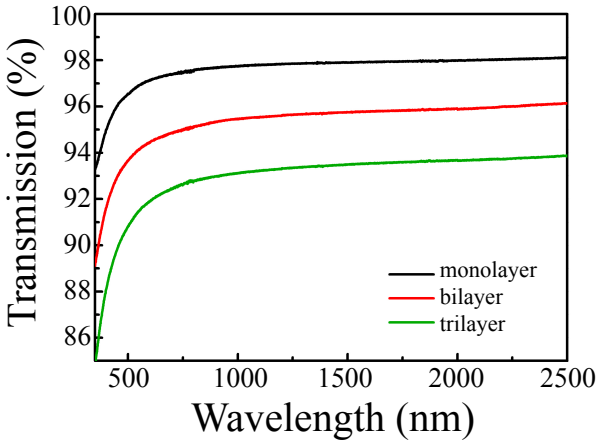

Figure 3.5: *Optical transmission spectra of a monolayer, bilayer and trilayer graphene sample. The increase in absorption occurs in steps of 2.3 %. Data provided by the corresponding author of [100].*

graphene layers, placed in vicinity to each other, is changed by the different environment [100]. This is not very surprising, as already a changed dielectric background constant influences the relaxation behavior of nanostructures [71] and the energy dispersion of mono- and bilayer graphene differ from each other [36, 101].

The absorption of an SWCNT-SAs is determined by the number of SWCNTs that are illuminated by the laser. This number may be varied by means of the concentration of nanotubes on the SA, or (if the concentration remains unchanged) the layer thickness. It is to be noted that a higher concentration results in higher probability of bundling (see chapter 2.3.3), and yields higher scattering losses. For the samples in this work, the concentration of the PMMA-SWCNT mixture was kept constant, but altering the rotational speed during the spin-coating process allowed for the fabrication of samples with different absorption values.

In table 4.1 common properties and parameters of SESAMs and nanostructure SAs are given. Due to the fact that SESAM technology matured during the last 18 years, a vast variety of devices with different parameters is available for wavelengths that may be easy covered using semiconductors. If longer wavelengths ($> 1\,\mu m$) need to be accessed, SESAM expansion strongly decelerates. From the large number of SESAMs, table 4.1 only lists those relevant for solid state bulk laser mode-locking.

Property	SESAM	SWCNT-SA	Graphene-SA
Fabrication	complex	simple	simple
Bandgap	yes	yes	no
Operation in transmission (T) or reflection (R)	mainly (R)	T & R	T & R
Operating wavelengths in µm	0.8 - 2.3[3]	0.8-2.1[4]	0.8-2.5[5]
Broadband application	no	yes	yes
Typ. eff. relaxation time	1-10 ps	≈250 fs	≈100 fs
Dominant relaxation component	slow	fast	fast
Typ. F_{sat} in $\mu J/cm^2$	150	5-10	50
Typ modulation depth in %	1-30	<0.5[6]	<1
Typ. non-saturable loss in %	2	1-2	<2
TPA	yes	no issue [7]	not observed
Self-starting	yes	yes[8]	no

Table 3.1: *Comparison of carbon nanostructure-SAs and SESAMs.*

[3] Designed for a defined wavelength (*e.g.*, 0.8 / 1.0 / 1.2 / 1.5 / 2.0 / 2.3 µm) and not applicable at other wavelengths.

[4] See [90] and section 5.4.4

[5] Values for the SWCNT-SAs used in this work. Higher modulation depths of approximately 1 and 1.9 % were reported in reference [102] for λ_{meas} =1.56 and 1.05 µm, respectively.

[6] References [103, 104] report mode-locking at the edges of this range. The range may be expanded theoretically, whereas ultimate limits are a possible non-zero Fermi-level on the low energy side, and the Fano resonance, respectively the linear range of the graphene energy dispersion, *i.e.* up to 3 eV, on the high energy side.

[7] At 800 nm TPA was observed [90]

[8] See section 5.4.1

Chapter 4

Fundamentals of ultrashort laser pulses

In this chapter the basic theory of passive mode-locking is briefly summarized. The chapter starts introducing the laser gain media and pulse shaping effects which are thereafter implemented in a mathematical model. Finally the stability of cw mode-locking is discussed.

4.1 The active Laser media

In this work, different types of active laser media were used. The crystalline hosts belong to the class of garnets, silicates, sesquioxides or double tungstates.

From the *garnets* the famous representative yttrium-aluminum-garnet (YAG) was used in this work. YAG is isotropic because it belongs to the cybic crystals. YAG provides a laser host with high damage threshold and high thermal conductivity. The latter, however, is inversely proportional on the doping level.

Forsterite (formula Mg_2SiO_4) belongs to the class of silicates and has an orthorhombic crystal structure, resulting in direction-dependent properties. Doped with Cr^{4+}, its polarization along the b-axis is, *e.g.*, most efficient for laser emission. Furthermore, with Cr-doping, a broad laser emission bandwidth of 250 nm @ 1.2 µm was achieved allowing for the generation of pulses as short as 14 fs [105]. All Forsterite laser results presented in this work have been obtained at the Ajou University in Suwon, South Korea, marked accordingly.

Sesquioxides are oxides with formula M_2O_3. M stands for a trivalent (semi)metal, or a rare-earth metal, *e.g.*, yttrium (Y), scandium (Sc) or lutetium (Lu). The latter

three elements form the sesquioxides, yttria, scandia and lutetia. They have been successfully applied as laser hosts [106], and show superior thermal properties over many other host materials. These sesquioxides are cubic and isotropic, but their high melting point (around 2430°C) requires a growth technique different than methods like Czochalski or Nacken-Kyropoulos growth or micro-pulling down. Furthermore crucible materials have to withstand the higher growth temperatures as well. The heat exchanger method (HEM) allows for the growth of sufficiently large laser crystals. This method is characterized by a constant heating of the crucible walls, whilst a heat sink is generated punctually at the crucible bottom by an increasing gas flow. The different methods of crystal growth are reviewed in [107].

Double tungstates (DT) are monoclinic crystals with formula $KT(WO_2)_2$. Here, T is a trivalent metal or rare-earth element cation, *e.g.*, yttrium or lutetium. Due to their crystal structure, the DTs exhibit directional properties, whereas the anisotropy of their optical properties is related to their principal optical axes N_m, N_p and N_g, respectively. The N_p principal optical axes coincides with the crystallographic b axis, whereas the N_m and N_g axes are defined by an angle to the crystallographic a and c axes, shown in figure 4.1(1) for KLuW.

For laser applications, polarization along the N_m and N_p principal optical axes yield a higher absorption and emission cross section and result in a better laser performance than along the N_g axis [108]. The samples used in this work were cut for laser emission polarized along one of the principal optical axes advantageous for laseer operation. The thermal conductivity is directional as well, and yields a thermal conductivity ellipsoid, which is shown in figure 4.1(2) for KLuW. The strong anisotropy of the DTs combines advantageous optical properties, a large absorption and emission cross section and a broad emission, in one crystal orientation.

The main properties of the four different laser gain media used in this work are summarized in table 4.1.

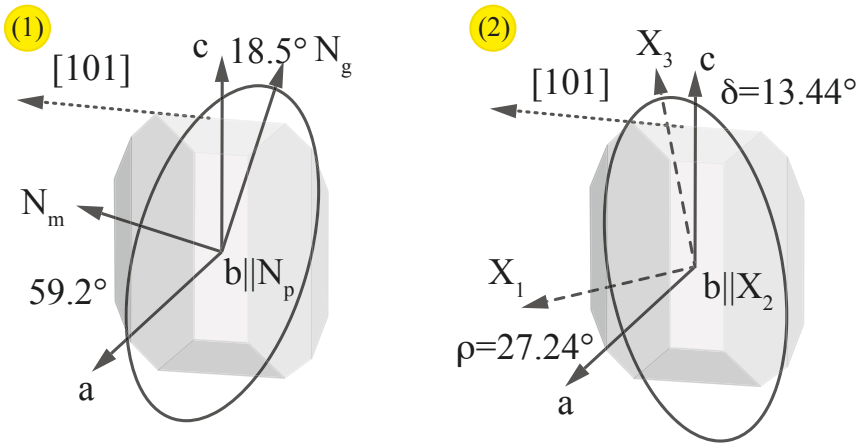

Figure 4.1: The optical (1) and thermal expansion ellipsoid (2) of KLuW at room temperature with respect to the morphology and the crystallographic frame. The crystal is grown by the top-seeded solution growth [109]. The crystallographic b-axis points out of the drawing plane and is parallel to the optical N_p axis and theX_2 axis of the thermal expansion ellipsoid. All frames are right-handed. Figure from [108].

Property	YAG	Forsterite	Sesquioxides	KLuW
Symmetry	cubic	orthorhombic	cubic	monoclinic
Preferred growth process	Cz	Cz	HEM	TSSG / Cz
Melting point (K)	≈ 2210	≈ 2160	≈ 2700	≈1330
Transparancy range (µm)	0.18 - 6.0	≈ 0.3 - 3.3	0.23 - 8.0	0.365 - 5.11
Refractive index at 1 µm	1.816	n_p=1.635 n_m=1.651 n_g=1.670	n_Sc=1.967 n_Lu=1.911 n_Y=1.890	n_p=1.995 n_m=2.030 n_g=2.084
Thermal conductivity ($\mathrm{W\,m^{-1}\,K^{-1}}$, 300K)	10.1 - 11.4	≈8	κ_Sc=18.0 (7.3)[1] κ_Lu=12.6 (11.7)[2] κ_Y=13.4 (7.4)[3]	κ_1=3.09 κ_2=2.55 κ_3=4.40

Table 4.1: *The different laser host materials used in this work and their main properties relevant for laser application. Directional properties are marked with indices referring to the optical or thermal expansion ellipsoid shown in figure 4.1.*

4.1.1 Absorption, emission and gain

The general concept of a cross section is used in various fields of physics to describe the probability of an interaction between two particles or between an electromagnetic wave and a particle. The cross section σ has the dimension of an area. Each ion may be pictured as a 'target' with this area, hit by a 'bullet' (e.g. a photon) with a probability w. The larger σ, the higher the probability that the 'target' is hit.

In a system of N laser active ions yielding energy levels E_1 and E_2 (with direct electronic transitions being allowed), absorption occurs upon excitation with radiation of energy $E_{\text{Photon}} = E_2 - E_1 = h \cdot \nu_{12}$. The change of the number of atoms in the ground state 1 is $\frac{dN_1}{dt} = -\sigma_{12} N_1 \phi$, with N_1 being the number of atoms in the ground state, ϕ the photon flux density (photons per area per time), and σ_{12} is the absorption cross section. The latter is related to the Einstein coefficient for the absorption B_{12} and to the absorption coefficient α by [92]

$$\sigma_{12} = B_{12} \frac{h\nu_{12}}{c} = \frac{1}{N_1} \alpha \ . \tag{4.1}$$

The above given equations are valid for two distinct energy levels. The lasers used in this work disobey this model as Yb^{3+}, $Cr^{4+}$and Tm^{3+} yield quasi-three-level behavior. In this case the ground and upper laser level are Stark manifolds composed of electronic sublevels of different energy. However, the concept of an *effective* absorption cross section, which incorporates the occupation probabilites and the transition cross sections for all sublevel transitions, is used to overcome this difficulty.

In contrast to the (effective) absorption cross section, which may be calculated from absorption spectra, determining the emission cross section is less trivial. For doing so either the Füchtbauer-Ladenburg equation or the McCumber theory (applying the reciprocity method) may be used. The former is used if the emission is not too broadband and given that the radiative lifetime of the excited state is known, it relates a measured fluorescence spectrum to the corresponding emission cross section by [110]

$$\sigma_{\text{em}}(\lambda) = \frac{\lambda_c^4}{8\pi c n^2 \tau_{\text{rad}}} \frac{I(\lambda)}{\int I(\lambda) d\lambda} \ . \tag{4.2}$$

Here $I(\lambda)$ denotes the fluorescence spectrum and λ_c the center wavelength of the emission. From equation 4.2 one can see that $\sigma_{\text{em}} \propto \left(\tau_{\text{rad}} \cdot \int I(\lambda) d\lambda\right)^{-1}$, hence, the broader an emission spectrum and the longer the upper state lifetime, the smaller the emission cross section.

[1] [−15] Values for the pristine laser host crystal. The values in brackets are determined for 2.4, 3.27, and 3.2 at. % Yb-doping, respectively [107]

The measurement of the radiative lifetime τ_{rad} is nontrivial due to reabsorption and internal reflection. Here one possibility is altering the measurement conditions (*e.g.*, by using diluted samples). The McCumber theory represents the second method for determination of σ_{em} [111, 112]. It relates the Einstein coefficients for broadband emission and absorption spectra and is therefore particularly useful for solid-state lasers yielding Stark manifolds. The McCumber relation reads [112]

$$\sigma_{\mathrm{abs}}(\nu) = \sigma_{\mathrm{em}}(\nu) \exp\left(\frac{h\nu - E_0}{k_B T}\right) . \tag{4.3}$$

The energetic positions of the individual Stark levels and their degeneracy are combined in E_0 [110, 111] and for certain laser active ions (e.g., Yb or Er), E_0 may be approximated by the zero phonon line, i.e., the transition between the lowest sublevels of the two Stark levels involved [113]. With knowledge of the absorption and emission cross section, it is possible to calculate τ_{rad} by means of the Füchtbauer-Ladenburg equation [111, 114, 115]. Furthermore, if the cross sections are known, the gain cross section is easily obtained by [108]

$$\sigma_{\mathrm{gain}}(\nu) = \beta_{\mathrm{inv}} \cdot \sigma_{\mathrm{em}}(\nu) - (1 - \beta_{\mathrm{inv}}) \cdot \sigma_{\mathrm{abs}}(\nu) . \tag{4.4}$$

With the inversion parameter β_{inv}, which is not to be confused with the dispersion parameters introduced in equation (4.7).

As an example, figure 4.2 shows the cross sections $\sigma_{\mathrm{abs}}(\nu)$, $\sigma_{\mathrm{em}}(\nu)$ as well as $\sigma_{\mathrm{gain}}(\nu)$ for the ${}^3\mathrm{F}_4 \rightarrow {}^3\mathrm{H}_6$ transition, on which the Tm^{3+}-doped KLuW laser operates. It can be seen that the cross sections are polarization dependent, and the curves are shown for polarization along two crystallographic axes. The plots show an overlap of the emission and absorption around the laser wavelength [Figure 4.2 (a)]. This behavior is characteristic for quasi-3-level systems and explains the higher laser threshold (compared to 4-level systems), which is due to this re-absorption of emitted radiation. Furthermore, the maximum of the gain and hence the central wavelength of the laser depend upon the population inversion in the laser crystal as apparent from Figure 4.2 (b). As higher output coupling demands for a higher inversion in the laser medium, different output coupling degrees result in different central wavelengths if all other laser parameters are fixed.

The gain cross section may be used to calculate the small signal gain coefficient by $g(\nu) = \sigma_{\mathrm{gain}}(\nu) \cdot \Delta N$, with the population density difference between the upper and lower laser level is $\Delta N = N_{\mathrm{upper}} - N_{\mathrm{lower}}$. The gain coefficient is found in the Lambert-Beer-law, relating the intensity of radiation I to the penetration depth z by $I(z, \nu) = I_0 \cdot e^{g(\nu) \cdot z}$.

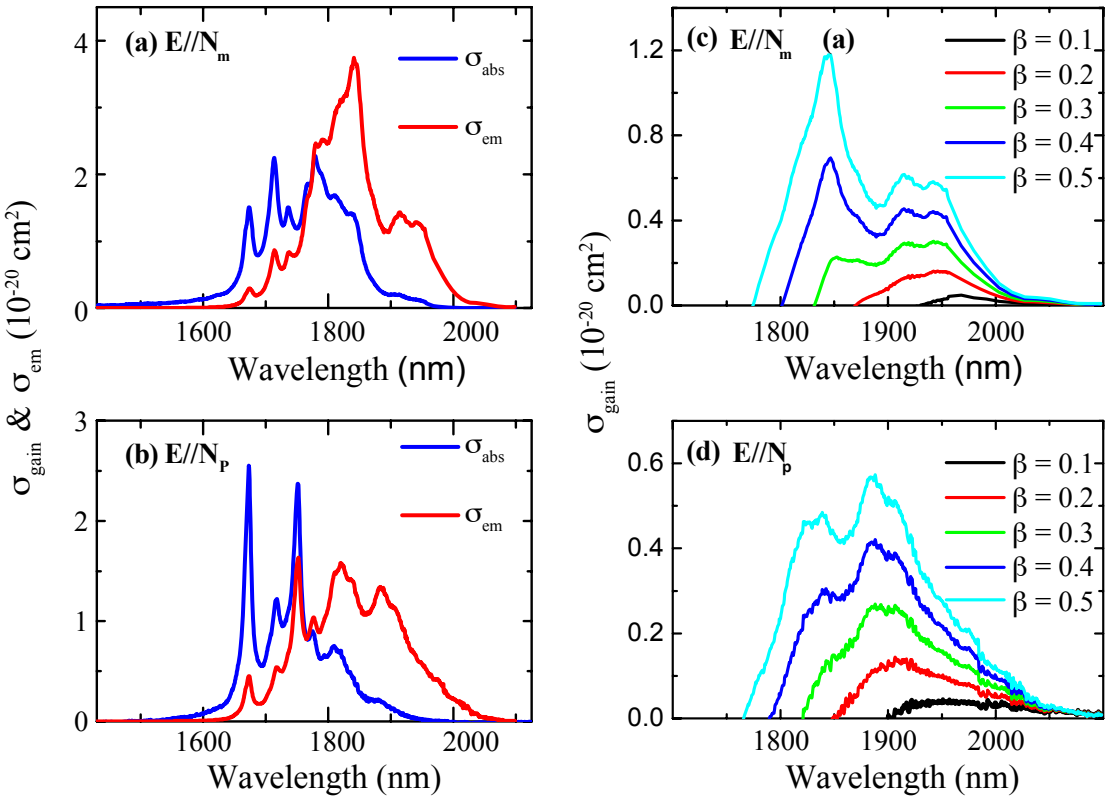

Figure 4.2: *(a) and (b) Absorption (blue) and emission (red) cross sections for the* ${}^3F_4 \rightarrow {}^3H_6$ *transition of Tm around 2 µmin KLuW for polarization parallel to* N_m *(a) and* N_p*(b), respectively. (c) and (d) Gain cross sections for the* ${}^3F_4 \rightarrow {}^3H_6$ *transition in Tm:KLuW according to equation* (4.4)*, given for the polarizations* N_m *(a) and* N_p *(b). Different inversion parameters* β *were assumed. Figure from [108].*

4.1.2 Gain saturation in the steady state

The gain introduced in the former section actually describes the behavior for small input intensities whereas the gain is actually a function of the photon flux density ϕ and consequently in a given geometry also a function of the fluence or intensity. The gain is given by [116]

$$g(\nu) = \frac{g_0}{1 + \frac{P}{P_{\mathrm{sat}}(\nu)}} = \frac{g_0}{1 + \frac{P \cdot \tau_g}{E_{\mathrm{sat}}(\nu)}} = \frac{g_0}{1 + \frac{\phi}{\phi_{\mathrm{sat}}(\nu)}} \ . \tag{4.5}$$

Here $P_{\mathrm{sat}}(\nu)$, $E_{\mathrm{sat}}(\nu)$, and $\phi_{\mathrm{sat}}(\nu)$ are the saturation power, saturation energy and saturation photon flux density, g_0 the small-signal-gain and τ_g the gain relaxation time, which is often close to the radiative lifetime. Equation (4.5) is valid in the steady state, *i.e.*, for long time scales, constant pump power and resonator losses. For different conditions, *e.g.*, for higher gain values as in amplifiers, the Frantz-Nodvick equation needs to be applied. The solid-state lasers used in this work yield a small emission cross section, as compared to dye lasers. With the gain saturation fluence being inverse proportional to the emission cross section ($F_{\mathrm{sat}} = \frac{h\nu}{\sigma_{\mathrm{em}} + \sigma_{\mathrm{abs}}}$), the lasers under study consequently yield a higher saturation fluence than dye lasers. Therefore, saturation of the gain by one single pulse may be assumed negligible.

In laser operation, *i.e.* in the steady-state, the gain of the active medium is saturated to a value such that the laser gain equals the losses. Consequently the average intracavity power remains constant, and the pulse is reproduced after each round trip.

4.2 Pulse shaping effects

4.2.1 Dispersion in dielectric materials

In dielectric media, the linear susceptibility $\chi(\omega)$, the refractive index $n(\omega)$ and the speed of light $c(\omega) = c_0/n(\omega)$ are frequency-dependent. Hence, different wavelengths experience temporal delay with respect to each other. Material dispersion can be defined by expressing the wave vector $k(\omega)$ as a Taylor series

$$k(\omega) = k(\omega_0) + \frac{1}{1!}\frac{\partial k}{\partial \omega}(\omega - \omega_0) + \frac{1}{2!}\frac{\partial^2 k}{\partial \omega^2}(\omega - \omega_0)^2 + \frac{1}{3!}\frac{\partial^3 k}{\partial \omega^3}(\omega - \omega_0)^3 + \cdots \ . \tag{4.6}$$

Introducing the dispersion coefficients $\beta_n = \frac{\partial^n k}{\partial \omega^n}$ and $\Delta\omega = (\omega - \omega_0)$, equation (4.6) is expressed as

$$k(\omega) = k(\omega_0) + \frac{1}{1!}\beta_1 \Delta\omega + \frac{1}{2!}\beta_2 \Delta\omega^2 + \frac{1}{3!}\beta_3 \Delta\omega^3 + \cdots \ , \tag{4.7}$$

respectively with the phase velocity

$$v_{\mathrm{ph}}(\omega) = \frac{\omega}{k(\omega)} \ , \tag{4.8}$$

and the group velocity

$$v_{\mathrm{g}}(\omega) = \frac{d\omega}{dk(\omega)} = \frac{c}{n(\omega) + \omega \frac{dn(\omega)}{d\omega}} \ , \tag{4.9}$$

the Taylor expansion of $k(\omega)$ around ω_0 is given by

$$k(\omega) = \frac{\omega}{v_{\mathrm{ph}}(\omega)} + \frac{1}{v_{\mathrm{g}}(\omega)}\Delta\omega + \frac{d}{d\omega}\left(\frac{1}{v_{\mathrm{g}}(\omega)}\right)\frac{\Delta\omega^2}{2} + \cdots \ . \tag{4.10}$$

The zero order term is a phase shift, and the first order term denotes the group delay (GD), which describes the delay between the pulse envelope and the carrier wave due to different group and phase velocities. The pulse shape and duration are not altered by the GD. The second order term is the group velocity dispersion (GVD), which introduces a phase difference between the spectral components of a pulse, leading to a temporal broadening. The GVD is a material parameter and if multiplied with the propagation length in a dispersive medium, the group delay dispersion (GDD) is obtained. GVD also results in a linear distribution of frequencies across the pulse (also called chirp), for instance to a leading *red* (low frequency) and trailing *blue* (higher frequency) component in the case of positive GVD. The increase in pulse duration for Gaussian pulses is given by [117]

$$\tau_1 = \tau_0 \sqrt{1 + \left(4 \ln(2) \frac{\beta_2 z}{\tau_0^2}\right)^2} \ , \tag{4.11}$$

with τ_0 and τ_1 being the full width at half maximum (FWHM) pulse duration before and after propagation through a medium, respectively. Equation (4.11) indicates that the broadening is independent on the sign of the chirp and GVD does not affect the original pulse shape of the propagating pulse. If a GDD of about $300\,\mathrm{fs}^2$ (corresponding to 3 mm propagation in a double tungstate) is assumed, pulse broadening becomes critical at pulse durations well below 40 fs [see figure 4.3(b)]. However, in a laser resonator, the pulse propagates for many roundtrips before being coupled out.

Therefore, even longer pulses experience significant dispersion and pulse broadening. The calculated GVD of the laser gain media and prism materials is shown in figure 4.3(a). The dispersion of KLuW (red) for polarization along the N_m - principal optical axis (*cp.* [108]) is plotted as a representative for other double tungstates together with lutetia (green).

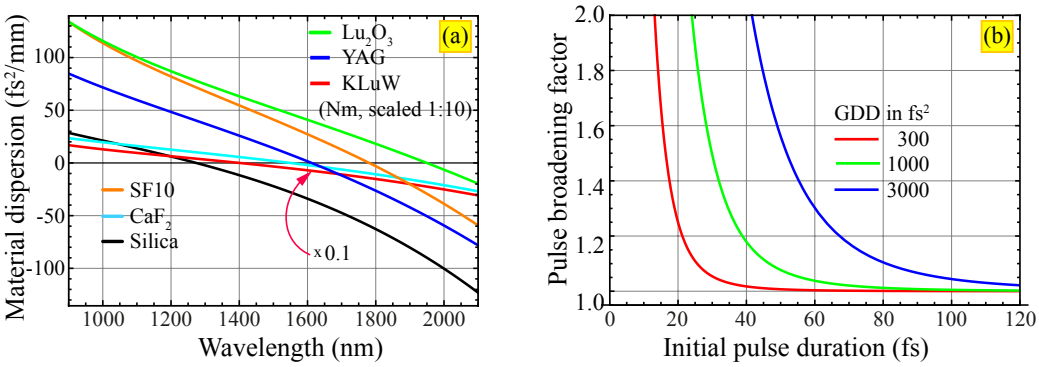

Figure 4.3: *(a) Calculated GVD for different materials in dependence of the wavelength. Please note that the GVD of KLuW is given for polarization along the Nm principal optical axis [108], and scaled by a factor of 0.1. (b) Pulse broadening in dependence of the initial pulse duration assuming a GDD of 300 (red), 1000 (green) and 3000 fs² (blue). A GDD of 300 fs² is introduced by a 3 mm thick KLuW crystal, and only pulses shorter than 40 fs experience significant broadening passing this crystal. In laser operation several round-trips easily sum up, higher GDD is obtained, and dispersion compensation becomes essential.*

Around 1 µm, the materials used in this work yield a positive GVD, turning negative between 1 and 2 µm. Lutetia features a GVD close to zero around 2 µm. The zero dispersion wavelength opens the possibility of pulse propagations with negligible pulse broadening, as *e.g.*, widely used in telecommunication around 1.3 µm in silica fibers. The dispersion is positive for the Yb host materials, slightly positive for the Cr host material, and negative in case of the Tm host materials. This becomes relevant during the discussion of solitary mode-locking in section 4.3.3.

In contrast to GVD, third order dispersion (TOD) as well as higher order dispersion influence the pulse duration *and* the pulse shape. TOD, *e.g.*, introduces oscillations after the main pulse for $\beta_3 > 0$ [118]. The TOD of a KLuW crystal oriented for N_m-polarization is approximately 200 fs³/mm at 1 µm and 1160 fs³/mm at 2 µm[4]. According to [117] the broadening factor is proportional to $\sqrt{1+\left(s\frac{\beta_3}{2\tau_0^3}\right)^2}$, and hence the pulse broadens by only 5% for pulse durations below 10 fs at 1 µm and 20 fs at 2 µm on passage of 1 mm KLuW. Consequently, TOD is negligible in the laser oscillators under study as they yield significantly longer pulse durations.

[4] in [118] a TOD of 30,000 fs³ is assumed for the example shown

4.2.2 Dispersion compensation

As explained later in section 4.3.3, stable mode-locked operation demands for a balance of positive intracavity material dispersion (section4.2.1) and negative dispersion introduced by SPM (subsection 4.2.3. Dispersion compensation within the laser cavity may be achieved by Gires-Tournois interferometers [119], dispersion compensating chirped mirrors [120], or a prism pair [121, 122]. Gratings are usually not applied inside a ultrashort pulse laser cavity, but may act as wavelength-selective element in narrow-band lasers [123, 124].

The dispersion compensating prism pair used in the laser cavities under study, allows for fine adjustment of the introduced amount of GDD, realized by a variable insertion of the second prism into the beam, which changes the optical path length through the tip of the prism, consequently varying the positive material dispersion introduced. This path may be defined conveniently by *(1)* the position of the center wavelength with respect to the tip of the second prism, *i.e.* the insertion [121] or *(2)* the horizon wavelength, which defines the shortest wavelength still passing the second prism, whereas shorter wavelengths do not enter the second prism at all [122].

The GDD introduced by one pass through the prism pair at the central wavelength λ_c, respectively the corresponding circular frequency ω_c, calculates by [122]

$$\left.\frac{d^2\Phi}{d\omega^2}\right|_{\omega_c} = -\frac{l\lambda^3}{2\pi c^2}\frac{d^2P}{d\lambda^2} \ . \tag{4.12}$$

Here l is the tip-to-tip distance (ttt-distance) and P denotes the optical path depending on the wavelength and the resulting angular dispersion for a given prism geometry. This derivative is given by [122]

$$\frac{d^2P}{d\lambda^2} = \beta'' \sin\beta + \beta'^2 \cos\beta \ , \tag{4.13}$$

with β being the second order material dispersion of the prism material. In the lasers under study the prism pair consists of either SF10 (below 2 µm) or calcium fluoride (CaF_2). The prisms used are cut for Brewster angle incidence to minimize reflection losses.

In figure 4.4, the GVD of the prism pairs made of SF10 and CaF_2 are calculated according to equations (4.9) and (4.13) for different ttt-distances.

4.2.3 Self phase modulation

Self phase modulation (SPM) is a nonlinear effect closely related to the optical Kerr-effect. The latter, however, is in general used to describe a *lateral* dependence of

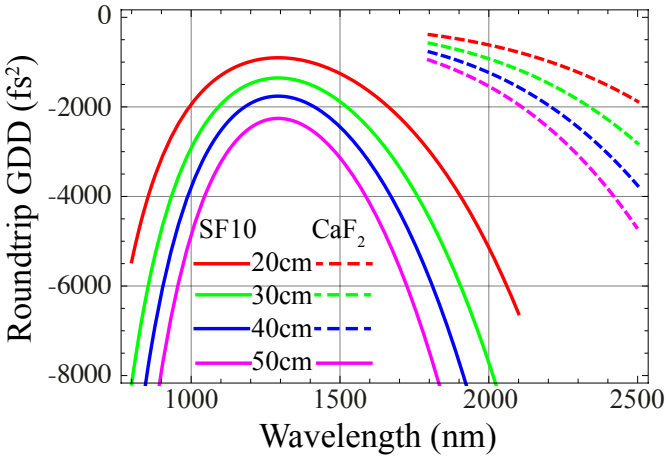

Figure 4.4: *Calculated GDD introduced by a pair of SF10 and CaF_2 prisms, respectively. The amount of negative dispersion is coarsely changed by the tip-to-tip distance of the prisms and may be fine-tuned by prism insertion. In the calculation according to [122], horizon wavelengths of $\lambda_{hor1} = 950\,nm$ and $\lambda_{hor2} = 1800\,nm$ were assumed for the SF10 and CaF_2 prism pair, respectively. As λ_{hor} denotes the shortes wavelength passing the prism pair, the curves are cut at λ_{hor2} for the CaF_2 prism pair.*

the refractive index due to a *lateral* intensity distribution. On the contrary, SPM is related to a temporal change in refractive index $\Delta n(t) = n_2 \cdot I(t)$ induced by the *temporal* intensity distribution of the pulse itself. Here n_2 denotes the nonlinear refractive index (in [cm^2/W]) and $I(t)$ the time dependent intensity of the laser pulse. It is to be noted that n_2 used in the following corresponds to $\overline{n}_2$ in [124]. With negligible third harmonic generation, the nonlinear refractive index is related to the third order susceptibility $\chi^{(3)}$ via [124]

$$n_2 = \frac{3}{4}\frac{1}{\varepsilon_0 c n_0^2}\chi^{(3)} \ . \tag{4.14}$$

Hence, during the temporal propagation of the pulse, different parts of it experience a different refractive index. This in turn leads to a time-dependent phase shift [116, 124]

$$\Delta\varphi(t) = 2\pi n_2 \frac{L}{\lambda_0} I(t) = \frac{\omega_0}{c} n_2 L I(t) = \gamma I(t) \ . \tag{4.15}$$

Here L denotes the propagation length in the medium, and λ_0 and ω_0 are the center wavelength, respectively frequency. The phase shift introduced by SPM results in a shift of the instantaneous frequency

$$\Delta\omega_{\text{inst}} = \frac{\partial}{\partial t}\Delta\varphi(t) = \frac{\omega_0}{c} n_2 L \cdot \frac{\partial I(t)}{\partial t} \ . \tag{4.16}$$

Figure 4.5 shows schematically a hyperbolic-secant pulse (*i.e.*, the temporal intensity profile is sech^2-shaped) and the corresponding nonlinear frequency shift due to SPM (prefactors not considered).

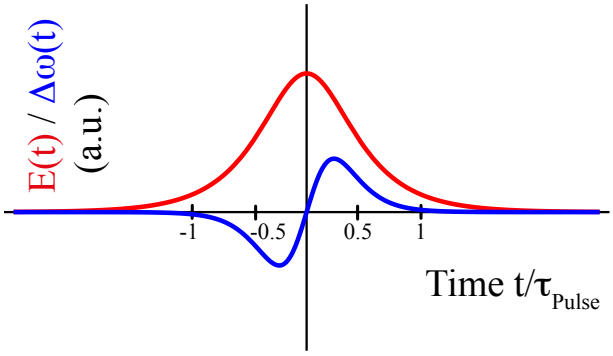

Figure 4.5: *Schematic of a sech^2-shaped pulse (red) and the change in frequency resulting from SPM induced by the pulse itself (blue).*

SPM consequently generates new frequencies and broadens the optical spectrum. Within the resonator, however, spectral filtering, *e.g.*, due to a finite gain bandwidth, limits this broadening. SPM applied externally, *e.g.*, in an optical fiber allows for the generation of very broadband radiation, the so-called supercontinuum or white light [125, 126].

For a positive nonlinear refractive index n_2, SPM introduces a positive chirp to an initially unchirped pulse. This chirp is approximatly linear for the central part of the the pulse (see figure 4.5). This fact becomes relevant in the following sections when solitary mode-locking is discussed.

4.3 Mathematical representation

4.3.1 The wave equation

To describe laser pulses, one may start from the wave equation

$$\left(\nabla^2 - \mu_0\varepsilon_0\frac{\partial^2}{\partial t^2}\right) E = 0 \tag{4.17}$$

and the complex representation of an electric light field

$$E(\mathbf{x},t) = \Re\left\{E_0(\mathbf{x},t)e^{ikx-i\omega_0 t}\right\} \ . \tag{4.18}$$

At first, the slowly varying envelope approximation (SVEA) is applied, *i.e.* the assumption is made, that the complex E-field amplitude $E_0(\mathbf{x}, t)$ changes slowly compared to the wavelength of the carrier wave. Consequently the second derivatives of $E_0(\mathbf{x}, t)$ are negligible compared to the first derivatives, $|\nabla^2 E_0| \ll |k\nabla E_0|$ and $\left|\frac{\partial^2 E_0}{\partial t^2}\right| \ll \left|\omega_0 \frac{\partial^2 E_0}{\partial t}\right|$[127]. The SVEA simplifies the second order differential equation to one of first order.

If moderate GVD and SPM (see sections 4.2.1 and 4.2.3) are assumed, using SVEA the wave equation (4.17) can be rewritten in the form of a nonlinear Schrödinger equation [128]

$$\left\{\frac{\partial}{\partial z} + \frac{i}{2}\beta_2 \frac{\partial^2}{\partial T^2} - i\delta\left|E(z,t)\right|^2\right\} E(z,t) = 0\ . \tag{4.19}$$

Here $T = t - {}^{z}/_{v_g}$ is the retarded time (the frame of reference is moving with the pulse maximum), $\beta_2 = \left(\frac{d^2k(\omega)}{d\omega^2}\right)_{\omega=\omega_0}$ is the GVD- and δ the SPM- coefficient.[5]

Equation (4.19) describes the transmission of electromagnetic waves in fibers and belongs to the class of Korteweg-de Vries equations. Apart from the solution in form of a uniform wave train, solitons represent a pulsed solution to those differential equations [132, 133].

4.3.2 From the NLSE to Haus' master equation

To describe a laser using equation 4.19, further assumptions and approximations need to be considered [129]:

1. Gain and loss of the active laser medium need to be incorporated and gain saturation may be omitted .

2. The linear and nonlinear change a pulse experiences within one roundtrip in the cavity, and hence the modification of the pulse by one passage of each optical component, is small ($< 20\%$).

3. In the steady state the pulse reproduces itself after one round trip in the resonator, i.e., $A(t) = A(t + T_R)$

[5] The notation of references [128] and [129] differ from each other. In [128] the SPM coefficient is γ, whereas it is δ in references from H. A. Haus [130, 131]. In this study Haus' notation is applied.

Those assumptions led to Haus' master equation, a model applicable to describe pulses circulating in a solid-state laser resonator considering pulse shaping effects. One representation of the master equation reads [129, 130][6]

$$\left[-i\psi - (l + iz) + g\left(1 + \frac{1}{\Omega_g^2}\frac{\partial^2}{\partial T^2}\right) + \cdots \right.$$
$$\left. iD\frac{\partial^2}{\partial T^2} + (q - i\delta)\left|a\right|^2\right]\mathcal{E}(T, z) = 0 \quad . \tag{4.20}$$

Here the different effects are implemented by the following differential operators [129, 130, 134]:

- $-i\psi$ is a small phase shift per resonator pass, induced by a shift of the carrier frequency.
- $-(l + iz)$ describes a small linear loss and phase shift per pass.
- $g\left(1 + \frac{1}{\Omega_g^2}\frac{\partial^2}{\partial T^2}\right)$ is a small gain acting on the field amplitude with the saturated gain g and the gain bandwidth Ω_g at half with at half maximum (HWHM). The ratio g/Ω_g^2 is called gain dispersion.
- $iD\frac{\partial^2}{\partial T^2}$ denotes the intracavity GDD,
- $q\left|a\right|^2$ the response of the saturable absorber, and
- $-i\delta\left|a\right|^2$ expresses SPM.

The master equation 4.20 may be expanded or simplified according to the effects present in the laser cavity, e.g., higher order dispersion that becomes relevant in sub-10 fs Ti:sapphire lasers (see e.g. [135] and references within). Under certain combinations of GVD and SPM, *e.g.*, if negative GVD is compensated by positive SPM, a soliton is one solution of the master equation.

4.3.3 The soliton

Real soliton propagation exists only in fibers. In a bulk laser the different contributions of SPM and GVD do not occur simultaneously. SPM emerges in the laser crystal, whereas the main contribution of GVD originates from the dispersion compensating prisms. However, the contributions balance each other within one roundtrip. Although, the pulse has a different shape at different positions in

[6] The response of the SA - originally labeled γ - is labeled q, according to [134]

the laser resonator, it reproduces itself after every roundtrip. Therefore it is more accurate to call this pulsed regime *solitonlike* or *solitary* mode-locking.

The temporal intensity profile $P(t)$ and the optical spectrum $S(\nu)$ of the pulse have the shape of a squared hyberbolic secant (sech^2) and this solution yields the following properties:

- The intracavity GDD (D), SPM (δ) and the pulse energy (E_P) are related to the full width half maximum pulse duration τ_{FWHM} by [117, 136]

$$\tau_{\mathrm{FWHM}} = 1.76 \cdot \frac{4\,|D|}{\delta E_P} \ . \tag{4.21}$$

- The time-bandwidth-product (TBP) relates the spectral bandwidth and pulse duration obtained. For sech^2-pulses the theoretical limit for the pulse duration at a given spectral bandwidth calculates to $\mathrm{TBP}_{\mathrm{lim}} = \Delta\nu \cdot \Delta\tau_{\mathrm{FWHM}} = 0.315$.

- The intensity autocorrelation function $G_2(\tau)$ of a sech^2 shaped pulse is described by [137]

$$G_2(\tau) = \frac{3\,(\tau \cdot \cosh(\tau) - \sinh(\tau))}{\sinh^3(\tau)} \ . \tag{4.22}$$

  In practical applications fitting $G_2(\tau)$ with a sech^2 and division of the autocorrelation width $\tau_{\mathrm{ac,FWHM}}$ by approximately 1.54 yields a very good first estimate of the pulse duration $\tau_{\mathrm{FWHM}} \approx 0.66 \cdot \tau_{\mathrm{ac,FWHM}}$.

- Solitons of higher order are possible solutions of the Haus master equation. While the fundamental soliton of order 1 is neither varying its pulse shape nor spectrum during propagation, higher order solitons change their shape and spectrum with the soliton period [117].

- Solitons are subject to TOD and nonlinear effects, self-steepening and intrapulse Raman scattering, which is also called the self-frequency shift [117]. In the case of propagation in fibers, those effects need to be incorporated, however, interaction lengths in the elements of the laser resonator are too short to see those effects.

The first two properties are most relevant for solid state lasers yielding solitary mode-locking. The third point concerning the stability is partially re-assessed within the following sections, discussing the net gain window and the stability against the continuum, respectively the stability against pulse-breakup.

For assessment of the solitary character of the results, the shape of the autocorrelation and the optical spectrum may be considered. If the former deviates from

the autocorrelation of a sech^2 shaped pulse, solitary mode-locking may be excluded. The same conclusion may be drawn if the optical spectrum does not feature a sech^2 shape. A further indication for solitary mode-locking is a TBP close to the theoretical limit of 0.315 for this pulse shape. If the achieved TBP does not deviate too much (i.e., <20 %) from the Fourier limit, the pulses are assumed solitary.

For a more quantitative assessment of the presence of a soliton, the 'soliton condition' according to [116], is applied. The effects of GVD and SPM (sections 4.2.1 and 4.2.3), introduce a phase to the pulse traveling in a non-linear optical medium. The pulse propagates in the form of a soliton, if the contributions to the phase by GVD and SPM yield the same absolute value and the opposite sign. The soliton condition in [116] needs to be adapted for bulk lasers by changing over the left hand side of equation (4.23) to the B integral [138] and integration of the right hand side as well. Different contributions occur at different positions z on the beam axis, which is taken into account by integration over one round trip in the cavity.

$$k_0 \int_{\text{cav}} n_2(z) I_0 \mathrm{d}z = \int_{\text{cav}} -\frac{\beta_2}{\tau_\text{p}^2} \mathrm{dz} \tag{4.23}$$

The angular wave number of the center wavelength $k_0 = \frac{2\pi}{\lambda_0}$, the nonlinear refractive index $n_2(z)$ of the non-linear material (in $[\frac{cm^2}{W}]$) and the pulse peak intensity I_0 compose the phase factor stemming from SPM.

The right-hand side of equation (4.23) includes the group velocity dispersion coefficient β_2 and the pulse duration τ_p, and integration yields a dimensionless expression on both sides of the equation.

This approach considers the fact that SPM and GVD do not occur at the same time and position. SPM is mainly present in the active laser medium, whereas GVD is introduced by the prism pair and the active laser medium. Consequently the term on the left hand side may be integrated over twice the crystal length, whereas the solution of the right hand side is determined by the GDD of the prism and the overall material dispersion of two passes through the laser active material. In general, the path through the prism sequence is not exactly known. Thus, the GVD introduced by the prism pair may be miscalculated, leading to an (mainly) overestimation of the amount of negative GVD. Finally, the calculation of SPM demands for accurate knowledge of the nonlinear refractive index and the average laser beam area of the active laser material.

4.4 Saturable absorber and net-gain-window

In general, an optical component (transmittive or reflective) whose losses are reversibly decreasing with increasing incident optical intensity is referred to as SA. The nonlinear transmission behavior (section 3.3 on page 32) describes the loss as a function of energy. The temporal behavior was neglected so far.

Fast and slow saturable absorbers

SAs yielding a relaxation time n the order of or shorter as the pulse duration of the laser are considered fast, and the losses may be modeled by [136]

$$q(T,\,t) = \frac{q_0}{1 + \frac{|A(T,\,t)|^2}{P_A}}\ , \tag{4.24}$$

with the linear loss q_0, and the SA saturation power P_A. SAs with a longer relaxation time are called slow absorbers[7].The absorption of a slow absorber may be expressed by a rate equation including the saturation energy E_A [136]

$$\frac{dq(T,\,t)}{dt} = -\frac{q - q_0}{\tau_A} - q\frac{|A(T,\,t)|^2}{E_A}\ . \tag{4.25}$$

A fast absorber 'follows' the temporal pulse profile in contrast to a slow absorber, that - once saturated by a short pulse - still shows a certain degree of saturation after passage of the pulse. Consequently, the net gain window, which correlates with decreasing cavity losses, is opened only during the pulse for a fast absorber [Figure 4.6(a)], but stays open longer than the pulse duration in case of a slow absorber [Figures 4.6(b) and (c)]. *Per se*, one may assume that a long net gain window, which remains open after the trailing edge of the pulse, allows the noise following the pulse to grow and ultimately degrades the discrimination of the pulse against this noise (also called 'continuum'). Yet, some effects may counteract the long net gain window. One effect temporally limiting the net gain window and increasing the stability against the noise is gain saturation of the laser medium. This effect is, for instance, observed in dye lasers and depicted in figure 4.6(b). In this case one pulse already extracts sufficient energy from the gain medium to saturate the gain even before the pulse completely passed the gain medium. Solid state lasers, on the contrary, yield only negligible gain saturation. Consequently, a long net gain window was assumed to render pulsed laser operation unstable [139]. Kärtner et al. [81] showed that soliton formation may stabilize pulsed operation against the continuum because the continuum experiences mainly two effects:

[7] The reference is the pulse, therefore a slow absorber for a fs-laser may represent a fast absorber for a picosecond-laser.

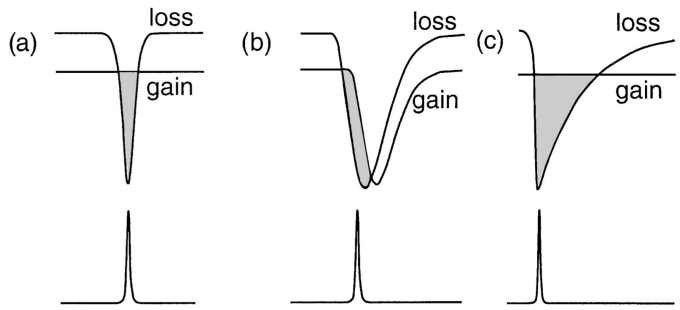

Figure 4.6: *The net gain windows for different combinations of relaxation times of the saturable absorbers and gain media. The loss and gain are drawn in the upper panel and the lower panel shows the pulse. The combinations are (a) a fast absorber, (b) a slow absorber in combination with gain saturation of the active laser material, and (c) a slow absorber with soliton pulse shaping. Figure from [81].*

(1) It undergoes temporal broadening, because the low intensity continuum still experiences GVD, whereas the (intensity dependent) dispersion due to SPM is not sufficient to compensate for this material dispersion.

(2) The pulse is retarded with respect to the continuum during every passage through the SA. As a result, the continuum precedes the pulse, such that the former propagates through a completely recovered and hence lossy SA.

The SWCNT-SAs used in this work yield a recovery time on the order of 70 and 100 fs for 1.0 and 1.2 µm, respectively. At 1.5 µm a recovery time of about 300 fs was determined, and at 1.9 µm a fast relaxation of about 250 fs was measured. Graphene yields a recovery time of about 200 fs at 1 µm. As chapter 5.1.4 shows in more detail, pulse durations obtained are in the order of 80 - 100 fs, implying that the SWNCT-SAs may be considered *fast* for 1 and 1.2 µm, but rather *slow* for the Cr:YAG laser at 1.5 µm. In the wavelength range around 2 µm the SWCNT-SA may be regarded *fast*, except for two results, where pulse durations of 175 and 145 fs were obtained. Those are in the order and at ≈50% of the recovery time, respectively. The graphene-SA may still be considered 'fast'. This evaluation becomes relevant in the following section concerning mode-locking stability.

4.5 Mode-locking stability

4.5.1 Q-switch mode-locking instabilities

Apart from the stability of the mode-locked operation against the continuum, Q-switching instabilities represent a delicate issue in laser operation. One refers to Q-switched mode-locking (QML) if the pulse train of the cw mode-locked laser experiences an additional amplitude modulation. This modulation stems from the capability of energy storage (and ultimately its sudden *release*) in active laser media with long upper state lifetimes. QML in bulk solid-state lasers yield a characteristic frequency of several ten kilohertz and shows itself as side-bands of the beat notes in the radio-frequency spectrum. Figure 4.7 schematically illustrates QML in comparison to cw mode-locking.

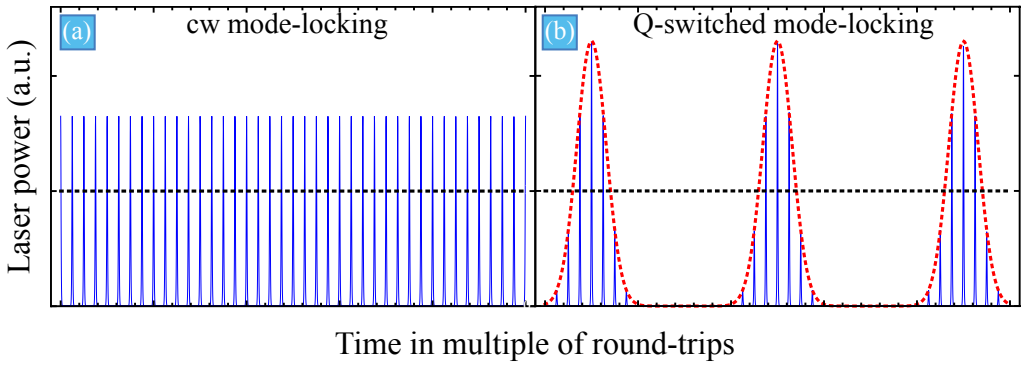

Figure 4.7: *Schematic of a cw mode-locked laser (a) and a laser showing Q-switched mode-locking (b). The average output power (black dotted line) of both lasers is identical but pulse energies are increased in case of QML.*

It is possible to deduce Q-switching stability limits from the rate equations for gain and loss. This assessment by Hönninger et al. [88] relates accessible laser and SA parameters to a critical pulse energy for stable cw mode-locking. One form of the stability criterion reads

$$E_P^2 \;>\; E_{\mathrm{sat,\,L}}\, E_{\mathrm{sat,\,A}}\, \Delta R\ . \tag{4.26}$$

With the saturation energy of the gain $E_{\mathrm{sat,\,L}}$, the saturation energy of the SA $E_{\mathrm{sat,\,A}}$ and the modulation depth of a reflective SA ΔR. The latter may be replaced by ΔT if a transmissive device is used. The saturation energies can be expressed by $E_{\mathrm{sat}} = F_{\mathrm{sat}} \cdot A_{\mathrm{eff}}$, whereupon the effective area of the laser mode in the crystal or on the SA is $A_{\mathrm{eff,\,L/A}} = \pi w_{\mathrm{L/A}}^2$. The cavity parameter w is the beam waist and

additionally, a tilt of the element due to Brewster alignment has to be considered. To derive equation 4.26 several approximations have been assumed [88]:

- The SA recovery time is shorter than the roundtrip time $\tau_A < T_R$
- ΔR of the SA is small and the nonsaturable losses of the SA are negligible
- The SA is strongly bleached, i.e., $F_P \geq 5 \cdot F_{\text{sat, A}}$
- The laser operates far above threshold

It is convenient to combine $E_{\text{sat,L}}$, $E_{\text{sat,A}}$ and ΔR to the QML parameter β_{QML}[8] and write for $E_{\text{P, crit}}$

$$E_{\text{P, crit}} = \sqrt{\beta_{\text{QML}}} \ . \tag{4.27}$$

Figure 4.8 shows the stability regions for the pulse energy in dependence of the QML parameter. The solid curve represents the critical pulse energy, with the blue shaded region indicating cw mode-locking, whereas for a combination of pulse energy and QML parameter lying in the red shaded region, Q-switching instabilities are expected. This model is a fairly good assessment of the cw mode-locking threshold

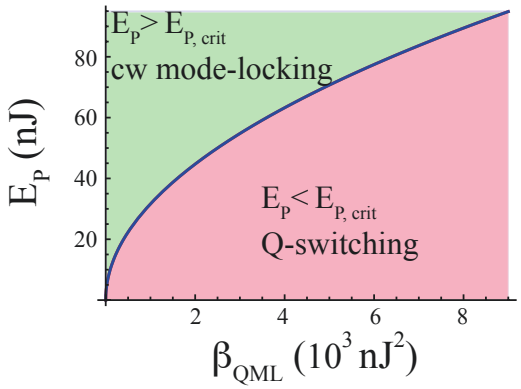

Figure 4.8: *Calculated critical pulse energy for stable cw mode-locking versus QML parameter (black solid line). The blue shaded region indicates cw mode-locked operation, whereas in the red shaded region Q-switching instabilities are expected.*

for picosecond lasers, whereas for solitonlike mode-locking the extended criterion reads [88]

$$\left(\frac{g_{\text{eff}}}{g} - \frac{\mathrm{d}g_{\text{eff}}}{\mathrm{d}E_P} \right) \Bigg|_{E_{\text{P}}} E_P^2 \ > \ E_{\text{sat, L}} \, E_{\text{sat, A}} \, \Delta R \ , \tag{4.28}$$

with the effective gain g_{eff}. The prefactor reduces the critical pulse energy for cw mode-locking and decrease its threshold[9]. In this modified criterion, the high

[8] this labeling is not applied in literature, but done for convenience

stability of the soliton mentioned before (section 4.3.3) may be quantified. It should be noted that the condition in equation 4.26 is stricter than in equation 4.28, i.e., lasers fulfilling the stricter condition consequently fulfill the weaker condition as well. The extension for solitons may be considered if equation 4.26 is not fulfilled by a soliton-like mode-locked laser. Either of the two QML criteria is considered during the analysis of the experimental results.

4.5.2 Pulse-breakup

In general, single pulse operation is preferred over double- or multi pulsing. Pulse breakup into two or more pulses is unwanted because this solution is not stationary any longer, and the pulses are moving with respect to each other.

If soliton-like pulse shaping effects are dominant, the FWHM pulse width is inversely proportional to the pulse energy [117, 136]

$$\tau_{\mathrm{FWHM}} = 1.76 \cdot \frac{4\,|D_{\mathrm{g,f}}|}{\delta E_P} \ . \tag{4.29}$$

$D_{\mathrm{g,f}}$ denotes gain and filter dispersion and δ is the SPM coefficient. If the pulse energy rises to a level where the SA is completely saturated, no further pulse shaping due to the SA occurs. SPM, on the contrary, does not saturate and results in further pulse shortening according to equation (4.29), which in turn implies a broadening of the optical spectrum. After a certain increase of the spectral bandwidth, the spectrum is subject to gain filtering due to a finite gain bandwidth. The losses for single pulse operation increase. If E_P increases and pulse breakup occurs, the two pulses have a lower pulse energy each, subsequently a longer pulse duration, as well as a narrower bandwidth. The latter decreases the losses due to the finite gain and filter bandwidth. The SA, which was very strongly saturated by the single pulse, is still strongly saturated by two less intense pulses. Ultimately, pulse breakup occurs, if the loss experienced by the double-pulse solution is smaller than the one for the single-pulse.

Kärtner et al. [136] found that a fast SA strongly increases the stability of mode-locking against pulse breakup. This may be explained by the fact that a fast SA saturates with peak power and a slow SA with energy. If a pulse breakup is assumed with $E_{\mathrm{pulse,2}} = 0.5 \cdot E_{\mathrm{pulse,1}}$, the pulse duration according equation 4.29 is $\tau_{\mathrm{FWHM,2}} = 2 \cdot \tau_{\mathrm{FWHM,1}}$. The peak power for the double pulse solution is hence reduced by a factor of 4, whereas the sum of the two pulse energies equals the energy of the single-pulse solution. As a slow absorber saturates with energy, the saturation of

[9] in [88] the factor is about 4 for experiments with Nd:glass

the SA is similar for single- and double-pulsed operation. In contrast to the fast absorber, saturating with peak power. Here the discrimination of single-pulsed operation against the double-pulsed solution due to the SA is increased compared to a slow SA.

As the SAs used in this work yield a recovery time which is in the order of the pulse duration, it was expected that multi-pulsing is less critical for the lasers under study. Nevertheless, if the saturation parameter $S = \frac{F_\mathrm{i}}{F_\mathrm{sat}}$ reaches values $\gtrapprox 10$, pulse breakup is anticipated [136, 140].

With respect to pulse breakup, the higher gain saturation fluence of the active laser materials under study is beneficial for single-pulse operation as well.

4.6 Carbon nanostructure mode-locking – State of the art

Before showing the results obtained in this work, the introductory part of this chapter gives a brief overview of bulk lasers that have been mode-locked using nanotube-based saturable absorbers. For a convenient comparison all results obtained with SWCNTs – including those presented later in this chapter – are listed in table 4.2. The classification according to lasing wavelength is further arranged in chronological order of publication. The main laser parameters and references are given in the table. Fiber lasers were the first lasers mode-locked with carbon nanostructures and are numerously present in literature. However, table 4.2 excludes fiber lasers as this laser type has not been part of this work. The latter tolerate much higher non-saturable losses of up to 15 %, which is not comparable to the requirements of the quasi-three-level bulk lasers, that are under study in this work.

Wavelength range	Active laser material	Center wavelength in nm	Pulse duration in fs	Average output power in mW	Repetition rate in MHz	Type of carbon nanostructure	Reference	This work
0.8 µm	Ti:sapphire	810 / 800	600 / 62	45 / 600	110 / 99.4	H (R) / (T)	[103, 141]	
1 µm	Nd:phosphate glass	1054	≈ 200	—	—	H (R)	[142]	
	Yb:KLuW	1048	115	30	89	A (T)	[91]	⊠
	Yb:KYW	1038 / 1049	140 / 83	32 / 24	88 7 84	A (T) / (R)	[143]	⊠
		1038	133	160	87	H (T)	[75]	⊠
	Nd:silicate glass	1070	99	10	194	A (R)	[144]	
	Nd:BYF	1049	8500	70	194	A (R)	[145]	
	Yb:KLuW	1069	84	62	89	H + A	[80]	⊠
	Nd:YAG ceramics	1064	8300	130	90	H (R)	[146]	
	$Nd:GdVO_4$	1063	8400	3630	122	A (T)	[147]	
	$Nd:Lu_{0.15}Y_{0.85}VO_4$	1064	19000	902	150	A (T)	[148]	
	$Yb:Sc_2SiO_5$	1061	880 / 5400	712 / 940	96 / 103	A (R)	[149]	
1.3 µm	$Cr:Mg_2SiO_4$ † (forsterite)	1245 / 1250	120 / 80	202 / 295	79 / 78	H (T) / (R)	[150, 151]	⊠
		1242	100	230	79	H (T)	[75]	⊠
		1243	118	250	79	H + A (T)	[80]	⊠
	$Nd:YVO_4$	1342	16500	800	127	H (T)	[152]	
1.5 µm	Er, Yb:phosphate glass	1570 / 1562	68 / 261	≈30 / 63	85 / 75	L (R)	[94, 142]	
	Cr:YAG	1495	92	110	85	H (T)	[75, 153]	⊠
		1485	113	85	85	H + A	[80]	⊠
2 µm	Tm:KLuW	1944	9700	240	126	A (T)	[154]	⊠
		1942	25400	167	130	H + A (T)	[80]	⊠
	$Tm:Lu_2O_3$	2070	175	36	88	A (T)	[155]	⊠
	Tm:KLuW	2037	141	26	88	A (T)	[156]	⊠

Table 4.2: *State of the art of SWCNT-SA mode-locked bulk lasers.* ♢ † *- Forsterite lasers operated at Ajou University, Suwon, South Korea. Abbreviations used: H - HipCO, A - arc, L - Laser ablation, T - transmission, R - reflection*

SWCNT-SA mode-locked lasers were numerously presented in literature (see, e.g., table 4.2), whereas there is still only a limited number of graphene mode-locked bulk lasers demonstrated. Those bulk lasers mode-locked using graphene or graphene oxide as mode-locker are listed in table 4.3. The table includes the results presented in this work, marked accordingly. The classification is arranged in chronological order of publication, giving the main laser parameters and references. The first laser mode-locked by graphene was an erbium-doped fiber laser [10] using graphene samples characterized by an undefined number of layers. The graphene-polymer composites and graphene flakes were produced by exfoliation or CVD, and deposited directly onto fiber ends, and the laser generated output powers in the mW range [10, 157–159]. The SAs used in those fiber lasers yield large scattering losses, which, however, may be compensated by the large gain of fiber lasers of several ten dB. Such high-loss SAs are not appropriate for mode-locking of bulk lasers.

Table 4.3: *State of the art of graphene mode-locked bulk lasers. Absorber are used in transmission (T) or reflection (R). 'GO' denotes graphene oxide, 'CVD' graphene synthesized by chemical vapor deposition, and 'exfol' graphene produced by exfoliation of graphite.* ◊ † *- The Cr:forsterite lasers were operated at Ajou University, South Korea.* ◊ ‡ *- Estimated values by the authors of [160].*

Active laser material	Center wavelength in nm	Pulse duration in fs	Average output power in mW	Repetition rate in MHz	Type of graphene saturable absorber	Reference	This work
ceramic Nd:YAG	1064	4000	100	90	GO (T)	[161]	
Er,Yb:glass	1552	260	4.5	88	CVD (T)	[162]	
Nd:$GdVO_4$	1065	16000	360	43	exfol (R)	[163]	
Cr:Mg_2SiO_4	1250	94	230	75	CVD (T)	[100]	☒†
Yb:KGW	1031	428	504	86	exfol (R)	[164]	
Tm:$YAlO_3$	2023	≈ 10,000 ‡	268	72	GO (T)	[160]	
Ti:sapphire	800	63	480	99.4	CVD (T)	[44]	
Tm:CLNGG	2018	729	60	99	CVD (R)	[165]	
Yb:KLuW	1047	160	47	93	CVD (T)	[166]	☒
		203	160				
ceramic Tm:Lu_2O_3	2067	410	270	110	CVD (T)	[167]	
Cr:YAG	1516	91	107	85	CVD (T)	[168]	☒

Chapter 5

Results

5.1 Absorber Characterization

5.1.1 Pump-probe spectroscopy - methods

The carrier population and its relaxation dynamics are examined with pump-probe spectroscopy, wherein a pump pulse excites the sample and changes the population distribution of charge carriers. The probe pulse is used to investigate these changes.

The measured quantity of a pump-probe experiment is the differential transmission change $\frac{\Delta T(h\nu)}{T_0}$ and by variation of the time delay Δt between pump and probe pulse using a delay stage, the differential transmission change is temporally resolved.

In a non-degenerate or 'two-color' pump probe experiment, the pump and probe pulse are centered at different wavelengths. This allows monitoring the dynamics of carriers in a subband different than the one excited. For the purpose of mode-locking at a given laser wavelength, the degenerate case of pump-probe measurements is of interest. Here pump and probe are commonly two replica stemming from one and the same laser source.

Figure 5.1 schematically shows the measurement setup. The laser output is split into pump and probe beam, and the former beam is modulated by a chopper. The resulting modulation of the probe intensity is then recovered by lock-in detection. It is absolutely mandatory to prevent any stray light from reaching the photo detector. To some extent, this is accomplished by using a sufficiently large crossing angle of the two beams on the sample. This measure alone does not suffice to suppress stray light. Therefore one typically cross-polarizes pumpt and probe beam and blocks direct detection of the pump beam by a polarizer. For reflective samples, cross-polarization

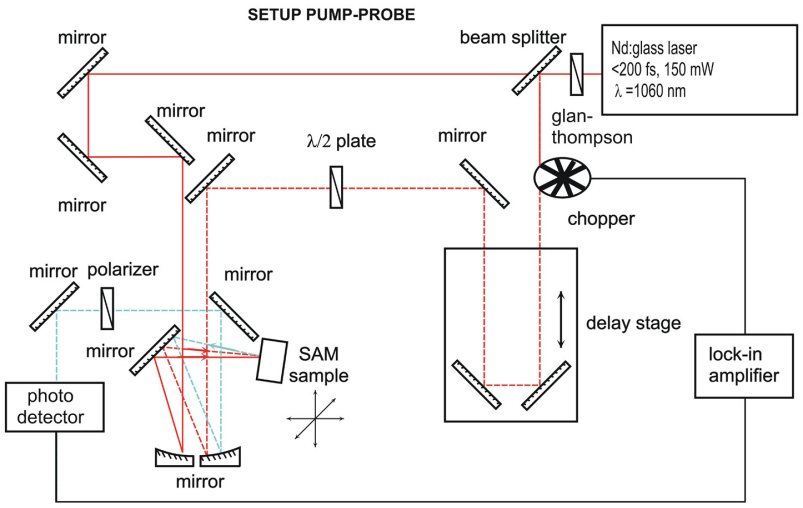

Figure 5.1: *The pump-probe setup to measure the relaxation time of different types of SAs. The setup shown is used for measurements of reflective SAs at 1 µm. For different spectral regions, the laser source and eventually optics have to be adapted to the changed wavelength of interest. The solid red line represents the pump and the dashed red line the probe. The blue dashed line is the probe pulse after reflection. The rate of the pump lasers used is on the order of 100 MHz.*

typically yields pump-probe traces that do not show any indication of a coherent artifact near zero delay [169].. For transmissive samples, however, a depolarization in the sample is sometimes observed. this effect can lead to interference effects near zero delay, which may result in strongly fluctuating signals in this range. These effects can be suppressed by measuring pump-probe traces with a constantly changing pump-probe delay. Adjusting the time constant of the lock-in amplifier to suppress the resultiing oscillations then serves to reject this artifact.

In pump-probe experiments, the minimum obtainable time resolution is dictated by cross-correlation between pump and probe pulse. If the cross-correlation function is known from independent measurements, this information can be utilized for a deconvolution of pmp-probe measurements. The reliability of such a deconvolution srongly depends on the signal-to-noise ratio of the available data. Even for near-perfect data, one cannot reliably retrieve dynamic effects on time scales that are about a factor 2 to 3 shorter than the pulse durations. Therefore, deconvolved traces have to be interpreted with a lot of care.

The absorption change in a semiconductor is given by [82]

$$\Delta\alpha(h\nu) = -\alpha_0(h\nu)\,(f_\mathrm{e} + f_\mathrm{h}) \ , \tag{5.1}$$

with the density functions of electrons and holes f_e and f_h and the small signal

absorption α_0. The absorption change is connected to the differential transmission by $\frac{\Delta T(h\nu)}{T_0} \approx \frac{\Delta\alpha(h\nu)}{\alpha_0}$, allowing to relate the property of interest, *i.e.*, the carrier density distribution to an observable and measurable property of the absorber. Equation (5.1) illustrates that *(a)* the sum of the density functions of electrons and holes (f_e and f_h) is easily accessible by the absorption change, and that *(b)* using the small signal absorption α_0 is not valid for higher excitation densities, as the absorption will saturate with incident fluence (section 3.3).

As presented in section 3.1.1, three main steps of relaxation are expected in semiconductors, exitation into the conduction band and subsequent ultrafast thermalization, intraband relaxations occurring on a femtosecond-timescale and interband relaxations on a picosecond timescale. Thermalization is not measurable with the pump sources used in this work. Therefore, the two relaxation processes expected to be resolvable are incorporated into the relaxation model described by a biexponential decay, which reads

$$\frac{\Delta T}{T}(t) = \mathrm{A} \cdot \exp\left[-\frac{t}{\tau_1}\right] + \mathrm{B} \cdot \exp\left[-\frac{t}{\tau_2}\right] . \tag{5.2}$$

Even if the system under study yields only one recovery time due to a relaxation process and an additional measurement artifact, *e.g.*, a coherence artifact, the biexponential fit will separate both from each other. As coherence artifacts are strongly reduced for reflective samples, comparing the pump-probe measurements of equally produced reflective and transmittive samples indicates whether the short time constant retrieved from the measurement is related to a relaxation process in the sample *or* to an artifact.

The relative weight of the time constants

If the differential transmission change of the SA is fit by (respectively the pump pulse convolved with) the biexponential model function of equation (5.2), it is possible to figure out the amplitude weights $w_{\mathrm{amp},1} = \frac{A}{A+B}$ and $w_{\mathrm{amp},2} = \frac{B}{A+B}$. However, as explained in the following, the contributions from the different relaxation times are of special interest with respect to self-starting and the suppression of the continuum (see section 4.4). Therefore the integral weight holds a higher importance. If the model function is slightly modified, resulting in

$$\frac{\Delta T}{T}(t) = 1 \cdot \exp\left[-\frac{t}{\tau_1}\right] + \mathrm{B'} \cdot \exp\left[-\frac{t}{\tau_2}\right] , \tag{5.3}$$

the integral weight of the slow relaxation time is $w_{\mathrm{int},2} = \frac{\mathrm{B'}\cdot\tau_2}{\tau_1+\mathrm{B'}\cdot\tau_2}$. For most SESAMS, *i.e.* not for the fast ones [170], only the slow relaxation time is specified, and

according to equation (5.3) an integral weight of $w_{\mathrm{int},2} \approx 100\,\%$ is obtained for such slowly relaxing systems.

5.1.2 Nonlinear transmission measurement - methods

In linear transmission measurements, the transmission is determined as a function of wavelength for small signal intensities. Nonlinear transmission (NLT) measurements, by contrast, focus on the transmission at a fixed wavelength or wavelength range as a function of the incident signal intensity.

They allow to determine macroscopic observable properties of the SA, like *e.g.*, the nonsaturable losses, the modulation depth, and the saturation fluence, introduced in section 3.3 on page 32.

Measuring the NLT of an SA is challenging, as sub percent changes in the transmission or reflection of a sample need to be detected over a fluence range of three orders of magnitude. In order to measure the NLT of the nanostructure-SAs, a setup similar to the one reported in [87] is used. Figure 5.2 depicts the NLT measurement setup used in this work. It repetitively scans the nonlinear transmission characteristics of the sample. An acousto-optic modulator is used for high-dynamic range attenuation. It allows for a precise variation of the incident fluence. Furthermore, each point of the measurement is referenced with a signal reflected by a silver mirror. This procedure is necessary to eliminate long term drift of the laser source as such a drift of the pump laser fluence may strongly falsify the measured transmission or reflection change. By these means, resolving modulation depths well below 1% is feasible. The measured data is subsequently fitted by the model function of equation (3.2).

5.1.3 Pump-probe spectroscopy - results

The pulsed laser sources used in the pump probe experiments are a 200 fs mode-locked Nd:glass laser operating at 1.06 µm (High Q Lasers), a 150 fs Er:Yb:glass laser at 1.56 µm (Origami by Onefive) and a femtosecond optical parametric oscillator (OPO) with ≈150 fs pulses (Opal by Spectra Physics). The signal, respectively idler output of the OPO were tunable to 1.3 and 2.0 µm. Consequently, the time resolution for the pump-probe experiments is in the order of 200 to 290 fs without applying the convolution method.

Figure 5.3(a) shows four pump trace signals measured for the same SA at different wavelengths. The sample used for these measurements is based on HipCO-made

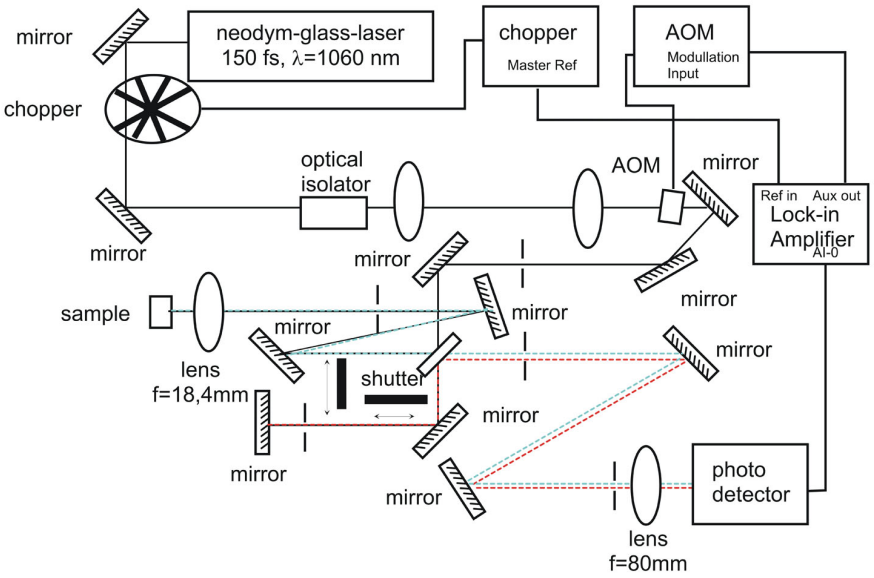

Figure 5.2: *The set-up for the non-linear transmission measurement. The pump laser is chopped as the lock-in technique is used for detection. The optical isolator prevents back-reflections into the laser source and the acousto-optic modulator allows for attenuation of the laser source over a high dynamic range. The assembly of shutters allows to switch between the sample arm and the reference arm including the silver mirror. Thus each data point is timely referenced, which minimizes errors due to long-term drift of the pump laser.*

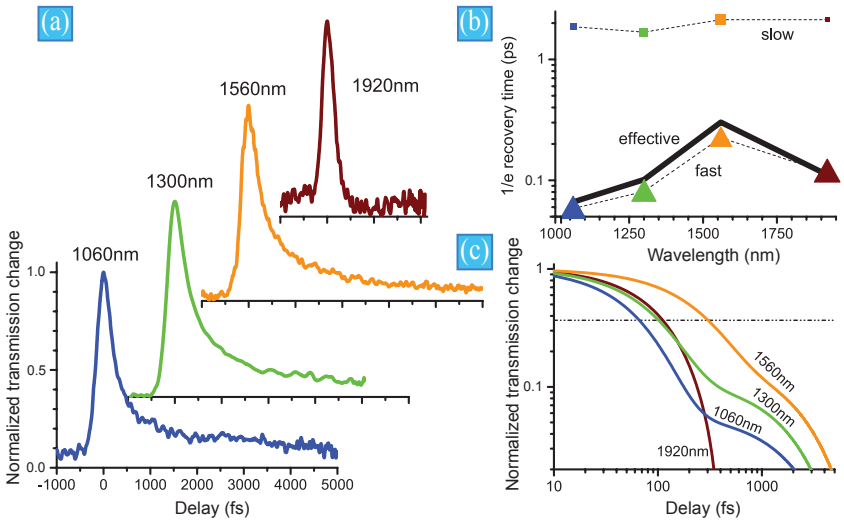

Figure 5.3: *Experimental pump-probe traces of the same SA based on HipCO-made SWCNTs; (a) Pump-probe traces measured at four different wavelengths. (b) The retrieved fast (triangles) and slow (squares) recovery times τ_1 & τ_2 plotted as function of wavelength. The symbol size indicates the relative weight of the fast and slow components. The solid thick black line represents the effective $^1/_e$-relaxation time. (c) The normalized transmission change for all 4 measurements in a double-logarithmic plot. Figure published in [75].*

nanotubes yielding a broadband absorption (section 2.3.4). Applying the convolution method, the fast component τ_1 was found to increase from approximately 70 fs at 1060 nm to 300 fs at 1.55 µm[Figure 5.3 (b)].

The increase of τ_1 in the vicinity of the E_{11} transitions of the largest nanotubes in the mixture may be explained by the increasing number of nanotubes being excited resonantly or close to the band gap. In such excited SWCNTs, relaxation via fast cc-scattering is less efficient and slower relaxation channels (cop-, and cap-scattering, section 3.2) become more important during relaxation. In the curves, the slow relaxation component (described by τ_2) is clearly discernible, giving rise to a small pedestal at positive delays. The latter is not present at 1.9 µm, and the faint fast response visible may be ascribed to the response of metallic nanotubes. This indicates, that a HiPCO nanotube based SA is not useful for mode-locking at Tm-wavelength around 2 µm.

As shown in section 2.3.4, operation at 2 µm demands for arc-made SWCNT-SAs. The biexponential fit to the differential transmission change using equation (5.2), yields time constants of 250 and 1160 fs, using the convolution method, time constants of 230 and approximately 1500 fs were obtained. Hence, both methods result in similar relaxation time constants, if the relaxation time is of the order or

slower than the pump pulse duration. Figure 5.4 shows pump-probe measurements of the three SA types for a pump wavelength of 1960 nm and the fit using the convolution method. The SESAM measurement [(a), squares and blue curve] shows a quasi instantaneous response, followed by a dominant (98 % integral weight) slow relaxation.

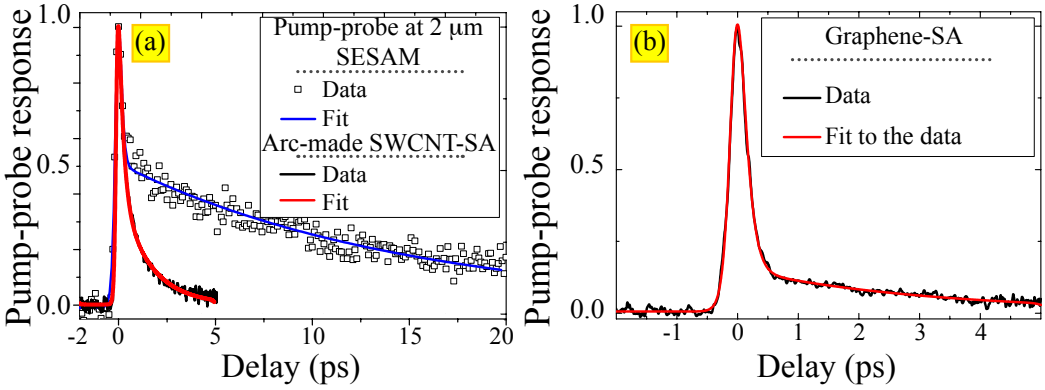

Figure 5.4: *Measured pump-probe response of the three investigated saturable absorbers at 2 µm wavelength: (a) Differential transmission change of the arc-made SWCNT-SA (black solid line) and an 1 quantum well SESAM (squares). The corresponding fits are denoted by the red and blue solid lines, respectively. (b) Differential transmission change of the graphene-SA (black solid line) and the corresponding fit (red solid line). For these three saturable absorbers under study, the convolution method was applied. In case of a SESAM the dominant slow relaxation time is clearly discernible as a slowly decaying pedestal.*

The graphene-SA was measured at 1 and 2 µm. The relaxation times τ_1 and τ_2 are found to be comparable for both wavelengths, but the integral weight of τ_2 seems to be increasing with wavelength. This corroborates that approaching the Dirac point in graphene, the effective relaxation time is increasingly dominated by the slow relaxation processes, confirming similar reports [171].

The pump-probe measurement of graphene at 2 µm reveals time constants τ_1 and τ_2 of 80 and 3500 fs, respectively. The straight forward approach using the biexponential fit yields 170 and 3700 fs, overestimating the fast component by a factor of two, whereas the slow component is not markedly influenced by the different evaluation approach. Similar values of $\tau_1 = 200$ fs and $\tau_2 = 1.5$ ps were found for a graphene-SA at 800 nm using a biexponential fit [44].

The extracted components of the relaxation time are in good agreement with literature [83, 172, 173]. In references [83, 84], a very fast equilibration of the carrier distribution on an ultrashort time scale on the order of 10 fs was reported for graphite and graphene. This relaxation time is much shorter than the pump-probe time resolution and cannot be resolved using the pump-probe lasers available. For

graphene the dependence of the relaxation time on the pump wavelength may be neglected, as a slow down of the relaxation is expected only close to the Dirac point, *i.e.*, at excitation energies below 300 meV [171].

Considering the shape of the measured pump-probe curves, the question arises, whether the sharp peak at zero time delay is caused by an ultrafast relaxation process in the sample, or by an interference between pump and probe pulse (coherence spike). As discussed in section 5.1.1 on page 62, the best possible care was taken to suppress the coherence spike.

All relaxation times obtained with the different SWCNT and graphene-SAs are listed in table 5.1. Furthermore, the results of a SESAM with common parameters is given as well. The last column of table 5.1 lists the integral weight of the slow time constant $w_{\mathrm{int},2}$ (the weight of the fast component is the complement to 100 %). Figure 5.4 shows, that the slow relaxation time is dominant in SESAMs, and on the contrary, plays a minor role for the relaxation of carbon nanostructure-based SAs.

The self-starting behavior of mode locked lasers is ascribed to the slow relaxation of the SA used [174]. For this reason the integral weights of the participating time constants in the relaxation of carbon nanostructure-SAs need to be discussed during their application as mode-locker. SESAMs feature reliable self-starting behavior, but mainly at the expense of a longer effective relaxation time. The latter is mainly determined by the slow relaxation component, which is in general in the order of several picoseconds.

Sample	λ [nm]	τ_1 [fs]	τ_2 [ps]	τ_{eff} [fs]	w_{int} [%]
HipCO SWCNT†	1060	60	1.9	70	72
	1300	80	1.7	100	75
	1560	225	2.1	300	66
Arc-made SWCNT	1920	230	1.52	530	84
Graphene	1060	110	3.0$^{(*)}$	120	36$^{(*)}$
	1980	80	3.5	90	72
SESAM‡ (Batop)	1040	-	-	500-1000	100
	1340	-	-	1000	100
	1510	-	-	10^4	100
SESAM$^{\boxtimes}$	1960	60$^{\circledast}$	15	100	98

Table 5.1: *Results of pump-probe studies. The fast (τ_1) and slow (τ_2) contributions to the effective $1/e$-relaxation time τ_{eff} of different SWCNT-SAs and a graphene sample used in this work. For comparison typical SESAM parameters are included. w_{int} denotes the integral weight of the slow relaxation component explained in the text.* $\diamondsuit$ † *- At 2 µm, only a faint fast response is measured for the HipCO-made sample, which can be seen in figure 5.3(a).* $\diamondsuit$ $^{(*)}$ *- the slow time constant was fit manually, as the automatism underestimates the slow decay.* $\diamondsuit$ ‡ *Information from Batop GmbH. If only one relaxation time is specified, it corresponds to τ_2. In this case $w_{int} = 100\,\%$.* $\diamondsuit$ $^{\boxtimes}$ *A one quantum well SESAM for 2 µm, fabricated at Tampere University of Technology, Optoelectronics Research Centre, Finnland.* $\diamondsuit$ $^{\circledast}$ *Fitting the slowly decaying curve with two time constants, this short value for τ_1 is obtained. As the fast decay actually follows the pump pulse, this value needs to be treated with care.*

5.1.4 Nonlinear transmission measurement - results

Figure 5.5(a) shows a NLT curve plotting the losses of a SWCNT-SA as a function of the incident fluence. The data points of the measurement are fitted (thick red line) using equation (3.2). The small-signal and nonsaturable losses $\Delta T_{\text{lin}} = 1 - T_{\text{lin}}$ and ΔT_{ns} are illustrated by the upper and lower horizontal red line, respectively. The vertical red line is drawn at the saturation fluence F_{sat}, and the modulation depth ΔT_{mod} is indicated by the gray arrow.

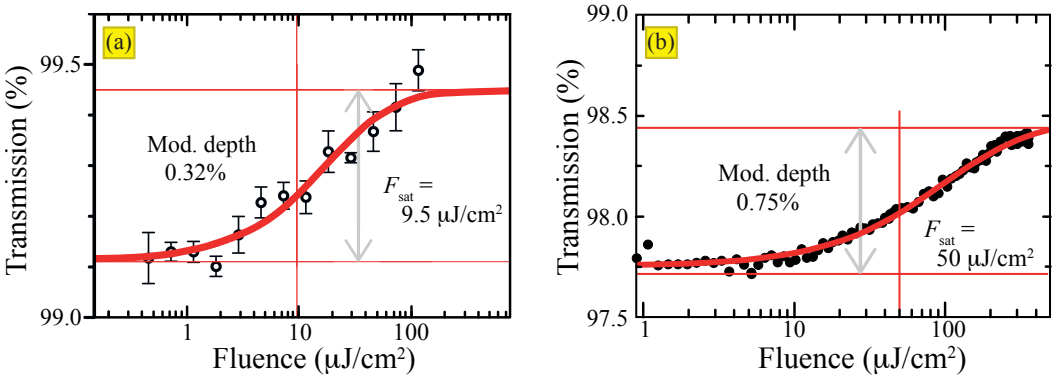

Figure 5.5: *(a) Measured non-linear transmission of a SWCNT-SA at 1.3 µm (open circles) and the corresponding fit (thick red line) as function of the incident fluence. (b) Measured non-linear transmission of the graphene-SA at 1.04 µm (dots), and the corresponding fit (thick red line).*

The saturation fluences of the SWCNT-SA based on HiPCO-made nanotubes is approximately 10 $\frac{\mu J}{cm^2}$. This designed low value is virtually identical with typical values reported for SAs based on arc-made nanotubes used in this work and reported, *e.g.*, in [91, 93, 154], which are of the order of 8-10 $\frac{\mu J}{cm^2}$. Other references report higher saturation fluences $F_{sat} > 50 \frac{\mu J}{cm^2}$ [94, 175]. Higher saturation fluences are unfavorable for avoiding Q-switching instabilities (see section 4.5.1). From the fits to the NLT measurements, nonsaturable losses ΔT_{ns} between 1 and 2.3% and a modulation depth ΔT_{mod} from 0.25 to 0.4% were extracted.

For the graphene-SA the nonlinear transmission measurement was performed at a wavelength near 1.04 µm using a synchronously pumped near-IR tunable femtosecond OPO that delivered sub-200 fs pulses. The maximum pulse fluence on the sample amounted to about 0.4 $^{mJ}/_{cm^2}$. Figure 5.5(b) shows the measured transmission in dependence on the fluence (data points) and the corresponding fit to the data. The fit to the NLT measurement yields a saturation fluence F_{sat} of about 50 $^{\mu J}/_{cm^2}$, and a modulation depth ΔT_{mod} of approximately 0.75%. The nonsaturable loss l_{ns} of the monolayer graphene SA was determined to be 1.59%.

Sample	λ [nm]	ΔT_{mod} [%]	$l_{\text{non-sat}}$ [%]	F_{sat} [$\frac{\mu\text{J}}{\text{cm}^2}$]
HipCO SWCNT	800†	0.15	<1	29
	1300	<0.4	0.95	6
	1560	<0.5	0.95	6
Arc-made SWCNT	1060	0.5	2.3	10
Graphene	800†	1.8	0.9	66
	1040	0.75	1.59	50
	1250*	0.54	1.8	14.5
	1500	0.4	1.9	14
SESAM‡	1040	<1 /<3	<0.5 / ≈ 1	120 / 50
	1340	1.2	0.8	70
	1510	6	<0.5	70
	2000	1.2	0.8	70

Table 5.2: *Results of the nonlinear transmission measurements of SWCNT and graphene-SAs used in this work. SESAM parameters given for comparison. The extracted SA parameters are listed according to absorber type and wavelength.* $\Diamond$ † *and* * *denote data from references [44] and [100], respectively.* $\Diamond$ ‡ *Typical parameters from commercially available SESAMs (Batop GmbH). For SESAMs,* ΔT_{mod} *needs to be replaced by* ΔR_{mod}*. The listed values are from SESAMs yielding the lowest modulation depths. SESAMS with modulation depths of severel ten % are available too, but as they are not relevant for the lasers examined in this work, they are not shown.*

The modulation depth and nonsaturable loss are similar to the values of SWCNT-SAs. The saturation fluence is higher than in SWCNT-SAs, but still those values are well-suited to achieve stable mode-locking of typical bulk lasers. The measured modulation depth was much larger than the values of the single exfoliated graphene layer reported in [84] This is mainly attributed to the high-quality of the CVD-grown monolayer graphene.

Apart from one exception [103], SWCNT- and graphene-SAs have not shown TPA in the NLT measurements with the available pump source fluences. The onset of TPA distinguishes SWCNT- and graphene-SA from classical SESAMs. In the latter, TPA may occur at relative low fluences of 20 to 100 $\frac{\mu\text{J}}{\text{cm}^2}$ [143, 176], limiting

their applicability for higher laser powers. The measured TPA in SWCNTs at wavelengths around 800 nm corroborates that the TPA-coefficient increases with decreasing wavelength and is clearly discernible for the E_{44} transition. Transition changes in the PMMA layer as in [177] are less probable, as the roll-over in the NLT measurement of [103] is reversible.

The measured relevant parameters of the differently produced SWCNT-SAs and the graphene-SA are listed in table 5.2. The results are listed according to the absorber type and the wavelength of the NLT measurement. Typical SESAM values are shown for comparison.

5.2 The laser set-up

Figure 5.6 shows a schematic of the laser cavity set-ups used in this work. According to [178], astigmatism resulting from off-axis resonators is compensated by means of the cavity configuration. The angular tilt of M_1 and M_2 are determined by the crystal thickness, yielding for example a tilt of 6 degree for a 3-mm thick laser active material. The laser cavities used are set-up for polarization parallel to the optical table. If only vertical pump source radiation is provided by the pump laser, a half-wave plate ($\lambda/2$) is used. The prism pair (P_1 and P_2) are applied for dispersion compensation (see section 4.2.2), and all spherical mirrors used (M_n) are dielectric dicroitic mirrors. If the output coupler (OC) limits the cavity without using the prism pair, the laser operates in the picosecond regime.

5.3 Diagnostics applied

For an assessment of the laser parameters, several standard diagnostic methods were applied. The average output power and the optical spectrum are determined by a bolometric power meter and a commercial spectrometer specified for the wavelength range under study, respectively. If the measurement of these two laser parameters demands for special means, the information is given in the according section.

The pulse duration is assessed by means of background-free intensity autocorrelation based on second harmonic generation (SHG). The autocorrelators are either commercial (for 1 µm) or home-made (for 1.5 and 2 µm). The latter allow for an increased scan range necessary for longer pulses ($\gtrapprox 10$ ps), and is very versatile in terms of the underlying conversion process (e.g., SHG or two photon absorption (TPA) directly in the photodiode). Additionally, it facilitates using the lock-in technique, which is a prerequisite to measure small SHG signals with a sufficient signal-to-noise ratio.

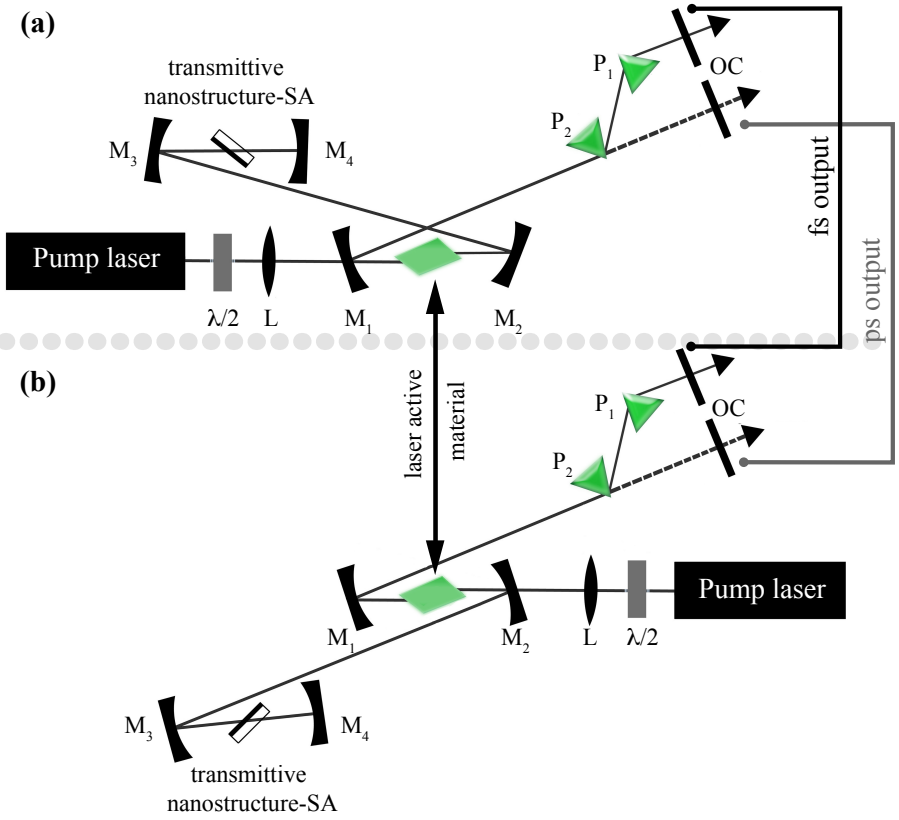

Figure 5.6: *Typical set-up of the mode-locked laser cavities used. The figure shows the* x*-shaped (a) and z-shaped (b) astigmatically compensated cavity according to [178]. The design of (a) is used for the Cr-lasers at 1.25 and 1.5 µm and the Tm-laser around 2 µm. The design of (b) is used for the Yb-laser cavity at 1 µm.* M_n *denote spherical mirrors,* $\lambda/2$ *is an optional half-wave plate for polarization rotation of the pump radiation (e.g., used in the Cr:YAG laser),* L *is the focusing lens for the pump,* P_i *are the prisms and* OC *denotes the output coupler. Operation without prism pair results in picosecond pulses.*

The stability of the pulse train emitted by the lasers is examined recording radio frequency (RF) spectra with a RF-analyzer (Rhode & Schwarz, 7 GHz) and a fast PIN photo diode. Within the RF-spectrum intermode beats are visible at multiples of the repetition rate of the laser (in the order of 100 MHz). Multi-pulsing, i.e., n pulses circulating in the cavity, and Q-switching are easily detectable in the RF-spectrum. For the former the intermode beats are spaced with a period of $1/n$ of the repetition rate, and for the latter, sidebands located some 10 KHz above and below the intermode beats appear.

Some laser pulses were assessed using a home-made interferometric SHG-based frequency resolved optical gating (FROG) measurement according to [179]. After measurement of the interferometric FROG-trace, the data of the fringe resolved measurement is FFT-filtered in order to obtain the DC-part, which is subsequently analyzed by the FROG retrieval program. This assessment results in a retrival of the pulses E-field, optical spectrum, as well as the temporal and spectral phase. By fitting a quadratic function to the spectral phase, the residual 2^{nd}-order dispersion may be extracted. Furthermore, the FROG technique allows for easy consistency checks of the measurements by means of marginals [180]. Here, the frequency marginal, which is simply speaking the SHG-intensity-FROG-trace integrated over time, is the most useful one. The frequency marginals are calculated from the measured and retrieved FROG trace and from the optical spectrum measured at the fundamental wavelength.

5.4 SWCNT mode-locked bulk lasers

SWCNTs have been applied as mode-lockers since 2004 [9] but throughout the first 4 years only fiber lasers were mode-locked using this versatile SA. Fiber lasers tolerate much higher losses due to their gain of up to several ten dB [181] allowing for the compensation of the nonsaturable losses introduced by the nanotube absorbers. Different approaches have been presented for fiber lasers, like coating fiber end faces [182], free-beam optical elements [183] or using the evanescent field in a D-shaped fiber [184]. Bulk lasers, on the other hand, yield a smaller gain compared to fiber lasers and are only reasonably operative if the losses of the laser cavity amount to at most 10%. Fabrication processes have to be adapted to meet the higher requirements for optical quality. Spin-coating of well-stirred polymer-nanotube mixtures allows for a sufficient surface flatness and in turn optical quality. Nanotubes embedded into a polymer layer may be coated onto highly reflecting mirrors or a transmitting glass plates in order to obtain reflective or transmissive SWCNT-SAs.

This section presents the different results obtained with SWCNT-SAs in the wavelength regions under study.

5.4.1 Ytterbium-doped lasers

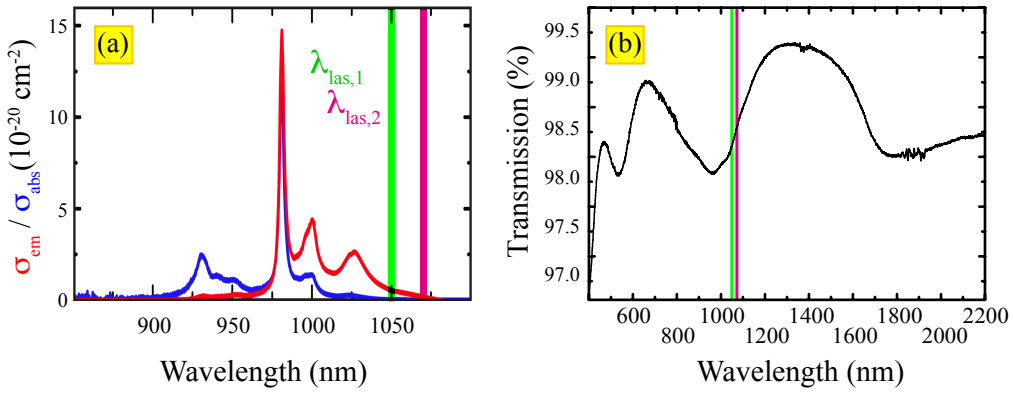

Figure 5.7: *(a) Emission (red) and absorption (blue) cross section of the* ${}^2F_{5/2} \rightarrow {}^2F_{7/2}$*-transition of* Yb^{3+} *in KLuW. The spectral position of the lasers under study (green and magenta line) are plotted with respect to the cross sections and to the measured optical transmission of the arc-made SWCNT-SA (b). Figure (a) from [108].*

In the 1 µm range, a monoclinic Yb:KLuW crystal was used as the laser gain medium. The very same crystal previously showed pulse durations down to 83 fs using a SESAM for passive mode locking at 1049 nm [185]. The SWCNT-SA used for this

laser is based on arc-made SWCNTs. Figure 5.7(a) shows the emission cross section of the $^2F_{5/2} \rightarrow {}^2F_{7/2}$- transition of Yb^{3+} in the KLuW crystal and relates the laser operation wavelength to the emission cross section and the transmission of the arc-made SWCNT [figure 5.7(a) & (b)]. The laser resonator setup applied is depicted in figure 5.6(b).

A continous wave (cw) Ti:sapphire laser was applied as a pump source emitting up to 2 W of output power near 980 nm. For diode-pumping of the Yb:KLuW laser a single-stripe diode laser operating at 980 nm was used. The laser diode output was limited to 2 W due to an inferior lateral beam profile at higher output powers. The crystal was oriented for polarization parallel to the Np optical axis (see section 4.1), and the low quantum defect of the laser active Yb^{3+}-ion allows for operation of the laser using solely passive cooling by the copper holder the crystal was mounted in.

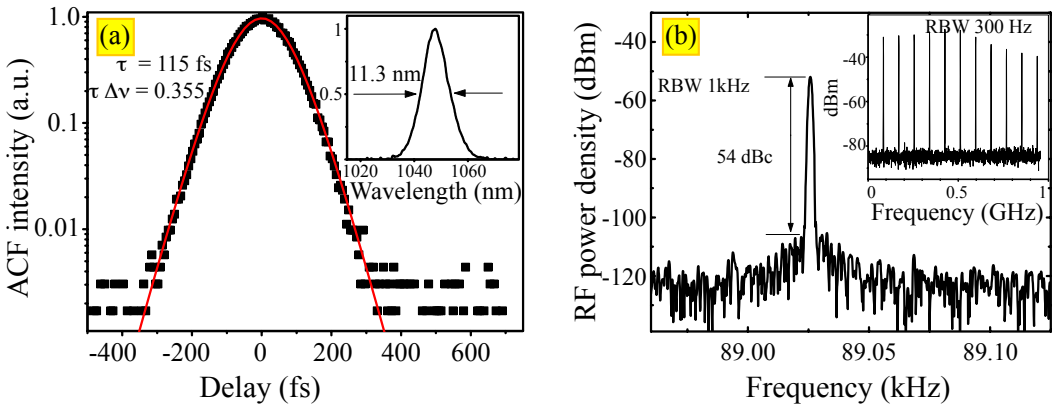

Figure 5.8: *(a) Measured autocorrelation (symbols) and the corresponding sech² fit (red solid line) of the arc-made SWCNT-SA mode-locked Yb:KLuW laser. The inset shows the measured optical spectrum. (b) Measured radio-frequency spectra of the Yb:KLuW laser, showing the fundamental beatnote and a 1 GHz scan (inset). No spurious modulations are visible down to 54 dBc below carrier.*

First, the SWCNT-SA was incorporated into the cavity without using the dispersion compensating prisms. In this configuration picosecond mode-locking was achieved yielding a pulse duration of 9.2 ps at a repetition rate of 88 MHz. The laser was self-starting but tended to Q-switch. The incident pump power of 1.34 W yields an average output power of 53 mW at 1046 nm. In this regime the fluence on the SA amounted to $\approx 5.3 \frac{\mu J}{cm^2}$ which is close to the saturation fluence of the absorber.

As the optical spectrum (not shown here) features steep edges, mode-locking is clearly not solitary and pulse formation is ascribed to the passive amplitude modulation by loss modulation of the SWCNT-SA.

For femtosecond operation utilizing soliton generation (section 4.3.3 on page 50), the different amounts of dispersion, present in the cavity, need to be considered.

The group velocity is explicitly dependent on the refractive index [see equation (4.9)], therefore the material dispersion may be calculated by means of the Sellmeier equations for the individual materials. This is shown for the laser host materials used in this work in figure 4.3(a) on page 45. For the Nm principal optical axis of the KLuW host, a GVD of about 130 fs^2/mm is obtained, yielding a roundtrip GDD due to the host material of approximately 780 fs^2 (3 mm crystal thickness, two passes per roundtrip).

By insertion of two SF10 Brewster prisms with a ttt-separation of 38 cm, stable mode-locked operation was obtained. If the second prism is inserted about 4 mm into the beam (*i.e.* the center wavelength propagates at a distance of approximately 3.7 mm away from the prism apex through the second prism), the calculation according to equation (4.12) yields a negative roundtrip-GDD of approximately -2400 fs^2 [121, 122], which compensates the overall positive GDD introduced by the laser material and SPM. The cavity length is virtually unchanged, resulting in a pulse-repetition rate of 89 MHz. When pumped with the Ti:sapphire laser, the mode-locking threshold using the 1 % output coupler was approximately 270 mW of incident pump power. The intensity autocorrelation trace, the corresponding fit and the spectrum of the shortest pulses are shown in figure 5.8(a). If $sech^2$-shaped pulses are assumed, deconvolving the autocorrelation yields a FWHM pulse duration of 115 fs. The autocorrelation function (ACF) is shown in a semilogarithmic plot for visual assessment of the fit with the data in the wings of the ACF.

The average output power amounted to 30 mW and the corresponding output spectrum was centered at 1048 nm having a bandwidth of 11.3 nm. The time-bandwith product $\Delta\nu \cdot \Delta\tau = 0.355$ corresponds to nearly transform limited $sech^2$-shaped pulses. These pulses durations are shorter than those mentioned in the only previous reference on SWCNT-SA mode-locked bulk lasers near 1 µm at the time of the experiments. Schibli et al. reported a pulse duration of ≈200 fs for a Nd:glass laser without further characterization [142]. In figure 5.8(b) the RF spectrum of the arc-made SWCNT-SA mode-locked Yb:KLuW laser is shown. The 1 GHz span (inset) and the first beat note, recorded at 1 kHz resolution bandwidth, do not show spurious modulations down to 54 dBc relative to the carrier. This is a clear evidence of stable cw mode locking.

Using the prism pair, the laser operates in the soliton-like mode locking regime, whereas this assumption is supported by the optical spectrum and autocorrelation trace, being well fitted using a $sech^2$ intensity profile and an autocorrelation of a $sech^2$ pulse shape, respectively. The fit nicely reproduces the measurement down to a relative ACF intensity of $5 \cdot 10^{-3}$. Furthermore, the TBP close to the Fourier limit for $sech^2$ shaped pulses, confirms the assumption of this pulse shape. A more detailed analysis applying the soliton condition (equation (4.23) of section 4.3.3) is presented in section 5.6.2.

Diode pumping using the same pump-, and cavity configuration with the SF10 prisms yields stable femtosecond mode locking as well. An incident pump power of 1.5 W yields a maximum mode-locked output power of 16 mW. Imperfect matching between pump and resonator modes and the lower beam quality of the diode emission causes a lower efficiency compared to the experiments with Ti:sapphire laser pumping.

Further laser parameters are the repetition rate $f_{\mathrm{rep}} = 89\,\mathrm{MHz}$, pulse duration $\tau_{\mathrm{FWHM}} = 170\,\mathrm{fs}$, center wavelength $\lambda_{\mathrm{c}} = 1045\,\mathrm{nm}$, spectral bandwidth $\Delta\lambda_{\mathrm{FWHM}} = 7.2\,\mathrm{nm}$, and a time-bandwidth product $\Delta\nu\Delta\tau = 0.334$, hence, also the diode-pumped mode-locked Yb:KLuW laser delivers almost transform limited pulses. The radio-frequency spectrum indicates a 61 dBc extinction ratio of the fundamental beat note at 88.85 MHz, as measured with 3 kHz resolution bandwidth. Single-pulse operation is confirmed by the wide-span measurements up to 1 GHz.

SWCNT-SA type	Center Wavelength in nm	Pulse duration in fs	Average output power in mW	Output coupling in %	Repetition rate in MHz	Pump scheme	Fluence on the absorber in $\mu J/cm^2$	Reference	This work
transmittive	1048	115	30	1	89	Ti:sa	55	[91]	☒
	1045	170	16	1	89	LD	30		
reflective	1049	83	24	1	84	Ti:Sa	100	[143]	☒

Table 5.3: *Laser parameters of the arc-made SWCNT-SA mode-locked Yb:KLuW lasers examined in this work. LD and Ti:sa denote pumping using a laser diode or Ti:sapphire laser, respectively.*

Assessment of the mode-locking stability

Modeling the laser cavity yields two distinct stability regions depending on the distance between M_1 and M_2. If this distance is 105 mm, the beam waist radius between M_3 and M_4 is calculated to be in the order of 90 µm, whereas a smaller distance M_1 - M_2 of approximately 100 mm yields a smaller beam waist radius at the absorber position of 30 µm. The latter stability region is more sensitve in terms of misalignment of the cavity, and as in this work the distance M_1 - M_2 was set to values larger

than 105 mm, operation in the according stability range, and a beam waist radius of 90 µm between M_3 and M_4 are assumed. Furthermore the Brewster angle of the transmittive SWCNT-SA is taken into consideration to calculate the fluence given in table 5.4.1. Considering the SWCNT-SA saturation fluence of approximately $10\,\frac{\mu J}{cm^2}$ (table 5.2), the SAs operate at saturation parameters around 5 or 10 for the transmittive and reflective samples, respectively. Those values are not critical with respect to pulse-breakup (section 4.5.2).

In order to estimate the stability of the laser against Q-switching instabilities, the criterion of section 4.5.1 is applied. The saturation fluence of the laser gain $F_{\mathrm{sat,L}}$ is assessed according to [88] by

$$F_{\mathrm{sat,\ L}} = \frac{h\nu_{\mathrm{las}}}{\sigma_{\mathrm{L}}} \ . \tag{5.4}$$

Here σ_{L} denotes the emission cross section of the laser transition with frequency ν_{las}. In four-level laser media $\sigma_{\mathrm{L}} = \sigma_{\mathrm{em}}$, whereas in a quasi three-level system (see section 4.1.1) the laser saturation fluence is given by [186]

$$F_{\mathrm{sat,\ L}} = \frac{h\nu_{\mathrm{las}}}{\sigma_{\mathrm{em}}(F(\lambda_{\mathrm{las}},\, T)+1)} \ . \tag{5.5}$$

$F(\lambda_{\mathrm{las}},\, T)$ is a function proportional to the ratio of the Boltzmann population distributions of the Stark manifolds involved in the laser transition and for Yb^{3+} it may be approximated to be in the order of 1.15 at 300 K [187].

The black solid line in figure 5.9 shows the critical pulse energy $E_{\mathrm{P,\ crit}}$ as a function of the QML parameter β_{QML} according to equation (4.26). The figure also plots the calculated laser pulse energies of the results obtained with the Yb:KLuW and the Yb:KYW lasers under Ti:sapphire laser pumping, and the Yb:KLuW laser using laser diode pumping, respectively. The corresponding QML parameter β_{QML} for the individual laser active materials in the given resonator geometry is assessed using equation (5.5).

In case of multiple results for one combination of laser gain medium and cavity configuration, the result with the smallest pulse energy is plotted. For all Yb-doped SWCNTS-SA mode-locked lasers, operation are expected to be stable against QML instabilities even if the *simple* QML criterion is taken into account[*cp.* equations (4.26) and (4.28)].

Damage

During alignment of the SWCNT-SA mode-locked Yb:KLuW laser, fluctuations similar to Q-switching were observed. In the optical spectrum a large number of

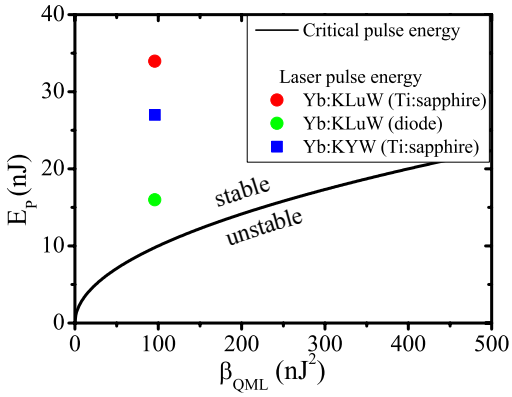

Figure 5.9: *Calculated stability of the Yb-doped lasers against Q-switching. The solid black line denotes the stability criterion according to [88]. The data points represent the calculated pulse energies for the Yb:KLuW and Yb:KYW lasers vs. QML-parameter. Results for different pumping schemes are shown. Using a typical SESAM with the same cavity and crystal parameters,* $F_{sat} = 50\,\frac{\mu J}{cm^2}$*, and a* $\Delta R = 1\,\%$*,* β_{QML} *increases by a factor of about 40,* $E_{P,\,crit}$ *by a factor of* $\sqrt{40} \approx 6$*. Hence, the results shown would suffer Q-switching instabilities using a SESAM, whereas they are in the stable cw-mode-locking region for the SWCNT-SA used.*

(>20) cw components fluctuated at different optical frequencies, covering a spectral region less than a few nm. Laser optimization in this operation regime is delicate, as damage may occur to the SWCNT-SA, which is indicated by sparks on the absorber. The damage, however, is expected to occur in th polymer substrate and not in the SWCNTs.

5.4.2 Chromium-doped lasers

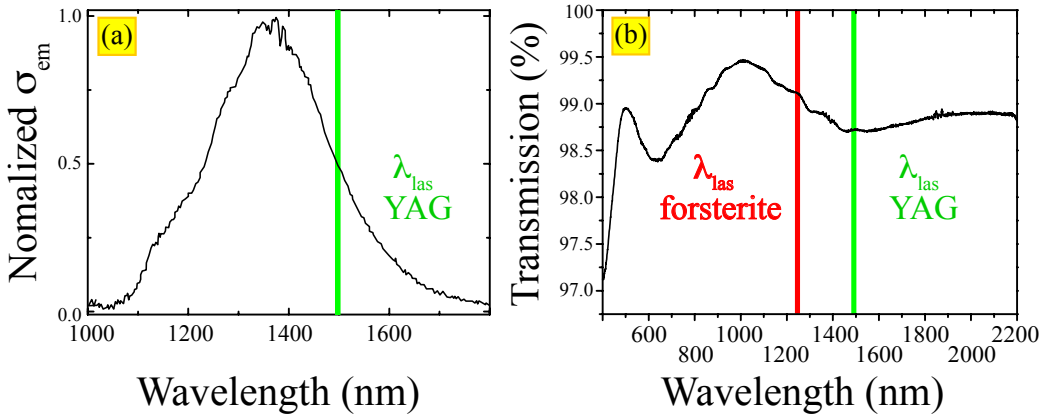

Figure 5.10: *(a) Emission cross section of the* $^3B_2 \rightarrow {}^3B_1$ *transition of* Cr^{4+} *in YAG. (b) The measured HipCO-made SWCNT-SA transmission. The green vertical line denotes the spectral position of the Cr:YAG laser under study and the red line in marks the emission of the HipCO-made SWCNT-SA mode-locked Cr:forsterite laser of reference [150], operated at the Ajou University in Suwon, South Korea. Data in figure (a) is reproduced from[188].*

The Cr^{3+}-doped yttrium aluminium garnet (YAG) laser emits around 1.5 µm, demanding for SWCNT-SAs based on HiPCO-made nanotubes that exhibit an absorption in this wavelength region (see section 2.3.4).

A 10 W cw Nd:YVO_4 laser (Spectra-Physics) operating at 1.064 µm is used as pump source. The Cr:YAG crystal is Brewster-cut and has a length of 20 mm. A flat, wedged output coupler with a 2% transmission at the lasing wavelength was used in a cavity setup depicted in figure 5.6(a). Because of a series of water absorption lines between 1.36 and 1.5 µm negatively effecting the laser stability [189], the whole oscillator was enclosed in a box and purged with dry nitrogen for stable pulsed femtosecond operation. Without dispersion compensating prisms, the passively mode-locked self-starting Cr:YAG laser produced stable picosecond pulses of 4.4 ps duration. Other laser parameters are a spectral bandwidth of 1.4 nm, a central wavelength of 1505 nm, a repetition rate of 87.9 MHz, and a TBP of 0.823. The latter indicates that pulse formation is not due to the formation of solitons, but rather due to self-amplitude modulation caused by gain and loss filtering. In this ps-setup a tuning range larger than 70 nm between 1435 and 1505 nm was realized but at wavelengths below 1450 nm a decrease of the laser spectral width was observed, which is attributed to the increasing residual water absorption and the short-wave limit of the dielectric mirrors used.

In reference [190] the round-trip GDD of the 20-mm-long Cr:YAG rod at 1.5 µm is measured to be $+450\,\mathrm{fs}^2$ which is on the same order of magnitude as the calculation

using equations (4.8) - (4.10), giving approximately +530 fs^2. The calculated round-trip refractive GDD of the prism pair according to equations (4.12) and (4.13) is approximately - 1,300 fs^2. Here the center wavelength of 1.5 µm passes second prism in a distance of approximately 2 mm from its apex, corresponding to a horizon wavelength of 1000 nm [122]. The latter corresponds to the short-wavelength end of the Cr^{3+}-emission shown in figure 5.10(a).

Tuning of the center wavelength is possible by adjusting the second prism in combination with a knife edge and the mode-locked tuning range extends from about 1.46 to 1.50 µm [figure 5.11(a)].

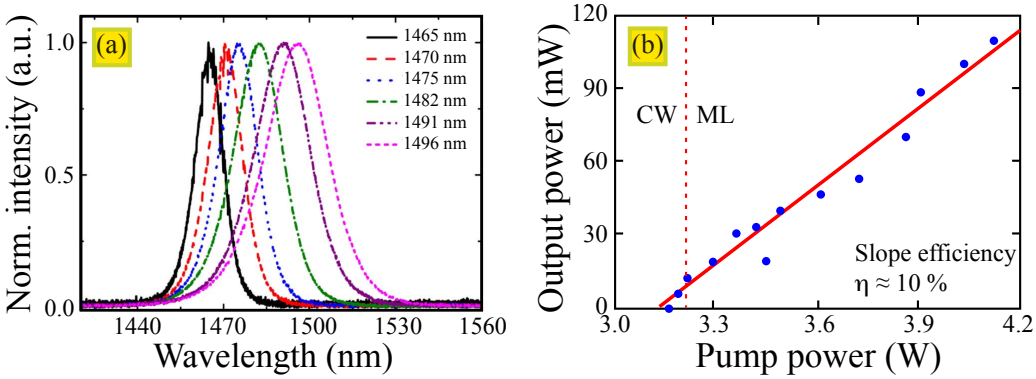

Figure 5.11: *(a) Measured tunability of the HipCO-made SWCNT-SA mode-locked Cr:YAG laser over 40 nm aligning a prism and a knife edge. The spectral width decreases for shorter central wavelengths. (b) Average output power of the HipCO-made SWCNT-SA mode-locked Cr:YAG laser. The vertical line indicates the transition from the continuous-wave (CW) to the mode-locked (ML) regime.*

Shorter central wavelengths result in narrower optical spectra, and mode-locked operation becomes less stable. A longer N_2 purging time stabilized mode locking in the entire tuning range. Figure 5.11(b) shows the average output power versus the input pump power measured for femtosecond operation at 1.5 µm, yielding a slope efficiency of ≈10%. From slightly above threshold (P_{pump} = 3.2 W) up to the maximum average output power of 110 mW (P_{pump} = 4.26 W), stable self-starting mode-locked operation was achieved. This range corresponds to an incident pump fluence on the SWCNT-SA of 0.05 – 0.33 $\frac{mJ}{cm^2}$, sufficient for bleaching the absorption. A higher pump power may be applied, but it results in strong spectral modulations and pulse breakup into multiple pulses (see section 4.5.2). The intensity autocorrelation function is fitted assuming a sech^2 pulse shape [equation (4.22)] and the shortest laser pulses yield a pulse duration of 92 fs. The plot is given on a semi-logarithmic scale to show, that the fit nicely matches the data down to a relatvie ACF intensity of about $2 \cdot 10^{-3}$. The time-bandwidth product of 0.33 is calculated from this pulse

duration and the measured FWHM spectral bandwidth of 27 nm, which is centered at 1495 nm. The autocorrelation and optical spectrum are shown in figure 5.12(a). Compared to the laser output without the dispersion compensating prism pair, the optical spectrum shows a smooth progression with a sech^2 profile, instead of a steep optical spectrum. Furthermore, the TBP is close to the transform-limited value of 0.315, presenting another indication for the presence of solitary mode-locking. In section 5.6.2, the soliton condition is used for assessment of the solitary character of mode-locking in Cr:YAG.

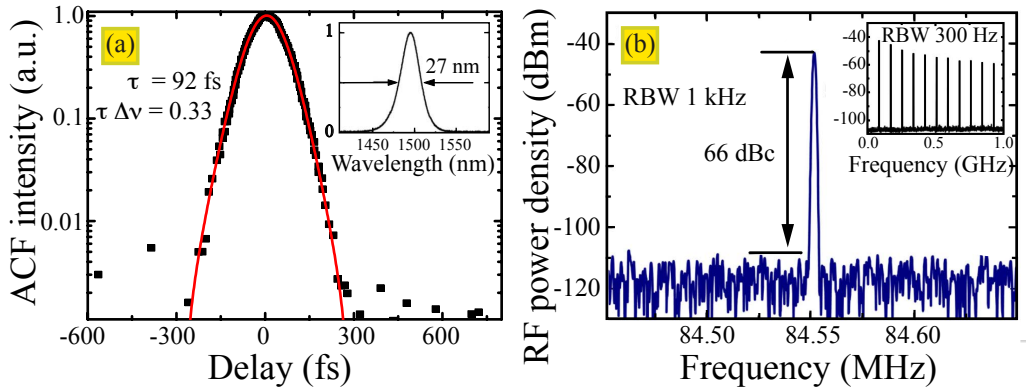

Figure 5.12: *(a) Measured autocorrelation (symbols) and sech^2 fit to the data of the HipCO-made SWCNT-SA mode-locked Cr:YAG laser. The inset shows the corresponding optical spectrum. (b) Measured radio-frequency spectra of the HipCO-made SWCNT-SA mode-locked Cr:YAG laser showing the fundamental beat-note at the pulse repetition frequency $f_{rep} = 84.55$ MHz and a 1 GHz scan (inset).*

Figure 5.12(b) shows the recorded radio frequency spectra of the laser. The high resolution RF-spectrum shows a sharp peak at the fundamental beat note of 84.55 MHz, as well as a high extinction ratio of 66 dBc from the noise level. The high harmonics of the fundamental beat note are shown in the inset. The measured RF spectra indicate stable single-pulse mode-locked operation without any signs of Q-switching instabilities and multiple pulsing.

In further experiments, applying improved HipCO-made SWCNT-SAs, significantly shorter pulses of 50 fs duration with an increased spectral bandwidth of more than 50 nm were obtained. For characterization of those pulses the FROG technique described in section 5.3 was performed. Figure 5.13(a) shows the measured FROG trace (a) next to the retrieved FROG-trace in figure 5.13(b). The measured trace shows a small asymmetry ascribed to fluctuations in the laser output during the measurement, spectral dependencies of phase matching or the applied spectrometers. From the FROG-retrieval a pulse duration of 48 fs [see figure 5.14(a)] was obtained. This pulse duration is in good agreement to noncollinear SHG autocorrelation measurements (Femtocrome autocorrelator FR-103XL). The spectral

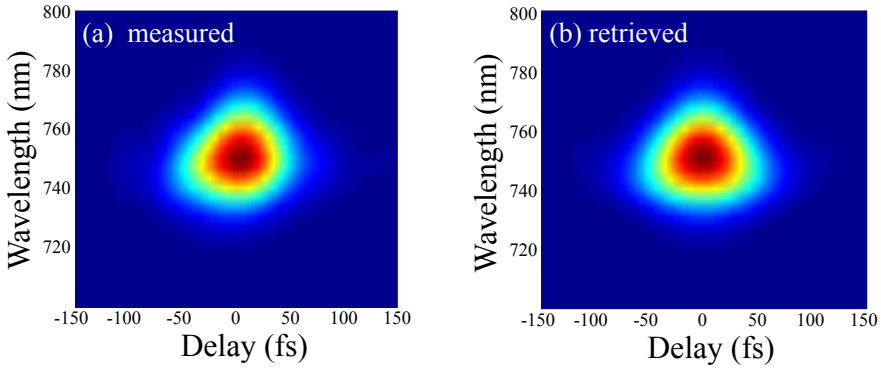

Figure 5.13: *(a) Measured and (b) retrieved FROG-trace of the HipCO-made SWCNT-SA mode-locked Cr:YAG laser.*

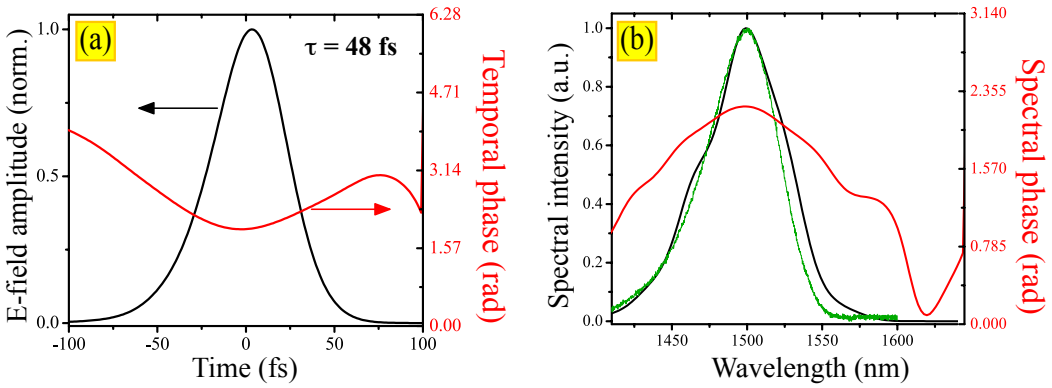

Figure 5.14: *FROG measurement of the HipCO-made SWCNT-SA mode-locked Cr:YAG laser. (a) The retrieved electric field envelope (black) and the according temporal phase (red). (b) The measured (green) and retrieved (black) optical spectrum, as well as the spectral phase (red).*

bandwidth resulting from the FROG-retrieval is 65 nm, but shows small fluctuations in the wings of the spectrum. The measured and retrieved optical spectra are shown in figure 5.14(b) with the spectral phase being plotted in the same figure. The FROG-error on a 1024 x 1024 grid size is 0.02.

One drawback of the SHG FROG measurement is the fact that the sign of the second order dispersion represents an ambiguity [191]. That is to say the absolute value of the GDD from the fit may be retrieved correctly, but the sign has to be checked separately. This stems from the fact that the time reversed E-field $E(-t)$ generates exactly the same FROG trace like the E-field $E(t)$. Within the FROG-retrieval of such a FROG-trace *one* of the solutions is retrieved, depending on the initial guess.

As proposed in [191], the check for the correctness of the sign may be done, *e.g.* by introducing a small pre-pulse to the main pulse by inserting a thin glass plate. Another approach is the insertion of an additional material of defined thickness and known dispersion followed by a comparison of the dispersion extracted from the measurement with and without the material. If the evolution of the value of the dispersion behaves like expected, the retrieved sign of the GDD is correct. Otherwise the E-field has to be temporally reversed and the dispersion curves mirrored at the wavelength axis.

The retrieved spectral phase was used for determination of the GDD. The spectral phase is plotted versus frequency and fitted by a polynomial of second order. The coefficient of the fitting functions quadratic term corresponds to the second order dispersion. Doing so with the above shown data a residual second order dispersion of $D_2 = -285\,\mathrm{fs}^2$ is obtained.

For testing the sign of the extracted GDD in the Cr:YAG laser, one FROG measurement is performed without additional material and a second measurement with a 3 mm thick ZnSe plate, introducing a GVD of $+400\,\frac{\mathrm{fs}^2}{mm}$, i.e., an overall additional GDD of $\approx$1200 fs^2. From the first measurement without additional material an average GDD of $|D_2| = 584\,\mathrm{fs}^2$ is extracted. This value differs from the GDD extracted from the first FROG measurement by $\approx 300\,\mathrm{fs}^2$ because of necessary re-alignment of the laser cavity. The obtained values are listed in table 5.4, and in conclusion, the extracted net negative dispersion confirms former reports for this type of laser [192, 193].

	GDD in fs^2
Measured w.o. material	$\approx +600$
Possible values	+600 | -600
3 mm ZnSe plate	+1200
Possible overall value	+1800 | +600
Measured with ZnSe plate	+890
Assumption correct?	× | ✓

Table 5.4: *Assessment of the sign of GVD. The laser output is evaluated without (w.o.) additional material and with a 3 mm ZnSe plate. The sign of GVD was found to be negative.*

It is to note that purging was not essential in this operation mode, neither with the HipCO-made SWCNT-SA, nor using the graphene-SA in this configuration (see section 5.5.2 on page 105). Mode-locking becomes unstable for a laser tuned below

Active laser material	Center wavelength in nm	Pulse duration in fs	Average output power in mW	Repetition rate in MHz	Output coupling in%	Spot size radius on SA in µm	Max. fluence on SA in $\frac{\mu J}{cm^2}$	Necessary® SA replacement in mm	Reference	This work
Cr:forsterite	1245	120	202	79	5	40	430	10	[150]	
Cr:YAG	1495	92	110	85	2	80	135	14	[153]	☒
	1500	48	67	85	2	80	80	7	-	

Table 5.5: *Results using HipCO-made SWCNT-SAs to mode-lock chromium-doped lasers. Note that the forsterite laser of reference [150] is listed for comparison and was operated at Ajou University Suwon, South-Korea.* ® *replacement necessary to obtain a saturation parameter of S=10, assuming Gaussian beam propagation and a minimum beam waist radius of 90 µm.*

1.5 µm, which is ascribed to the increasing water vapor absorption with decreasing wavelength [194]. A similar report shows a mode-locked Cr:YAG laser with a central wavelength down to but not below 1488 nm [195]. The set-up used in the present work required purging to operate at central wavelengths at and below 1496 nm, whereas the laser with the non-purged cavity operates at a central wavelength of ≈1515 nm. In the latter case the spectral tuning is performed by means of the output coupler alignment and by introducing a knife edge in between the dispersion compensating prisms.

In case of the purged cavity, the onset of transmission of the cavity mirrors limit the tunability. This short-wavelength limit of stable mode-locking in the cavity under study can be clearly seen in the tuning experiment in figure 5.11(a) where the optical spectrum seems to be 'pressed' against a lower wavelength limit. As confirmed by section 5.5.2, the short wavelength pedestal of the optical spectra does not extend significantly to wavelengths below 1450 nm. The Cr:YAG laser active material, however, would support much shorter wavelengths down to 1340 nm [196][1].

Except the suppression of water vapor influence, there is virtually no difference between the cavity in air or purged with nitrogen. The optical cavity length change is insignificant (as the change in refractive index is $\Delta n \approx 2 \cdot 10^{-5}$) and the material dispersion in both gases is practically the same.

[1] The emission cross section extends to approximately 1 µm [188]

The stability of the operating lasers is assesses according to section 4.5.1 (details on the procedure are given in the previous section on page 79). Figure 5.15 shows the pulse energies obtained with the chromium doped lasers(triangles), the QML criterion (solid line) according to equation (4.26) and the pulse energies obtained with the Yb-lasers for comparison. From the results listed in table 5.5, the lowest pulse energy is plotted or each laser configuration. Lasers with higher pulse energy are expected to be more stable against QML instabilities. It is to be noted that the Cr:forsterite laser was operated at the Ajou University in Suwon, South Korea.

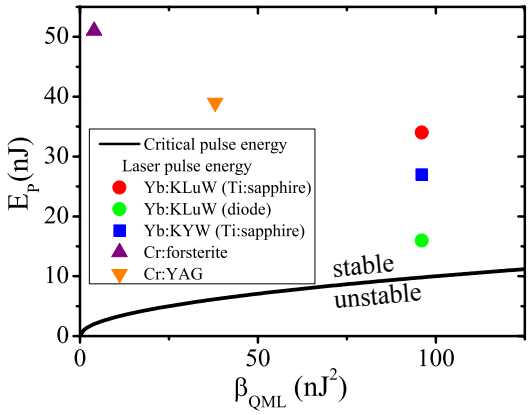

Figure 5.15: *Stability of the HipCO-made SWCNT-SA mode-locked chromium-doped lasers against Q-switching. The solid black line denotes the stability criterion according to reference [88]. The data points represent the calculated pulse energies for the Cr:forsterite and Cr:YAG lasers (triangles) and the Yb-lasers (circles, square) for comparison.*

5.4.3 Thulium-doped lasers

The Tm:KLuW laser

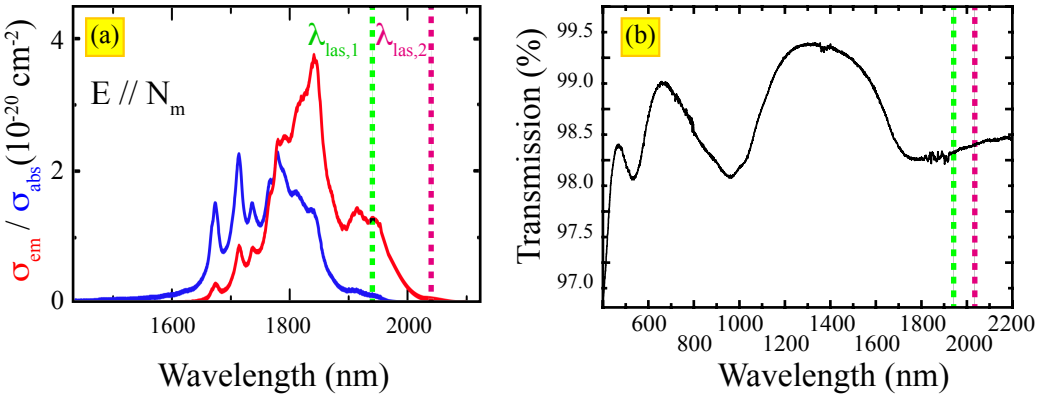

Figure 5.16: *Absorption (blue) and emission (red) cross section of the* $^3F_4 \rightarrow {}^3H_6$*-transition of* Tm^{3+} *in KLuW for polarization parallel to* N_m *(a), and the arc-made SWCNT transmission (b). The spectral position of the center emission wavelengths of the lasers under study (green and magenta lines) are indicated in both plots. The former marks the wavelength of the laser before replacing the cavity mirrors by high-pass dielectric mirrors, the latter after the replacement. The high-pass mirror set shifts the emission wavelength above 2 µm, which is preferable for femtosecond mode-locked operation. Figure (a) taken from reference [108].*

In the 2 µm range, the Tm-doped KLuW host was under study. The corresponding absorption and emission cross section of the $^3F_4 \rightarrow {}^3H_6$- transition of Tm^{3+} in KLuW is shown in figure 5.16(a). Using cavity mirrors specified for a wavelength range between 1.9 and 2.05 µm, the laser operates at a center wavelength around 1.95 µm, denoted by the green line in the figure. To achieve an emission at longer wavelengths, low-pass mirrors have to be applied for the resonator to spectrally shift the emission above 2 µm, which is indicated by the magenta line. the low-pass mirrors yield an increasing transmission for decreasing wavelengths (8 and 84 % at 2 and 1.96 µm, respectively).

The Tm-doping level of the KLuW crystal is 3 at.%, it has a thickness of 2.92 mm and an aperture of 3 x 3 mm^2. The laser crystal was positioned for polarization of the laser parallel to the Nm principal optical axis, *i.e.* propagation along the Ng axis.

At wavelengths around 2 µm, arc-made SWCNT-SAs need to be applied in the Tm:KLuW cavity (see section 2.3.4). Incorporating the transmission type of this SA,

either Q-switching or stable mode-locking without any Q-switching was achieved. By means of changing the effective beam waist (and hence the fluence) on the SWCNT-SA, it is possible to switch between the different modes of operation.

In the Q-switched regime, the laser operates at a repetition rate of $\approx 33\,\mathrm{kHz}$, and an average output power of 170 mW was obtained.

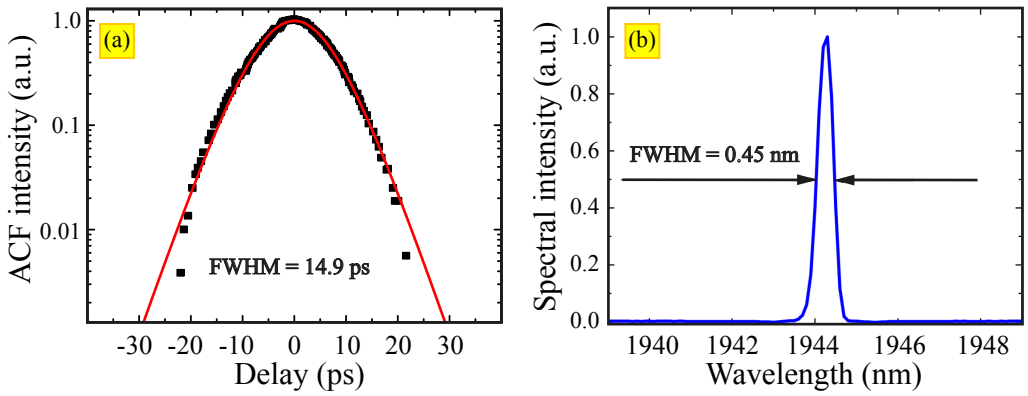

Figure 5.17: *Measured autocorrelation (symbols) and sech^2 fit to the data of the arc-made SWCNT-SA mode-locked Tm:KLuW laser (a). The corresponding optical spectrum (b) is measured with 0.2 nm resolution.*

In the mode-locked regime, 9.7 ps pulses were measured with the self-made intensity autocorrelator (section 5.3). The corresponding output spectrum was centered at 1944 nm and features a FWHM bandwidth of 0.45 nm (measured at a spectral resolution of 0.2 nm using a 0.5 m monochromator). The calculated time-bandwidth product is 0.347, which is close to the Fourier limit for a sech^2-shaped pulse, and the output power amounted to 240 mW at a pump level of 1.86 W. Figure 5.17 shows the autocorrelation and the optical spectrum of this first demonstration of a SWCNT-SA mode-locked bulk laser at 2 µm at the time of the experiment. The semi-logarithmic plot reveals, that for relative ACF intensities down to 10^{-3}, the ACF fit function well describes the data and overestimates them for smaller intensities. However, due to the long pulse duration, only few data points are available in the wings of the autocorrelation, rendering this estimation difficult. Compared to the 'quality' of the fit of the Yb:KLuW and Cr:YAG lasers, the discrepancy between fit and data starts being visible at higher relative ACF intensity values. This fact is reflected in the larger TBP for the Tm:KLuW laser as well. An analysis of the soliton condition is given in section 5.6.2. The RF spectrum of the arc-made SWCNT-SA mode-locked Tm:KLuW laser (shown in figure 5.18) yields the carrier being $> 60\,\mathrm{dB}$ above noise level and the wide-span measurement (inset) does not show spurious modulations, which indicates stable cw single-pulse operation without Q-switching.

To assess the stability of the mode-locked operation against Q-switching, the

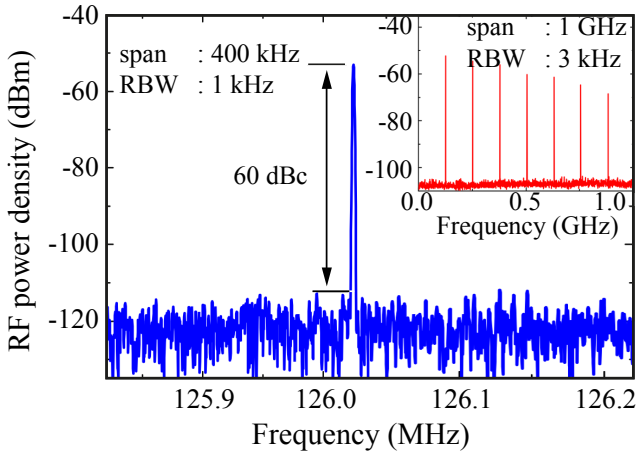

Figure 5.18: *Measured RF spectra of the arc-made SWCNT-SA mode-locked Tm:KLuW laser. The fundamental beat note at the laser repetition rate is 60 dBc above the noise floor and no spurious modulations are visible. The inset shows the wide span RF up to 1 GHz.*

saturation fluence of $\approx 10\,\frac{\mu J}{cm^2}$ at 2 µm, a modulation depth of the SWCNT-SA of ≈ 0.5 % and a calculated waist size on the absorber of 30 µm are assumed. Considering the emission cross section [108], the influence of the three-level nature of Tm [186] and common ratios of the partition functions for Tm in the order of 1.5 [197], a QML parameter of approximately 70 nJ[2], and subsequently $E_{P,\,crit} \approx 8$ nJ are obtained. The Tm:KLuW laser reaches this critical pulse energy if the average output power surpasses approximately 15 mW. With this value slightly above the lasing threshold, the laser is practically unconditionally stable against Q-switched mode-locking, confirming the estimation of [154]. The stability of the Tm laser against Q-switching is re-discussed within figure 5.23 at the end of this section.

For laser operation in the wavelengthrange around 2 µm the center wavelength plays an important role for the generation of ultrashort pulses. So far, all femtosecond mode-locked solid-state lasers did not operate substantially below 1980 nm [198]. In the first place, water vapor absorption (similar to the obstacles present in the Cr:YAG laser in section 5.4.2) is assumed to be the main cause preventing broadband mode-locking with femtosecond pulse durations. However, purging the whole cavity with dry nitrogen to minimize the influence from water vapor was not helpful to broaden the optical spectrum and shorten the pulses. Another explanation may be absorbed or adsorbed water influencing the laser if present in condensed form in or on the absorber. The concentration of absorbed water may be in the order of 0.3 % - 0.4 % of the PMMA weight [199], whereas for the latter no exact values are known. However, no systematic study proofs this suggestion, and so far, the question why mode-locking below 1980 nm is not possible remains a puzzle. One possibility to overcome this limitation is to shift the operating wavelength to longer

values by means of wavelength-selective cavity mirrors.

Therefore, the dielectric mirrors operating in the 1.9 - 2.05 µm range were replaced by specially designed short-pass mirrors. Those mirrors yield a transmission of $T \approx 8\,\%$ at 2000 nm, rapidly increasing for shorter wavelengths. The mirrors are highly reflective at wavelengths $\geq 2.05\,\mu m$ and hence the lasing wavelength is expected to shift towards longer values.

The Tm-doped KLuW crystal features a broad emission cross section extending up to $\approx 2050\,nm$ (see, e.g., figure 4.2(a) or reference [200]), potentially allowing lasing above 2 µm. After mirror replacement, the emission wavelength shifted to 2034 nm, but mode-locked laser operation required incorporation of a pair of Brewster-cut CaF_2 prisms. The prisms were separated by 34 cm, introducing a negative GDD of approximately -1100 fs^2 per round-trip. When the laser started mode-locking, the pulses emitted were substantially shorter than in the first experiments, yielding an accordingly increased spectral bandwidth. As the material dispersion of KLuW at this wavelength is -270 $\frac{fs^2}{mm}$, fine tuning by means of prism material dispersion is limited to an unidirectional change towards lower values of the GDD.

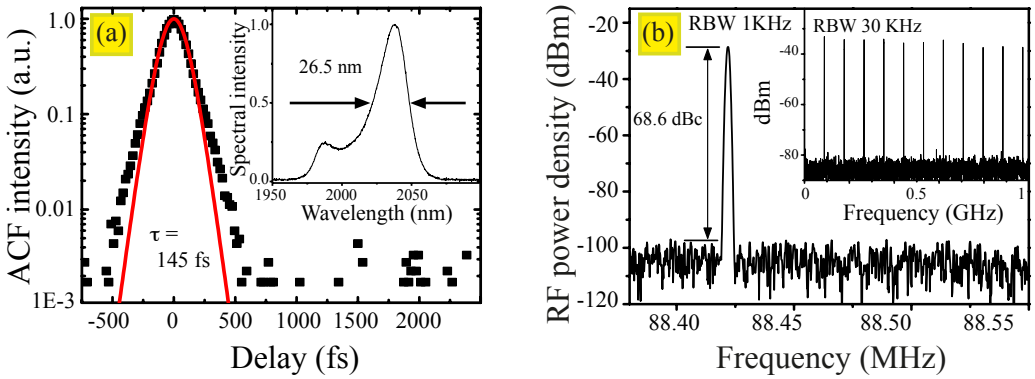

Figure 5.19: *(a) Measured intensity autocorrelation of the arc-made SWCNT-SA mode-locked Tm:KLuW laser (symbols) and the sech² fit (red). The laser operates at a center wavelength larger than 2 µm, and the corresponding optical spectrum is shown in the inset. The pulse shape is not a sech². (b) Measured radio-frequency spectra of the Tm:KLuW laser showing the fundamental beat-note and a 1 GHz scan (inset).*

For the Tm:KLuW laser, the stability of the laser output and the single-mode operation were verified using RF-spectra as well. The spectra recorded with a resolution bandwidth of 1 kHz and 3 kHz are shown in figure 5.19(b). The fundamental beat-note exhibits an excellent signal to noise ratio of the carrier being 68 dB above the noise floor. Furthermore no sidebands or spurious modulations are detected, indicating cw-mode-locked single-pulse operation.

The pulse duration was measured with the background-free noncollinear autocorrelator, and a $sech^2$-fit resulted in a pulse duration of 145 fs with an unsatisfactory match of the fit to the data [see figure 5.19(a)]. The optical spectrum [inset of figure 5.19(a)] shows a clear double hump structure which is not expected for a $sech^2$ beam shape. The spectrum encompasses 100 nm (foot to foot) but the FWHM extracted from the optical spectrum is only 26.5 nm. Using this bandwidth, a TBP of 0.272 is obtained. As discernible from figure 5.19(a), assuming a $sech^2$ pulse shape, the pedestals of the intensity autocorrelation are not fitted correctly. Furthermore, the TBP proves, that pulse formation is not solitary in this case. The shape of the optical spectrum and the TBP indicate the presence of asymmetric pulse shapes, which yield TBPs down to 0.22 [137].

If the intensity autocorrelation is used for pulse retrieval, ambiguities in the direction of the pulse and in the sign of GVD are present and may even result in a failing pulse retrieval [201]. As discussed in [201], and improved in [202], a cross correlation is necessary for ambiguity-free pulse retrieval. This may be realized by placing a dispersive element - introducing a known dispersion to the pulse - in one arm of the interferometer. One possible pulse shape, obtained via FFT from the optical spectrum, is depicted in figure 5.20(b). A pulse shape with only one leading or trailing pedestal may result in the same autocorrelation as well. Hence, conclusions about the exact pulse shape may not be drawn. Nevertheless, the following analytical approach allows to estimate how close the achieved pulse duration reaches to the fundamental limit set by the measured bandwidth.

In the first step the measured optical spectrum [plotted versus frequency, figure 5.20(a)] is Fourier transformed. This Fourier transformation yields one possible (shortest) pulse envelope of the E-field supported by the optical spectrum [figure 5.20(b)]]. With this theoretical pulse, an autocorrelation signal is calculated (figure 5.20(c), solid line), and to fit the calculated autocorrelation trace to the measured one (figure 5.20(c), dots), GVD and TOD are incorporated as fitting parameters. The best match of the measured and calculated autocorrelation trace is shown in figure 5.20(d), and was obtained adding a GVD of -2580 fs^2 and a TOD of $\approx$16,000 fs^3 to the theoretic E-field. The optical spectrum was found to theoretically support 134.5 fs. The above mentioned evaluation extracts a pulse duration of 142 fs from the measurement, which is about only 5% longer than the minimum supported pulse duration. The main laser parameters of the obtained laser results are grouped with the laser results of the following section and listed in table 5.6.

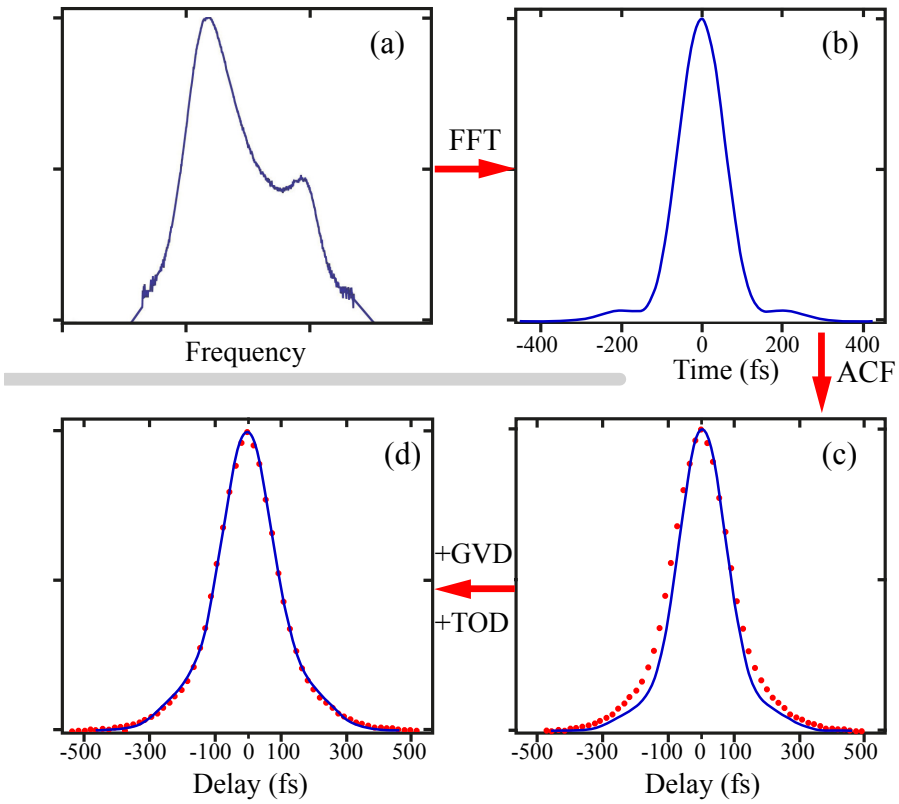

Figure 5.20: *Evaluation of pulses from a Tm:KLuW laser with asymmetric spectrum. (a) The optical spectrum is plotted vs. frequency and extrapolated to zero intensity. (b) The Fourier transform of the spectrum represents one possible shortest pulse theoretically supported. (c) The autocorrelation of this pulse (blue, solid) needs to be fit with the measured autocorrelation (red dots). (d) To compare the calculated autocorrelation (blue, solid) and the measured data (red dots), the E-field of (b) is charged with GDD and TOD before generating the autocorrelation. The amplitudes in all four figures are normalized to 1.*

The Tm:Lu_2O_3 laser - operation at zero dispersion

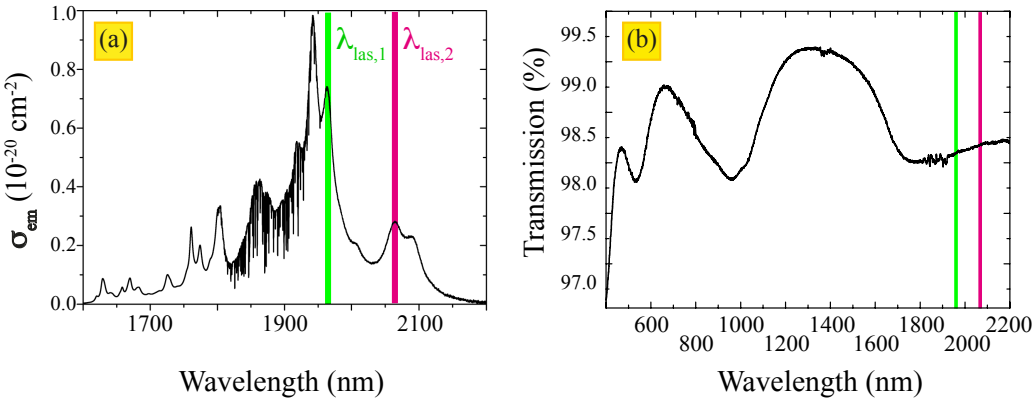

Figure 5.21: *Emission cross section of the $^3F_4 \rightarrow {}^3H_6$-transition of Tm^{3+} in Lu_2O_3 (a), and the linear transmission of the arc-made SWCNT-SA (b). The spectral position of the center wavelengths of the arc-made SWCNT-SA mode-locked Tm:Lu_2O_3 laser is denoted by the green and magenta lines, before and after replacing the cavity mirrors by high-pass dielectric mirrors, respectively. The high-pass mirror set shifts the emission wavelength above 2 µm, being better suited or mode-locked operation . The emission cross section of (a) is from [203].*

Apart from the Tm^{3+}-doped double tungstate KLuW, in this thesis, one representative of the class of sesquioxides (see section 4.1) was applied for pulse generation around 2 µm. The emission cross section of the $^3F_4 \rightarrow {}^3H_6$ transition of Tm^{3+} in lutetia (chemical formula Lu_2O_3) is shown in figure 5.21(a), together with the transmission of the arc-made SWCNT-SA (b). The operation wavelengths of the Tm:Lu_2O_3 laser are indicated by the green and magenta lines, using the broadband (highly reflective for 1.9 - 2.05 µm) and low-pass cavity mirrors (transmitting 8 and 84 % at 2000 and 1960 nm), respectively. Comparing the two crystalline hosts KLuW and Lu_2O_3, the emission cross sections [figures 5.16(a) and 5.21(a)] already indicate an inherent difference. The Tm:KLuW laser active material yields a maximum emission cross section around 1.85 µm, operating preferentially at wavelengths below 2 µm, whereas the Tm:Lu_2O_3 laser active material shows the maximum about 100 nm red-shifted, around 1.95 µm. The latter also features a spectral local maximum and a smooth optical spectrum in the wavelength range between 2.05 and 2.1 µm, being beneficial for mode-locked operation at wavelengths longer than 2 µm.

Figure 4.3(a) shows, that Lu_2O_3 yields a GVD close to zero at wavelengths around 1.95 µm. With the previously used cavity mirrors (highly reflective for wavelengths between 1.82 - 2.05 µm), the 1 at.% Tm-doped Lu_2O_3 crystal showed mode-locking without the prism pair, but rather long pulses of 31 ps were obtained.

Operating at a center wavelength of 1965 nm, the laser gain medium introduces a very small amount of negative GDD of about -10 fs^2 per round trip. The laser repetition rate amounts to 128 MHz, and 88 mW of average output power were obtained using the 1.5 % output coupler.

Shorter pulses were not obtainable and therefore, the CaF_2 prism pair and the set of low-pass mirrors were incorporated into the cavity. As the emission cross section is reduced by about a factor of three at wavelengths above 2 µm, mode-locking was not achievable with the 1 at.% Tm-doped crystal. The samples doped with 1.8 and 5 at.% Tm, in contrast, showed mode-locking in the femtosecond regime, accompanied by a shift of the center wavelengths to 2061 and 2070 nm, respectively. The wavelength shifts to these values because of a local peak in the emission cross section in this wavelength region (see figure 5.21(a) [203]).

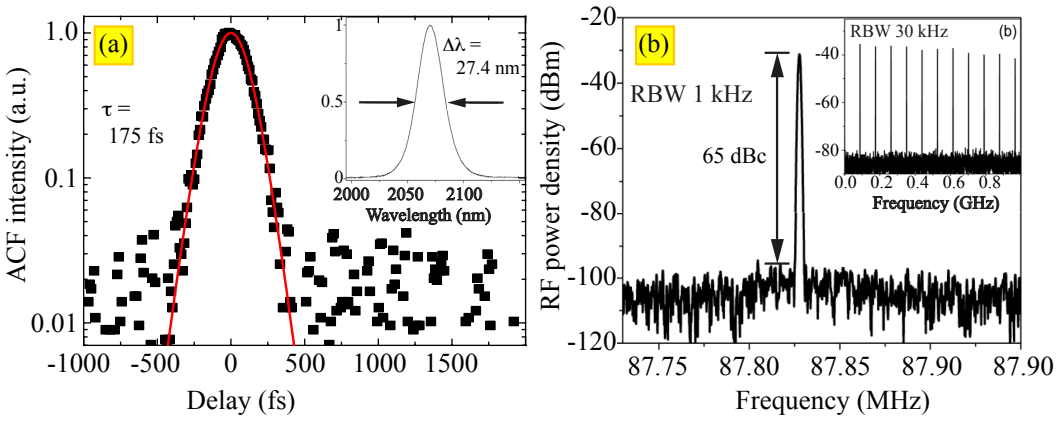

Figure 5.22: *Measured autocorrelation (a) of the arc SWCNT-SA mode-locked Tm:Lu_2O_3 laser. The optical spectrum (inset) is centered at 2070 nm. The RF spectra (b) show the fundamental beat-note and an 1 GHz scan (inset).*

The femtosecond mode-locked lasers yield a pulse duration of 279 and 175 fs, respectively. Due to a resonator length increase caused by the insertion of the prism pair in one resonator arm, the pulse repetition rate decreased to approximately 90 MHz. The obtained average output powers with the 1.8 and 5 at.% Tm-doped Lu_2O_3 are on the order of 30 mW. Figure 5.22 shows the semilogarithmic autocorrelation and optical spectrum (a), and the RF-spectra (b) of the arc-made SWCNT-SA mode locked 5 at.% Tm:Lu_2O_3 laser. Down to a normalized ACF intensity of $5 \cdot 10^{-3}$, the ACF fitting function nicely matches the data, whereas the wings of the autocorrelation data are governed by noise yielding fluctuating data. Section 5.6.2 further analyzes the soliton condition for assessment of the present mode-locking mechanism.

Active laser material	Central wavelength in nm	Pulse duration in fs	Average output power in mW	Repetition rate in MHz	Output coupling in %	Max. fluence on the SA in $\frac{\mu J}{cm^2}$	Necessary® SA replacement in mm	Reference	This work
Tm:KLuW	1944	9700	240	126	1.5	210	14	[154]	☒
	2037	141	26	88	0.2	240	15	[156]	☒
1.0 %	1965	31,000	88	126	1.5	75	-	[155]	☒
1.8 % - $Tm:Lu_2O_3$	2061	279	30	90	0.2	275	17		
5.0 %	2070	175	36	88	0.2	340	19		

Table 5.6: *Results arc SWCNT-SA mode-locked lasers at 2 µm (Tm-doped) obtained in this work.* ® *replacement necessary to obtain a saturation parameter of S=10, assuming Gaussian beam propagation and a minimum beam waist radius of 90 µm.*

The maximum fluence on the SAs listed in table 5.6 is in a similar range for the different lasers. Assuming a saturation fluence of 10 $\frac{\mu J}{cm^2}$ (table 5.2), the maximum saturation parameter for the SWCNT-SAs is in the order of 20-30. According to reference [88] a saturation parameter below 10 is necessary to avoid pulse-breakup (see section 4.5.2). The SWCNT-SAs designed for transmission allow to decrease the fluence by moving the absorber away from the beam waist in either direction (see figure 5.6), reducing the possibility of pulse-breakup[2]. The SA replacements necessary to avoid pulse-breakup are given in table 5.6 as well.

Assessment of the laser stability against QML-instabilities was performed according to section 4.5.1. In figure 5.23, the pulse energies of the laser results obtained with SWCNT-SAs are shown. The solid curve represents the critical pulse energy for cw mode-locking without Q-switching instabilities according to reference [88]. The plot indicates that all lasers are assumed stable against Q-switching. Compared to the other lasers under study, the pulse energies of the Tm-lasers are elevated, because of the low output coupling of 0.2 %. As the QML parameter $\beta_{\mathrm{QML}} \propto (\sigma_{\mathrm{em}})^{-1}$, the lower emission cross sections of Tm:KLuW and $Tm:Lu_2O_3$ at 2037, respectively 2070 nm, result in a larger β_{QML}. Due to the increased QML parameter, the critical pulse energy $E_{\mathrm{P,crit}}$ is increased by approximately $\sqrt{3}$. However, the Tm-doped lasers operate 7 and 9 times above the corresponding critical pulse energy $E_{\mathrm{P,crit}}$,

[2] One also has to consider that the assumed beam waist radii are calculated for ideal cavities. It is estimated that beam waist radii in real cavities may differ by 10 %.

resulting in an decreased probability for Q-switching instabilities.

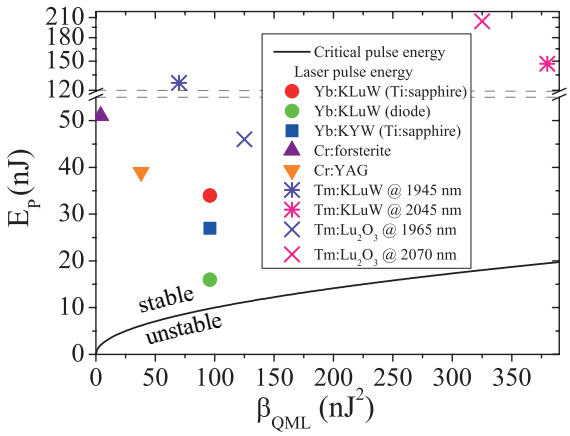

Figure 5.23: *Stability of cw mode-locking against Q-switching for all lasers of this work mode-locked with a SWCNT-SA. The solid curve represents the critical pulse energy vs. The QML parameter according to equation* (4.26)*. All pulse energies obtained for the different laser types (symbols) lie above the curve, indicating stable cw mode-locked operation.*

5.4.4 Broadband & octave-spanning application

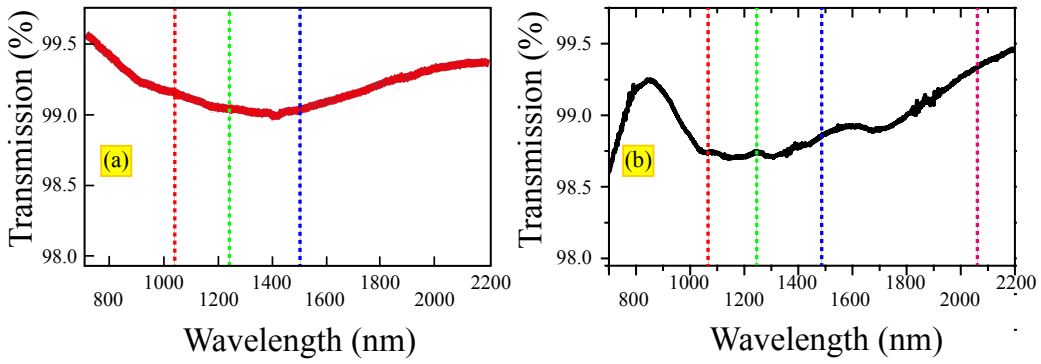

Figure 5.24: *Transmission spectra of the broadband HipCO-made SWCNT-SA (a) and the ultrabroadband (octave-spanning) HipCO+arc-made SWCNT-SA (b). The vertical lines denote the central wavelengths of the lasers that were mode-locked using the same corresponding absorber type. The colors denote the laser type, i.e., Yb:KYW and Yb:KLuW (red), Cr:forsterite (green), Cr:YAG (blue) and Tm:KLuW (magenta). The exact wavelengths are listed in table 5.7.*

As mentioned in section 2.3.4, some HipCO-made SWCNT-SA feature a relatively large diameter distribution, resulting in a broadband absorption, that may extend to wavelengths around 1 µm. Figure 5.24(a) shows the transmission spectrum of such a broadband HipCO-made SWCNT-SA. Figure 5.24(b) re-plots figure 2.15 from section 2.3.5, showing the octave spanning absorption of a SWCNT-SA based on the mixture of Arc- and HipCO-made SWCNTs. In the transmission spectra of both absorber types, the wavelengths of the lasers, mode-locked by means of the corresponding SWCNT-SA, are marked by the vertical lines.

As the SAs were produced via spin coating on a 1 mm thick quartz plate, application of one and the same absorber in different spectral regions was unproblematic. Mode-locking of all three, respectively four lasers was self-starting or could be initiated by a slight perturbation of the cavity, e.g., shaking a prism.

Figure 5.25 shows the measured autocorrelation traces of the four bulk lasers mode-locked with the ultrabroadband HipCo + Arc-made SWCNT-SA in a semilogarithmic plot. The pulses generated were nearly Fourier-limited for all lasers assuming a sech^2 shape and the durations measured were well below 200 fs in the case of Yb^{3+} and Cr^{4+}-doping and ≈ 550 fs for the Tm^{3+} laser. The fit to the data is good down to a normalized ACF intensity of $1 \cdot 10^{-2}$ or better. Table 5.7 lists the relevant laser parameters for the lasers mode-locked by the broadband and the ultrabroadband SWCNT-SAs. In the radio frequency spectra of all lasers, the noise level has

been measured to be at least 55 dB below carrier, and in none of the 1GHz span RF spectra parasitic frequencies were observed. This confirms stable cw mode-locking without Q-switching instabilities.

This successful application of one and the same SWCNT-SA in different spectral regions emphasized the versatility of SWCNTs over SESAMS. The latter are commonly designed for a defined spectral region and their application is limited to this wavelength range.

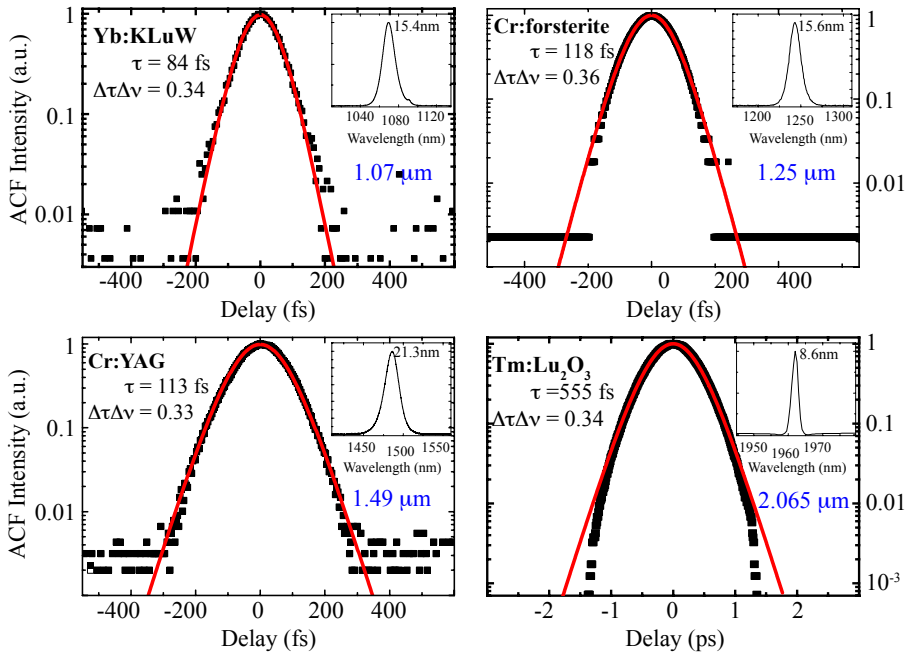

Figure 5.25: *Mode-locking of the 4 different lasers between 1 and 2 µm, using the octave spanning HipCO + arc-made SWCNT-SA. Each subplot shows the autocorrelation (black), the fit (red, solid) to the data, and the corresponding optical spectrum as inset. The center wavelength (blue), pulse duration and time-bandwidth product are given as well.*

Absorber used	Active laser material	Center wavelength in nm	Pulse duration in fs	Average output power in mW	Laser repetition rate in MHz	Output coupling in %	Max. fluence on SA in $\frac{\mu J}{cm^2}$	Necessary ⊛ SA replacement in mm	This work
Broadband SWCNT-SA	Yb:KYW	1040	133	160	87	1	300	34	☒
	Cr:forsterite	1240	100	230	79	7	350	6	
	Cr:YAG	1500	92	110	85	2	140	8	☒
Octave-spanning SWCNT-SA	Yb:KLuW	1070	84	62	90	1	110	9	☒
	Cr:forsterite	1250	118	250	79	7	380	7	
	Cr:YAG	1490	113	85	85	2	100	0	☒
	Tm:KLuW	2065	555	37	88	0.2	350	19	☒

Table 5.7: *Comparison of the main laser parameters using the broadband HipCO SWCNT-SA and the octave-spanning HipCO + arc SWCNT-SA. The Cr:forsterite laser was operated at the Ajou University Suwon, South Korea. Results published in references [75] and [80].* ⊛ *replacement necessary to obtain a saturation parameter of S=10.*

5.5 Graphene mode-locked bulk lasers

5.5.1 Ytterbium-doped laser

In this section the graphene-SA mode-locked Yb:KLuW is presented. The samples under study were produced via exfoliation as described in [23] and the laser setups are identical to the one applied for the SWCNT-SA mode-locked lasers (figure 5.6). In the first part of the experiment, the Yb:KLuW laser was pumped using a diode laser incorporating a distributed Bragg reflector[204] at 978 nm, and subsequently Ti:sapphire laser pumping was applied.

After optimization of the cw laser performance, the graphene SA and two SF10 prisms with a tip-to-tip separation of 39 cm were inserted into the resonator, operating at a pulse repetition frequency of 92.5 MHz. The positive second order dispersion introduced by SPM, the laser crystal and the quartz substrate of the SA is balanced by the negative dispersion introduced by the prisms (approximately -2400 fs^2, see section 5.4.1). The transition between cw operation and mode-locking occurs at an absorbed pump power of 660 mW for the 1 % OC. At the mode-locking threshold, the laser output power amounts to 16 mW. Figure 5.26(a) shows the semilogarithmic autocorrelation trace and the optical spectrum of the shortest pulses obtained. The ACF of an assumed $sech^2$ pulse profile well fits the data to a normalized ACF intensity of about $7 \cdot 10^{-3}$. The deconvolved FWHM of the shortest pulses is 160 fs at an

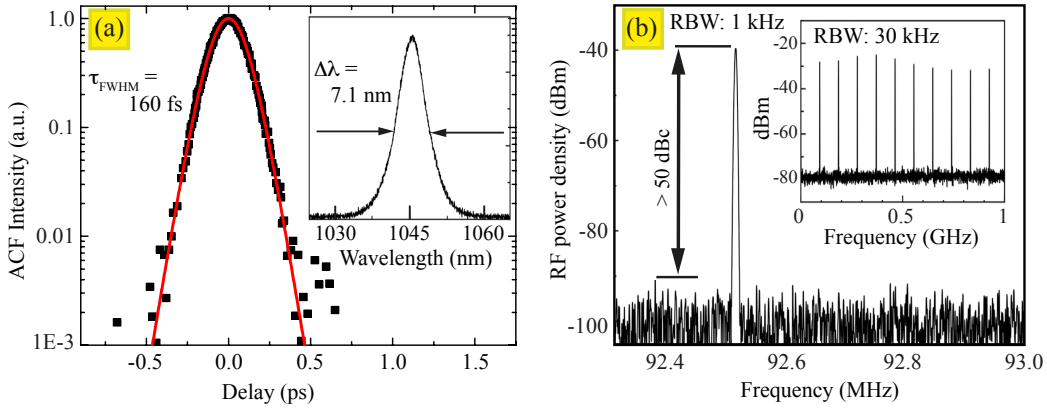

Figure 5.26: *(a) Measured autocorrelation trace and $sech^2$-fit of the graphene mode-locked Yb:KLuW laser. The corresponding optical spectrum is shown in the inset. (b) RF spectra of the laser, recorded at the repetition rate of $f_{rep} = 92.5$ MHz and a 1GHz scan (inset).*

average output power of 47 mW. The central wavelength of the emission spectrum is located at 1047 nm, and a bandwidth of 7.1 nm was measured. The calculated corresponding time-bandwidth product is 0.32, which nearly equals the Fourier limit.

Figure 5.26(b) depicts the radio frequency spectrum of the fundamental beat note at 92.5 MHz recorded with a RBW of 1 kHz and a 1 GHz wide-span measurement (inset) for the shortest pulse operation. The carrier is 50 dBc above the noise floor, and no spurious modulation can be seen in the RF spectra, indicating clean cw mode-locked operation.

The laser was not reliably self-starting, but already a slight perturbation initiated mode-locked operation. At the expense of a slightly longer pulse duration of 203 fs, higher output power of 160 mW was obtained using the 5 % OC. The central wavelength did not change, and the pulses remained bandwidth-limited. In this operation mode, the laser showed improved stability against perturbations and fine spectral tuning was easily realized. Placing a knife edge between the two prisms, a tuning range of 14 nm, from 1036 to 1050 nm was obtained. Tuning of the laser, the pulse duration slightly increased but pulse duration did not surpass 300 fs and the average output power loss due to tuning was below 30 %.

The active laser material theoretically supports pulses well below 100 fs [185]. Applying the graphene SA, it was possible to exploit this short-pulse potential to a certain degree. Pulse durations down to $\approx$ 90 fs were recorded, but stabilizing this regime was not possible.

Under Ti:sapphire laser pumping - allowing for a better overlap of the pump beam and resonator mode - mode-locking applying the graphene SA was possible, too. Using the single layer sample, pulse durations down to 84 fs were measured. To stabilize mode-locking against cw components and multi pulsing, spectral clipping by means of a knife edge (moved into the beampath between the two prisms, see figure 5.6) was necessary. This stabilization is obtained at the expense of the output power, decreasing by about 60 %, as compared to the laser without spectral clipping. The spectral clipping furthermore affected the bandwidth and hence pulse duration.

Figure 5.27 shows the semilogarithmic autocorrelation and corresponding optical spectrum of 95 fs pulses obtained with the graphene-SA, using the Ti:sapphire laser as pump source. The optical spectrum shown in the inset is centered at 1047 nm and shows an additional small peak at around 1070 nm, whereas the latter is not influenced by spectral clipping and persists in the optical spectrum. Despite the additional spectral peak, the autocorrelation is well fit by the ACF of a sech^2 pulse and yields a similar quality (down to an ACF intensity of ca. $0.7 \cdot 10^{-3}$) as the diode laser pumped result (figure 5.26). Spectral clipping was essential for operation in this mode, but his measure decreased the spectral bandwidth and increased the pulse duration by about 16 nm and 10 fs, respectively. Laser operation with very broad spectral bandwidth of 28 nm yield a non-soliton-like optical spectrum and a large TBP between 0.46 and 0.66. By slightly changing the spectral clipping, the bandwidth is reduced to 12.3 nm, yielding a TBP of 0.319, which is close to the theoretical limit for sech^2-shaped pulses. This operation mode is very sensitive and

fragile, and due to the disproportional number of obstacles, further studies of the graphene-SA mode-locked, Ti:sapphire laser pumped Yb:KLuW were not performed.

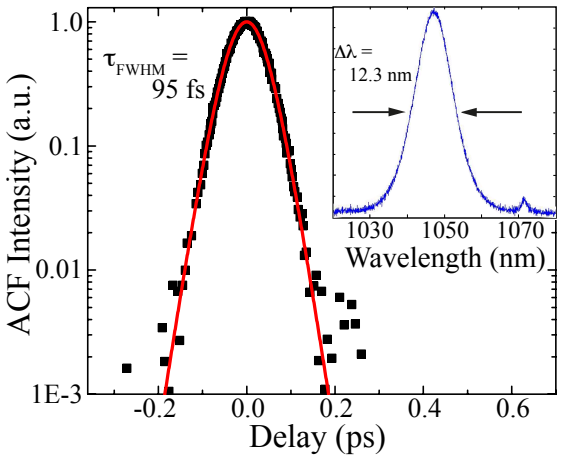

Figure 5.27: *Measured autocorrelation (dots) of the graphene-SA mode-locked Yb:KLuW laser. The fit to the data (red solid line) assumes a sech^2 pulse shape. A Ti:sapphire laser was used as pump source. The corresponding optical spectrum (inset) shows a local maximum at 1075 nm, even if spectral clipping is applied (see explanation in the text).*

Further laser parameters obtained in this work are listed in table 5.8.

As graphene's saturation fluence is approximately 50 $\frac{\mu J}{cm^2}$ (table 5.2 in section 5.1.4), the saturation parameter of the graphene-SA operated in the Yb:KLuW laser is in the order of 1.2-1.7. The analysis of the laser results with respect to the Q-switching stability introduced in chapter 4.5.1 is presented in figure 5.31 at the end of section 5.5.2.

Center wavelength in nm	Pulse duration in fs	Average output power in mW	Laser repetition rate in MHz	Output coupling in %	Max fluence on SA in $\frac{\mu J}{cm^2}$	Pump source	Reference	This work
1047	160	47	92.5	1	85	LD	[166]	☒
	203	160	92.5	5	60			
1040	84	45	92.5	1	80	Ti:Sa	-	☒

Table 5.8: *The main laser parameters of the graphene-SA mode-locked Yb:KLuW laser under study in this work. Ti:Sa indicates pumping with a Ti:sapphire laser, LD using a laser diode as pump source. A beam waist radius of 90 µm is assumed between mirrors M_3 and M_4 in the additional folding [figure 5.6(b)]4. The saturation parameter computes to a value of 1.2-1.7, therefore no replacement of the SA is necessary to avoid pulse-breakup (section 4.5.2).*

5.5.2 Chromium-doped lasers

The chromium YAG laser presented in section 5.4.2 has shown a good performance mode-locked using SWCNT-SAs. This performance motivated the operation of graphene as passive mode-locker in this laser.

The graphene sample was incorporated at the same position as the SWCNT-SA. After alignment the laser already showed the tendency of a modulated output, however, it did not enter the mode-locked regime by itself, yet a small perturbation was sufficient to start mode-locking. Once the laser was well aligned, it was self-starting in some cases.

During the first attempts of mode-locking with SWCNT and graphene-SAs, purging the cavity housing was essential for stabilization of the mode-locked operation. Notably, the laser was mode-locked and operated stable even *without* purging of the cavity housing in the subsequent experiments (using either SWCNT-SAs or graphene SAs). The explanation is given in section 5.4.2 on page 85. The Cr:YAG laser was analyzed using SHG FROG according to [205], and figure 5.28 shows the measured (a) and retrieved (b) FROG trace, respectively. The slight asymmetry of the measured FROG signal may be ascribed to temporal changes in the measured pulses during the measurement which took about 2 minutes. Furthermore, two different spectrum analyzers were used to measure the fundamental (APE Wavescan, not calibrated) and the second harmonic (Andor Newton) wave. However, the temporal drift is estimated less critical as it was possible to reproduce FROG-measurements several times until re-alignment of the laser was necessary.

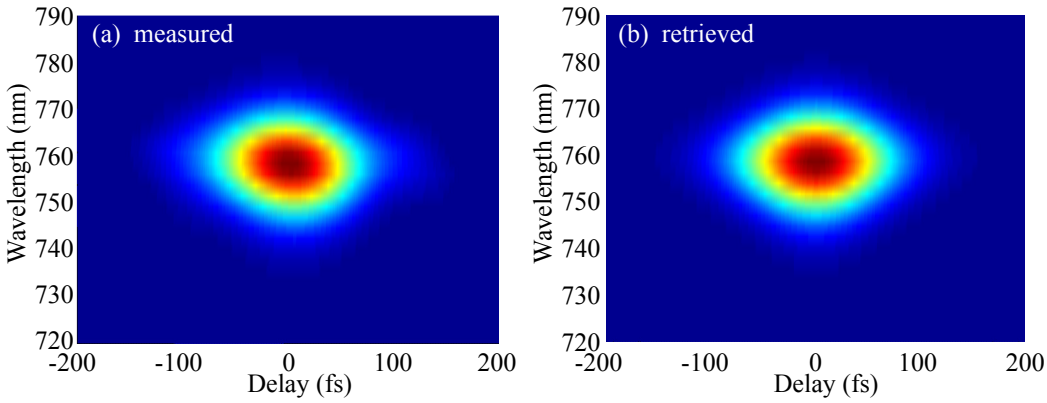

Figure 5.28: *Measured (a) and retrieved (b) FROG-traces of the graphene-SA mode-locked Cr:YAG laser. Retrieval on a 1024 × 1024 grid, a FROG error of 0.0013 is obtained.*

The original FROG-trace features spectral modulations that are Fourier filtered to obtain the DC part, *i.e.*, the intensity FROG trace. This SHG intensity FROG-trace was fed into the commercial retrieval program [118], and using a 1024 x 1024 pixel grid size, the smallest FROG error obtainable was 0.0013.

The FROG-retrieval extracted a pulse duration of the E-field envelope of 72 fs which is plotted in figure 5.29(a) together with the temporal phase. The retrieved optical spectrum, the measured optical spectrum and the spectral phase are shown in figure 5.29(b). The retrieved spectrum had a FWHM of ≈ 41 nm, whereas the measured spectrum encompasses 36.5 nm. This discrepancy is unusual, as a narrower

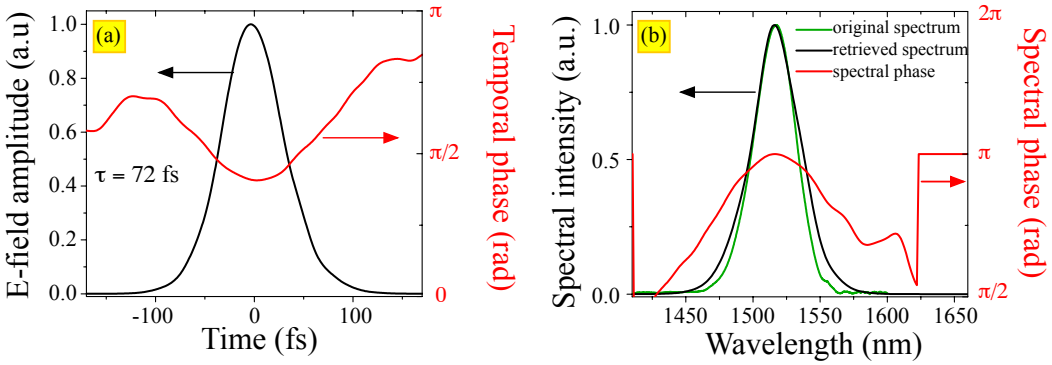

Figure 5.29: *(a) The retrieved electric field envelope (black) and the according temporal phase (red) of the graphene-SA mode-locked Cr:YAG laser. (b) The measured (black) and retrieved (green) optical spectrum. The spectral phase is plotted in red, 2nd y-axis. Figure published in [168].*

retrieved spectrum seems more probable (*e.g.*, due to spectral clipping in the SHG

process because of imperfect phase-matching over the whole spectral bandwidth). However, the retrieved spectra are systematically broader than the measured ones.

The source of this systematic error is not ultimately located yet, but the observed phenomenon is probably due to the use of two different spectrometers for the fundamental- and SHG spectrum (the λ^2-correction is implemented in the spectrometer and FROG software). Especially the spectrum analyzer used for the fundamental wavelength range seems to be responsible for this error, as it was operated at the end of its detection range (1.6 µm) and seems to suffer from improper calibration (baseline is bent upwards).

The FROG technique allows for consistency checks of the measurements [180], namely the frequency marginal, which is simply speaking the SHG-intensity-FROG-trace integrated over time. The frequency marginal of this measurement is shown in

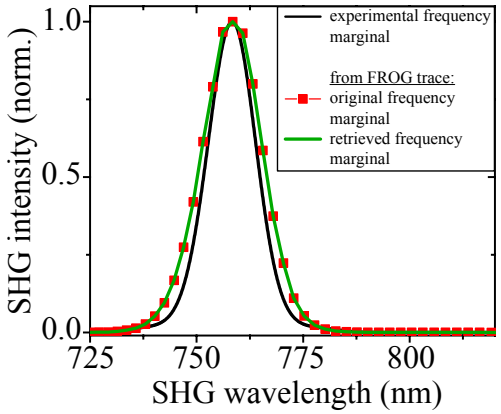

Figure 5.30: *Frequency marginal of the graphene-SA mode-locked Cr:YAG laser. The frequency marginal from the measured FROG trace [figure 5.28(a)] given by the red squares and line coincides with the frequency marginal from the retrieved FROG trace [figure 5.28(b)] plotted in green. The experimental frequency marginal (black) is narrower due to the spectrometer used (see text).*

figure 5.30. The marginals calculated from the measured and retrieved FROG trace agree nicely with each other, whereas the discrepancy in spectral bandwidth is clearly reflected in the frequency marginal calculated from the original optical spectrum. The latter frequency marginal corresponds to the SHG spectrum calculated from the fundamental spectrum. The central wavelengths agree very well, but because of the above mentioned obstacles due to the spectrometer for the 1.5 µm range, the measured bandwidths do not agree with each other.

Calculating the time bandwidth product using the FWHM of the optical spectrum of 41 nm (36.5 nm), a value of 0.388 (0.343) is obtained for the time-bandwidth product. Hence the obtained pulses are approximately 23% (9%) longer than the

Active laser material	Central wavelength in nm	Pulse duration in fs	Average output power in mW	Laser repetition rate in MHz	Output coupling in %	Min. beam waist radius on SA in µm	Max. fluence on SA in $\frac{\mu J}{cm^2}$	Necessary® SA replacement in mm	Reference	This work
Cr:forsterite	1240	94	230	74.6	5	40	515	6.5	[100]	
Cr:YAG	1516	91	107	85	2	80	130	0	[168]	☒
		72	90				110	0	-	☒

Table 5.9: *Results of the graphene-SA mode-locked chromium lasers. The Cr:forsterite laser was operated at the Ajou University in Suwon, South Korea, and listed for comparison as it was operated with the same graphene-SA.*

Fourier limited pulse duration of 58 fs (66 fs). The potential for shorter pulse durations has been shown in section 5.4.2 and the time-bandwidth product indicates that further pulse shortening may be possible. Dispersion compensation inside the cavity is one aspect for optimization of a laser towards shortest pulses. The dispersion present in the pulse can be extracted from the spectral phase plot. The procedure to determine the second order dispersion is presented in section 5.4.2 on page 85. Here a residual quadratic chirp of approximately $-520\,fs^2$ is found. This value includes the GVD due to the output coupler material, *i.e.*, about 5 mm fused silica, introducing approximately -150 fs^2 and the material dispersion of the beam-splitter of the FROG apparatus. The value of approximately -350 fs^2 confirms the soliton-like operation of the Cr:YAG laser in the net negative dispersion regime [189, 192, 206]. Addidionally, this value has the same order of magnitude as the SWCNT-SA mode-locked Cr:YAG laser (section 5.4.2), but unfortunately the laser was too sensitive against realignment of the cavity during operation. Therefore a systematic study of the obtainable pulse duration with respect to the amount of intracavity dispersion was not realizable.

With the measured saturation fluence of the graphene-SA around 1.25 and 1.50 µm of approximately 14 $\frac{\mu J}{cm^2}$(table 5.2), the saturation parameter of the SA calculates to be about 9 for the Cr:YAG laser, being uncritical for the occurence of pulse-breakup (section 4.5.2). In case of the Cr:forsterite laser, a displacement of the graphene-SA of only 6.5 mm is sufficient to reduce the saturation parameter from above 30 down to 10.

Similar to the SWCNT-SA mode-locking results, the stability of the graphene-SA mode-locked lasers against Q-switching is assessed according to section 4.5.1. Figure 5.31 plots the critical pulse energy of equation (4.26) as function of the QML parameter (solid line) and the pulse energies of the laser results obtained. For the sake of completeness, the Cr:forsterite laser results from reference [100] are given as well. Data plotted as line and scatter show the resulting pulse energy as function of a range of β_{QML}, because the calculation is based on a range of the laser beam waist on the SA.

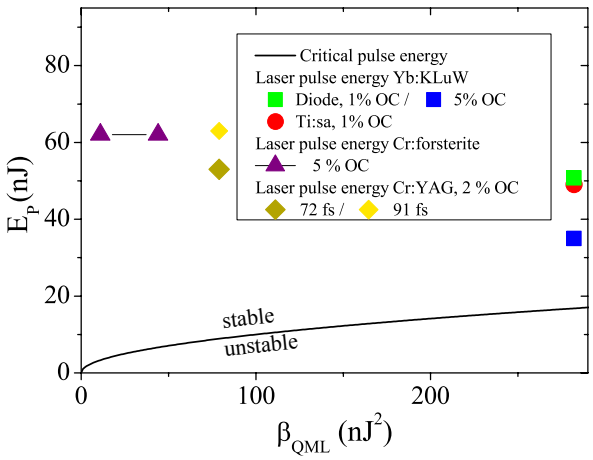

Figure 5.31: *Stability of cw mode-locking against Q-switching for the graphene SA mode-locked Yb- and Cr-lasers. The solid curve represents the critical pulse energy vs. QML parameter according to equation* (4.26)*. The pulse energies obtained for the different laser types (symbols) are larger than the calculated critical pulse energy, indicating stable cw mode-locked operation.*

5.6 Discussion of nanostructure-SA mode-locked laser results

5.6.1 General remarks

SWCNT-SAs and graphene yield an intrinsically fast relaxation time τ_{eff}, and in order to be suitable for bulk laser mode-locking, they were tailored to show a low modulation depth ΔR, a low saturation fluence F_{sat} and low non-linear losses l_{nl}. These SA parameters are listed in table 5.1 and 5.2. Although being related to each other, SAs based on graphene and SWCNTs show some general differences.

1. The absorption of graphene is fixed to ≈2.3 %. Higher values may be tailored by use of multiple graphene layers (section 3.4), actually resulting in graphite samples (graphene's properties merge into those of graphite). Deviations in the uniform absorption to smaller values indicate a fill-factor smaller than 1 (*i.e.*, 'holes' may be found in the graphene layer). A higher absorption per layer corroborates large scattering losses due to inferior sample quality.

2. The intrinsic (theoretical) upper limit for the modulation depth is given by the graphene absorption of 2.3 %. Measured modulation depths listed in table 5.2 show, that nearly 80 % of the absorption may be saturated, however, ΔT denotes a decrease with increasing wavelength, *i.e.*, energetically closer to the K-point, the modulation depth becomes smaller. This may be explained by a non-zero Fermi level (figure 2.2).

3. The saturation fluence of graphene-SAs used in this work is higher than for SWCNT-SAs[3]. As the cc-scattering times of both nanostructures are similar (section 3.2), it is supposed, that the fill-factor of the SWCNT-SA is the reason for the lower saturation fluence. As conceivable from SEM and TEM measurements (figure 2.13), the fill factor of the samples under study is clearly below 1, *i.e.*, the number of available electronic states per area is lower than for graphene[4], saturating already with lower incident fluence.

4. From table 5.1 it becomes clear, that graphene and SWCNTs yield comparable recovery times. However, with increasing wavelengths, *i.e.*, approaching the K-point of graphene, the integral weight of the slow time constant increases. This is explained by the fact that fast cc-scattering becomes less efficient in the vicinity of the K-point (section 5.1.3, reference [171]).

[3] With SWCNT-SAs applied for fiber lasers, saturation fluences of up to 320 and 1000 $\frac{\mu J}{cm^2}$ were reported for wavelengths of 1.56 and 1.05 µm, respectively [175]

[4] The DOS of graphene and SWCNTs are only comparable for given energy values. However, due to the presence of a large number of different SWCNTs in the sample, the averaged DOS of SWCNTs is comparable to the one for graphene (see *e.g.*, figure 3 in reference [207])

5.6.2 Soliton-like mode-locking

For assessment of the mode-locking mechanism underlying the lasers in this work, the soliton condition (equation (4.23) on page 52) is evaluated. Therefore, several laser and material parameters need to be known or estimated to the best of knowledge.

Table 5.10 lists these parameters and estimations for the lasers operating in the four spectral regions. For the peak intensity I_0, the formula

$$I_0 = \frac{2}{A(w)} \cdot P_{\text{peak}} \approx \frac{2}{\pi \cdot w^2} \cdot \underbrace{0.88 \cdot \frac{1}{\tau_{\text{p}}} \cdot E_{\text{p}}}_{\approx P_{\text{peak}}} \approx \frac{2}{\pi \cdot w^2} \cdot 0.88 \cdot \frac{1}{\tau_{\text{p}}} \cdot \underbrace{\frac{P_{\text{avg}}}{f_{\text{rep}}}}_{=E_{\text{p}}} \tag{5.6}$$

is applied. The left-hand side (lhs) of equation (4.23) thus depends on the laser wavelength λ, the nonlinear refractive index n_2, the beam waist radius in the laser medium w, the FWHM pulse duration τ_{p}, the average intracavity power P_{avg}, and the laser repetition rate f_{rep}. The right-hand side (rhs) of equation (4.23) depends on the calculation of the prism round-trip GDD (section 4.2.2), corrected by the round-trip GDD introduced by the active laser medium (section 4.2.1), and the pulse duration.

The integral in the lhs of equation (4.23) considers Gaussian propagation in the crystal. For small crystal thicknesses (few millimeters), it may be approximated by the multiplication of n_2 and the crystal length, but for thicker crystal, *e.g.*, the Cr:YAG laser crystal, this approximation is not valid any longer.

Laser	λ (nm)	n_2 ($10^{-20}\,\text{m}^2\text{W}^{-1}$)	w (µm)	τ_{p} (fs)	P_{avg} (W)	f_{rep} (MHz)	β_2 (fs^2)	lhs eq. (4.23)	rhs eq. (4.23)
Yb:KLuW	1048	8.7	30	115	3	89	- 1620	0.60	0.12
Cr:YAG	1500	3.85$^{\diamond}$	24 & 37$^{\circledast}$	48	3.35	85	-850	$\approx$ 1.31$^{\otimes}$	0.37
Tm:KLuW	2037	8.7	33	141	13.25	88	-2720	0.88	0.14
Tm:Lu_2O_3	2070	5.8	33	175	9.0‡	88	-1280	0.318	0.042

Table 5.10: *Parameters for assessment of the soliton condition for the lasers under study.* $^{\diamond}$ *averaged value determined by references [208], [209], and [210];* $^{\circledast}$ *Lengths of the main axes of the elliptical beam;* $^{\otimes}$ *Depending on the resonator geometry and crystal displacement, the beam waist is not centered in the laser crystal, this calculation was performed for zero displacement, table 5.6.2 assesses crystal displacement;* ‡ *The OCs are specified from 1850 up to 2050 nm. At 2070 nm the OC transmission already increased to 0.4% according to the suppliers transmission measurement.*

Table 5.10 lists the parameters used for assessment of the soliton condition, *i.e.*, by comparing the lhs and rhs of equation (4.23). The beam waist radius w and the round-trip GDD β_2 are calculated *ideal* values, which may differ from values present in the laser cavity.

From the table it is discernible that the lhs and rhs of equation (4.23) differ by about a factor of 5 for the four lasers. This fact actually would disprove the presence of solitons, although the other means of laser characterization (ACF, RF and optical spectrum), indicate clean soliton mode-locking. Actually, some parameters are not well known and an exemplary model calculation for the Cr:YAG laser will assess possible reasons for this discrepancy.

The nonlinear refractive index n_2 may be estimated from the YAG band gap, which is found in literature with values of 6.73 and 6.5 eV [208, 209], and used to determine n_2 via a Kramer-Kronig relation presented in [210]. This results in an n_2 of 3.6 and $4.1{\cdot}10^{-20}\,\mathrm{m^2W^{-1}}$, whereas an average value of $n_2 = 3.85{\cdot}10^{-20}\,\mathrm{m^2W^{-1}}$ is assumed for calculation.

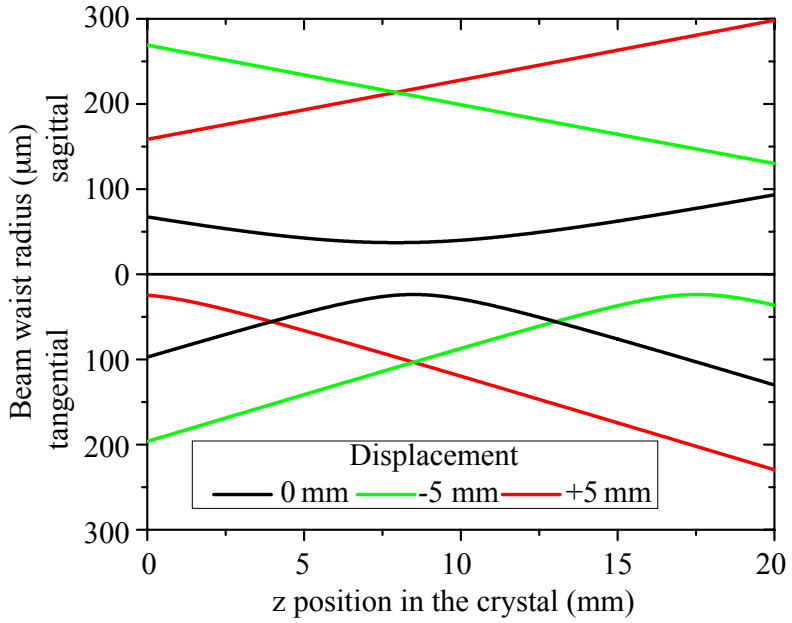

Figure 5.32: *Beam waist radii in the Cr:YAG crystal for different crystal displacements and for the sagittal and tangential plane in the upper and lower panel, respectively. The tangential beam waist radius remains constant but its position depends on the crystal displacement, whereas the sagittal beam waist is not located in the crystal for some displacements. In this case the beam waist radius may be described by a linear function.*

Crystal displacement in mm	lhs of eq. (4.23), $n_2 = 3.85 \cdot 10^{-20}\,\frac{\mathrm{m}^2}{\mathrm{W}-\mathrm{I}}$ [208, 209]
-5	0.303
-4	0.424
-3	0.607
-2	0.920
-1	1.227
0	1.311
+1	1.081
+2	0.710
+3	0.460
+4	0.300
+5	0.220

Table 5.11: Calculated lhs of sol. condition vs. displacement, rhs=0.369.

The beam waist radius w inside the active laser medium is described by Gaussian propagation and changes significantly with crystal displacement. Figure 5.32 shows exemplary the beam waist in the Cr:YAG crystal for the sagittal and tangential plane for three individual crystal positions. Table 5.6.2 lists the lhs of the soliton condition for 10 different displacements of the crystal, and shows that a displacement of approximately 4 mm is sufficient to explain the discrepancy. Similar considerations were made on the other laser results, summarized in table 5.12. The table indicates that the soliton condition is fulfilled by a minor change in the cavity set-up, whereas such changes are realistic in laser operation.

Laser	lhs eq. (4.23), ideal geometry	rhs eq. (4.23)	Crystal displacement Δz (mm)	*New* lhs after variation	*New* rhs after variation	Comment
Yb:KLuW	0.60	0.12	2 mm	0.16	0.12	The crystal translation is actually used for laser alignment and this displacement is realistic.
Cr:YAG	≈ 1.31	0.37	3.5 mm	0.38	0.37	If ΔGDD=-300 fs^2 ⊛ is assumed in combination, Δz for equality lhs=rhs is 2.5 mm, which is realistic.
Tm:KLuW	0.88	0.14	2 mm	0.15	0.14	The crystal translation is actually used for laser alignment and this displacement is realistic.
Tm:Lu_2O_3	0.318	0.042	2 mm	0.053	0.042	The crystal translation is actually used for laser alignment and this displacement is realistic.

Table 5.12: *Assessment of the soliton condition incorporating a laser crystal displacement.* ⊛ *This change in GDD corresponds to a prism insertion of 1 mm, instead of 2 mm.*

5.6.3 Relevance of the SA's and material parameters

Significance of the integral weight of τ_2

The self-starting behavior of the SWCNT-SA mode-locked lasers is inferior compared to the usage of SESAMs. The latter yield a dominant slow relaxation time constant τ_2 of several picoseconds, which is beneficial for self-starting [174]. As presented in table 5.1, and apparent from figure 5.4, in contrast to SESAMs, the relaxation times of SWCNT-SAs are dominated by the fast relaxation time constant τ_1.

The integral weight $w_{\tau_2,SESAM}$ of a classical SESAM is close to 100 %, indicating that the relaxation process in the SESAM is governed by the slow relaxation component. In the SWCNT-SAs the integral weight $w_{\tau_2,SWCNT}$ is in the order of 70 %. The difference for self-starting may be pictured as follows. With a dominating slow relaxation component, an initial perturbation from the noise may saturate the SA to a certain extend. The reduced loss due to this saturation represents a net gain window that allows the growth and amplification of further intensity fluctuations. If the fast time constant relaxes the absorber too quickly, the recovered SA attenuates the intensity fluctuations following the first event. Consequently, the probability decreases that a subsequently following intensity fluctuation experiences sufficient gain to gather the energy necessary for saturation of the SA.

Due to the decreased influence of the slow relaxation component of SWCNT-SAs, achieving self-starting with the lasers under study is not intrinsically facilitated and demands for careful alignment. In case a laser under study is not self-starting, it required only a small perturbation for initiation of the pulsed regime. Usually the laser is sensitive enough that softly touching a mirror holder starts mode-locking. Once started, laser operation was stable.

In general, the integral weight of the slow time constant (table 5.1) of the graphene-SAs tends to be equal or even smaller than for SWCNT-SAs. This trend is directly transfered to the self-starting behavior of graphene-SA mode-locked lasers. It is challenging to find a self-starting configuration, but with proper cavity alignment without self-starting, a slight perturbation suffices to initiate mode-locking.

Significance of the low SWCNT-SA modulation depth

The designed SWCNT-SAs yield a very low modulation depth well below 1 %. This low modulation depth is required for mode-locking of bulk lasers [5], and is additionally beneficial to suppress QML instabilities (section 4.5.1). It furthermore decreases the non-saturable losses in the cavity, as they scale with the modulation depth. Although these low transmission changes are sufficient for discrimination of mode-locking against cw operation, already minor changes of a laser parameter may result in laser instabilities or in termination of mode-locking. Stable mode-locked laser operation is therefore more fragile using SWCNT-SAs and modifying laser parameters, *e.g.*, during the attempt to measure the slope efficiency, demands for careful attention.

[5] In reference [211], a $\Delta R_{\mathrm{mod}} = 37\,\%$ is used.

Significance of the low SWCNT-SA saturation fluence

Similar to the designed low modulation depth, the low saturation fluence (<10 $\frac{\mu J}{cm^2}$) of the SWCNT-SAs decreases the critical pulse energy to suppress QML instabilities (see figure 5.9 and the corresponding information in the text).

On the one hand, using a low F_{sat} SWCNT-SA results in reaching the mode-locking threshold already at laser operation slightly above the lasing threshold, on the other hand, a very low saturation fluence tends to be saturated with an 10 - 30 times lower incident fluence, compared to a graphene-SA or a typical SESAM (yielding an $F_{sat} \approx 150 \frac{\mu J}{cm^2}$). A possible over-saturation of the SWCNT-SA may be easily avoided using SWCNT-SAs designed for operation in transmission, allowing to move these elements along the cavity laser beam axis out of the beam waist of the second folding between M_3 and M_4 (see figure 5.6), and subsequently reducing the fluence on the SA. Considering, *e.g.*, the Yb:KLuW laser with two spherical mirrors of ROC_{M3}=-100 and ROC_{M4}=-50 mm, the beam waist in the folding calculates to 90 µm. As focusing follows Gaussian propagation, the absorber in transmission needs to be translated by approximately 25 mm (in either direction along the laser beam axis) in order to change the fluence on the SA by a factor of two..

In the Cr:YAG laser, strong spectral modulations and multiple pulsing occurred for higher pump power $P_{Pump} \gtrapprox 4.26$ W. Although reduction of the saturation parameter to 10 ($S \approx 22$ for the SA positioned in the vicinity of the beam waist) is possible by translating the SA 15 mm along the beam propagation, mode-locking may not be stabilized for a higher incident fluence on the SA.

As denoted in section 5.1.2, TPA is not observed in the non-linear transmission measurements. Consequently, the SWCNT-SA transmission change does not experience a roll-over and no damage occurs to the SWCNT-SA[6].

Significance of the low non-saturable loss

The low non-saturable losses of SWCNT-SAs in the order of 1-2 %, are beneficial for the overall laser performance and for the lasers self-starting behavior.

Increasing gain as well as decreasing losses are found conducive for self-starting [174]. The latter may be observed directly in the Cr:YAG laser operating at a center wavelength below 1.5 µm. In this operation mode, the laser is quite sensitive to a disturbance of the purging. As soon, as the box is opened for alignment, instead of a smooth optical spectrum, the laser shows a spectral output denoting random

[6] A different process leading to damage of the SWCNT-SA in the Yb:KLuW laser is discussed in section 5.4.1 on page 80.

coherent interferences of the cw components present. In this case either the random constructive interference of the cavity modes is not sufficient to *push* the laser out of the noise, over an entropic barrier into the region of mode-locking [212], or the mode-locked pulse is not stable enough to be maintained inside the cavity. Also with time, the laser does not cross the barrier on its own. Closing the box without further touching the cavity, the former fills with dry nitrogen, replaces the ambient air and continuously decreases the water vapor absorption. After a limited purging time the laser self-starts from the 'noisy' fluctuating cw components and remains stably mode-locked.

Significance of the SA's saturation parameter

The fluences given in tables 5.4.1, 5.5, 5.6 and 5.7 for the SWCNT-SA mode-locked lasers, as well as tables 5.8 and 5.9 for the graphene-SA mode-locked lasers, in combination with the measured saturation fluences (table 5.2), allow to assess the SA's saturation parameter S. The values of S are listed in table 5.13 for comparison of the laser results.

Laser active ion (λ region)	Saturation parameter S of the corresponding SWCNT-SA mode-locked laser	Saturation parameter S of the corresponding graphene-SA mode-locked laser
Yb^{3+} (1.0 µm)	5-10 (30†)	1.2-1.7
Cr^{4+} (1.3 µm)	35-70‡	35‡
Cr^{4+} (1.5 µm)	10-22	8-9
Tm^{3+} (2.0 µm)	21-35	no ml with available samples

Table 5.13: *Saturation parameters of the SWCNT and graphene-SA mode-locked lasers of this work.* † *indicates values obtaineed with the HipCO SWCNT-SA operated around 1 µm,* ‡ *- The Cr:forsterite laser was operated at Ajou university Suwon, South Korea, using the same SWCNT-SA samples. Values given for comparison.*

The saturation parameter is widely comparable for the lasers under study. According to reference [88], a value of S below 10 is favorable to avoid pulse-breakup. As the SWCNT-SAs are designed for transmission, the oversaturation of the SA is avoided in the lasers under study by means of translating the SA along the cavity beam axis by several millimeters (values given in the according tables).

Using the graphene-SA, the saturation parameter is decreased due to graphene's higher modulation depth (table 5.2). In the spectral region around 1 µm, the

graphene-SA is operated slightly above saturation. Figure 5.33 (taken from reference [136]) plots the loss difference between the double and single pulse solution Δq_S normalized to the modulation depth q_0 as function of the saturation parameter S. The optimum discrimination between the single and double pulse solution was

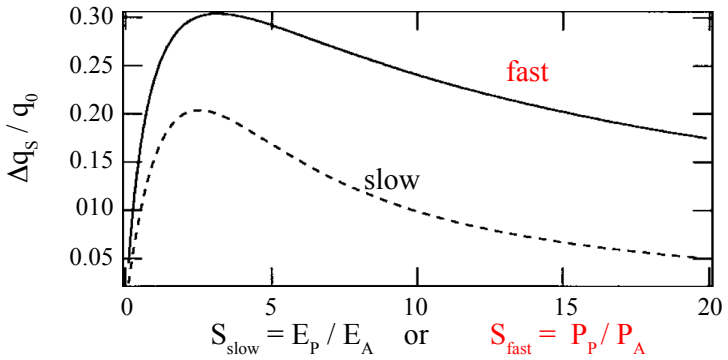

Figure 5.33: *Discrimination of single pulses against double pulses as function of the saturation parameter. A slow SA (dashed) saturates with pulse energy, whereas as fast absorber (solid) saturates with pulse peak power. The ratio* $\frac{\Delta q_S}{q_0}$ *is the difference between losses of the double puse solution and the single pulse solution normalized to the modulation depth. Figure from reference [136].*

found for a saturation parameter of 3 [136] and the plot indicates that values in the order of 1 yield a lower single pulse discrimination than an $1 < S \lessapprox 15$. The values for S given in table 5.13 actually denote the maximum saturation parameter, hence, the saturation parameter is expected even smaller. Figure 5.33 explains the inferior laser stability of the graphene-SA mode locked Yb:KLuW laser at 1040 and 1047 nm. The saturation parameter for these two lasers is well below the optimum, leading to a decreased discrimination against pulse-breakup. In the wavelength region around 1.3 µm, the graphene-SA needs to be moved out of the beam waist by 6.5 mm to obtain $S = 10$, and the eight to ninefold saturation of the graphene-SA around 1.5 µm, yields *a priori* no tendency for pulse-breakup in the given configuration.

Effects of laser active material properties

Naturally, the properties of the laser active materials - composed of dopant and host - play a major role for the mode-locking performance and stability. Cr^{4+}-doped YAG, for example, yields a larger emission cross section (and hence effective gain cross section [213]) compared to Yb:KLuW ([108], section 5.4.1). This fact is directly noticeable in the value of the QML parameter β_{QML}, as $F_{\mathrm{sat,L}} \propto \sigma_{\mathrm{em}}^{-1}$ (section 4.5.1). Because of a reduction of β_{QML} by more than a factor of 2 and 9 for the Cr:YAG and Cr:forsterite laser, respectively, the critical pulse energy $E_{\mathrm{P,crit}}$

is reduced by a factor of $\sqrt{2}$ and 3, respectively. The opposite trend is observed with the Tm:KLuW and Tm:Lu_2O_3 when operated above 2 µm wavelength. The decreasing emission cross sections of both active laser materials (see figures 5.16 and 5.21) lead to an increase in the QML parameter and critical pulse energy for stable cw mode-locking without Q-switching instabilities. The latter increase was not critical for the lasers under study, as lower output coupling led to an increased pulse energy substantially larger than the critical value (see figure 5.23).

Chapter 6

Conclusion and Outlook

In this work, novel SAs based on SWCNTs and graphene have been investigated and characterized. The design of SWCNT-SAs parameters like SWCNT concentration or SWCNT mean diameter allowed for realization of mode-locking in different wavelength regions from 0.8 [103] to 2.1 µm [155], with sub-200 fs pulses obtained. The broadband non-linear response of HipCO SWCNTs enabled quasi-continuous mode-locking between 1.0 - 1.5 µm, demonstrated with three laser types operating in this wavelength range mode-locked with one and the same SWCNT-SA. Furthermore, a single SWCNT-SA device was designed, operating between 0.8 and 2.1 µm. In conclusion the main findings of this work are

- the first demonstration of an SWCNT-SA cw mode-locked bulk laser at 2 µm,
- the first sub-100 fs bulk laser pulses at 1 µm, with an SWCNT or graphene-SA,
- the shortest pulse durations (sub-50 & sub-100 fs) demonstrated for the combination of a bulk Cr:YAG laser at 1.5 µm and carbon nanostructure SAs based on SWCNTs and graphene,respectively, and
- application of the same SWCNT-SA over a broad spectral range of 1.0 - 1.5 µm as well as an octave-spanning operation from 1.0 to 2.1 µm.

Degenerate pump-probe spectroscopy and nonlinear transmission measurements were used to extract the relaxation times, the nonsaturable losses, the modulation depth and the saturation fluence of the SAs, showing, that

- For SWCNTs the fast relaxation time was measured to be on the order of 100 - 300 fs, whereas the slow relaxation time is on the order of 2 - 3 ps.
- For graphene the fast relaxation time was determined to be on the order of 100 fs as well and the slow relaxation time approximately 3.5 ps.

- For graphene the integrated weighting of the slow time constant is equal or smaller to those obtained for SWCNT-SAs, which corroborates the inferior self-starting behavior compared to the SWCNT-SA mode-locked lasers.
- The non-saturable losses of the SWCNT and graphene-SAs amount to approximately 1-2%, and modulation depths below 1% were measured.
- From NLT measurements, a saturation fluence of about 10 $\frac{\mu J}{cm^2}$ was extracted for SWCNT-SAs, whereas the saturation fluence of the graphene-SAs is on the order of 50 and 15 $\frac{\mu J}{cm^2}$ for wavelengths of 800 - 1040 nm and 1250 - 1500 nm, respectively.

Although being critical, self-starting laser configurations may be found, and if a configuration did not show self-starting, only a slight perturbation of the cavity is sufficient to initiate mode-locking. Differences in the self-starting behavior are observed between the laser types as well. The Yb-laser emitting at 1 µm is hardly self-starting due to a low integral weight of the slow component of 72 %. At 1.5 µm(Cr:YAG), the laser shows an increased tendency for self-starting, which is counter-intuitive at first sight, as the influence of the slow relaxation component is smaller at this wavelength (66 %). The higher emission cross section of Cr:YAG (about a factor of ten compared to Yb:KLuW, [213]) is assumed responsible for the higher tendency to self-start.

The applicability of the graphene-SA did not fully match the expectations towards its versatility, but applying the same graphene-SA resulted in mode-locked operation at wavelengths between 1.0 and 1.5 µm. However, in general lasing was less stable as compared to SWCNT-SA mode-locking, and to date it was not possible at 2 µm with the samples available. Apart from this exception, all combinations of lasers and nanostructure-SAs resulted in mode-locked operation with a laser performance comparable to SESAM mode-locked results. The pulse durations were found to be as short as 83 and 48 fs for the Yb^{3+}- and Cr^{4+}- lasers, respectively. For the Tm^{3+}-laser a pulse duration down to 141 fs was achieved.

In conclusion, this thesis shows that carbon nanostructure based SAs are well suited to mode-lock solid-state bulk lasers. SAs based on SWCNTs or graphene, have become a match to SESAMS and regarding the improvements of the last years, carbon-based nanostructure SAs may soon become a serious competitor to SESAMs.

6.1 Outlook

By now, certain obstacles prevent an *unproblematic* replacement of SESAMs by SWCNT or graphene-SAs. SWCNTs yield an elevated damage threshold as compared to semiconductors. Unfortunately the embedding polymer matrix does not feature the same damage threshold under tight focusing. The transmissive nature of the SAs used, however, allows to avoid this damage by moving the SA out of the cavity beam waist. The increase of the carbon nanostructure-SA damage threshold is one goal for future research in this field.

As discussed in section 5.6, Carbon nanostructure-SA mode-locked lasers may need cavity modification, *e.g.*, by smaller radii of curvature of the folding mirrors (M_3 and M_4 in figure 5.6) to obtain a more stable laser operation with decreased tendency to multi-pulsing (*cp.* section 5.6). With tighter focusing, however, the before mentioned damage threshold of the polymer matrix represents the limiting parameter. For this reason, the direct and permanent transfer of SWCNTs on a glass substrate would be a very attractive means to overcome this issue.

An intriguing feature for SWCNT-SAs may be the variation of their absorption due to the inherent polarization dependence of the SWCNT absorption. Light polarized perpendicular to the tube is hardly absorbed, whereas polarization along the tube axis yields the maximum absorption per SWCNT. Samples incorporating aligned SWCNTs may be variable in their absorption by rotating the element. However, so far the directed growth has only been shown for individual SWCNTs and for arrays of multiwalled CNTs [214, 215]. Such a variable absorption may represent another laser parameter for optimization.

Consequently, future works may focus on different ways of nanostructure-SA implementation in the lasers under study. Using evanescent field absorption represents one way, which is currently paved for the generation of ultrashort pulses with elevated output power levels.

Due to the combination of usable nonlinearities of one single absorber covering a spectral range of more than one octave, and the design in transmission, the synchronization of two lasers with one single nanostructure-SA should be possible. For this purpose, the cavity beam paths need to cross in the position of the SA, and the optical cavity lengths have to be identical.

Abbreviations and symbols

ACF	autocorrelation function
AOM	acousto-optic modulator
AR	Auger recombination
cap-scattering	Carrier-acoustic phonon scattering
cc-scattering	Carrier-carrier scattering
cop-scattering	Carrier-optical phonon scattering
CR	Coulomb renormalization
cw	continous wave
DOS	density of states
double tungstate	DT
FROG	frequency resolved optical gating
FWHM	full width at half maximum
GD	group delay
GDD	group delay dispersion
GVD	group velocity dispersion
HEM	heat exchanger method
HipCO	high pressure carbon monoxide assisted
HWHM	half width half maximum
IE	Impact excitation
IE	impact excitation
lhs	left-hand side
NIR	near-infrared
NLT	nonlinear transmission
OC	output coupler
OPO	optical parametric oscillator
QML	Q-switched mode-locking
RBM	radial breathing mode
RF	radio frequency
rhs	right-hand side
SA	Saturable absorber

SHG ..... second harmonic generation
SPM ..... self phase modulation
SVEA ..... slowly varying envelope approximation
SWCNT ..... single-walled carbon nanotube
SWCNTs ..... Single-walled carbon nanotubes
TBP ..... time-bandwidth-product
TOD ..... third order dispersion
TPA ..... Two photon absorption
TPA ..... two photon absorption
ttt-distance ..... tip-to-tip distance
UV ..... ultraviolet
vHs ..... van Hove singularity
vHs ..... van Hove singularity
YAG ..... yttrium aluminium garnet

List of figures

List of Tables

Bibliography

[1] P. Tzankov, O. Steinkellner, J. Zheng, M. Mero, W. Freyer, A. Husakou, I. Babushkin, J. Herrmann, and F. Noack. High-power fifth-harmonic generation of femtosecond pulses in the vacuum ultraviolet using a ti:sapphire laser. *Opt. Express*, 15(10):6389–6395, 2007.

[2] T. Bartel, P. Gaal, K. Reimann, M. Woerner, and T. Elsaesser. Generation of single-cycle thz transients with high electric-field amplitudes. *Opt. Lett.*, 30(20):2805–2807, 2005.

[3] U. Morgner, F. X. Kärtner, S. H. Cho, Y. Chen, H. A. Haus, J. G. Fujimoto, E. P. Ippen, V. Scheuer, G. Angelow, and T. Tschudi. Sub-two-cycle pulses from a kerr-lens mode-locked ti:sapphire laser. *Opt. Lett.*, 24(6):411–413, 1999.

[4] S. Koke, C. Grebing, H. Frei, A. Anderson, A. Assion, and G. Steinmeyer. Direct frequency comb synthesis with arbitrary offset and shot-noise-limited phase noise. *Nature Photonics*, 4:462–465, 2010.

[5] J C Livas, J I Thorpe, K Numata, S Mitryk, G Mueller, and V Wand. Frequency-tunable pre-stabilized lasers for lisa via sideband locking. *Classical and Quantum Gravity*, 26(9):094016, 2009.

[6] J. D. Zuegel, S. Borneis, C. Barty, B. Legarrec, C. Danson, N. Miyanaga, P. K. Rambo, C. Leblanc, T. J. Kessler, A. W. Schmid, L. J. Waxer, J. H. Kelly, B. Kruschwitz, R. Jungquist, E. Moses, J. Britten, I. Jovanovic, J. Dawson, and N. Blanchot. Laser challenges for fast ignition. *Fusion Science & Technology*, 49(3):453–482, 2006.

[7] Jian C., J. W. Sickler, H. Byun, E. P. Ippen, S. Jiang, and F. X. Kärtner. Fundamentally mode-locked 3 ghz femtosecond erbium fiber laser. In *Proceedings of the 16th International Conference, Palazzo dei Congressi Stresa, Italy*, pages 732–734. Springer Berlin / Heidelberg, 2008.

[8] U. Keller, K.J. Weingarten, F.X. Kartner, D. Kopf, B.Braun, I.D. Jung, R. Fluck, C. Honninger, N. Matuschek, and J. J. Aus der Au. Semiconductor saturable absorber mirrors (sesam's) for femtosecond to nanosecond pulse generation in solid-state lasers. *IEEE Journal of Selected Topics in Quantum Electronics*, (3):435–453.

[9] S. Y. Set, H. Yaguchi, Y. Tanaka, and M.Jablonski. Laser mode locking using a saturable absorber incorporating carbon nanotubes. *J. Lightwave Technol.*, 22(1):51, 2004.

[10] T. Hasan, Z. Sun, F. Wang, F. Bonaccorso, P.H. Tan, A.G. Rozhin, and A.C. Ferrari. Nanotube polymer composites for ultrafast photonics. *Advanced Materials*, 21(38-39):3874–3899, 2009.

[11] T. Hakulinen, A. Kaskela, B. Aitchison, D. P. Brown, A. G. Nasibulin, E. I. Kauppinen, O. G. Okhotnikov, et al. Carbon nanotube films for ultrafast broadband technology. *Optics express*, 17(4):2358–2363, 2009.

[12] H. W. Kroto, J.R. Heath, S. C. O'Brien, R. F. Curl, and R. E. Smalley. C_{60}buckminsterfullerene. *Nature*, 1985.

[13] S. Iijima and T. Ichihashi. Single-shell carbon nanotubes of 1-nm diameter. *Nature*, 1993.

[14] P.R. Wallace. The band theory of graphite. *Physical Review*, 1947.

[15] J.W. McClure. Diamagnetism of graphite. *Physical Review*, 1956.

[16] J.C. Slonczewski and P.R. Weiss. Band structure of graphite. *Physical Review*, 1958.

[17] F. Bonaccorso, Z. Sun, T. Hasan, and A. C. Ferrari. Graphene photonics and optoelectronics. *Nature Photonics*, 2010.

[18] T. Stauber, N. M. R. Peres, and A. K. Geim. Optical conductivity of graphene in the visible region of the spectrum. *Phys. Rev. B*, 78:085432, 2008.

[19] J. Sun, M. T. Cole, N. Lindvall, K. B. K. Teo, and A. Yurgens. Noncatalytic chemical vapor deposition of graphene on high-temperature substrates for transparent electrodes. *Applied Physics Letters*, 100(2):022102, 2012.

[20] L. A. Falkovsky and S. S. Pershoguba. Optical far-infrared properties of a graphene monolayer and multilayer. *Phys. Rev. B*, 76:153410, 2007.

[21] K.S. Novoselov, A.K. Geim, S.V. Morozov, D. Jiang, M.I. Katsnelson, I.V. Grigorieva, S.V. Dubonos, and A.A. Firsov. Two-dimensional gas of massless dirac fermions in graphene. *Nature*, 2005.

[22] Y. Zhang, J.W. Tan, H.L. Stormer, and P. Kim. Experimental observation of the quantum hall effect in Berry's phase in graphene. *Nature*, 2005.

[23] K.S. Novoselov, A.K. Geim, S.V. Morozov, D. Jiang, Y. Zhang, S.V. Dubonos, I.V. Gregorieva, and A. A. Firsov. Electric field effect in atomically thin carbon films. *Science*, 2004.

[24] K.S. Novoselov, D. Jiange, F. Schedin, T.J. Booth, V.V. Khotkevich, S.V. Morozov, and A.K. Geim. Two-dimensional atomic crystal. *Proceedings of the National Academy of Sciences*, 2005.

[25] A.K. Geim and K.S. Novoselov. The rise of graphene. *Nature Materials*, 2007.

[26] M. S. Dresselhaus and G. Dresselhaus. *Carbon Nanotubes Synthesis, Structure, Properties, and Applications*. Springer Berlin Heidelberg, 2001.

[27] R. Saito, G. Dresselhaus, and M. S. Dresselhaus. Trigonal warping effect of carbon nanotubes. *Phys. Rev. B*, 61:2981–2990, 2000.

[28] J. P. Hobson and W. A. Nierenberg. The statistics of a two-dimensional, hexagonal net. *Phys. Rev.*, 89:662–662, 1953.

[29] V. P. Gusynin, S. G. Sharapov, and J. P. Carbotte. Ac Conductivity of Graphene:. from Tight-Binding Model to 2 + 1-DIMENSIONAL Quantum Electrodynamics. *International Journal of Modern Physics B*, 21:4611–4658, 2007.

[30] A. H. Castro Neto, F. Guinea, N. M. R. Peres, K. S. Novoselov, and A. K. Geim. The electronic properties of graphene. *Reviews of Modern Physics*, 81:109–162, 2009.

[31] Léon Van Hove. The occurrence of singularities in the elastic frequency distribution of a crystal. *Phys. Rev.*, 89:1189–1193, 1953.

[32] A. Zhou and W. Sheng. Van hove singularities in graphene nanoflakes. *Journal of Applied Physics*, 112(9):094313, 2012.

[33] L. Hao and L. Sheng. Optical conductivity of multilayer graphene. *Solid State Communications*, 149(43/44):1962 – 1966, 2009.

[34] Z. Sun, Z. Yan, E. Yao, J.and Beitler, Y. Zhu, and J. M. Tour. Growth of graphene from solid carbon sources. *Nature*, 468:549–552, 2010.

[35] Dan Li, Marc B. Muller, Scott Gilje, Richard B. Kaner, and Gordon G. Wallace. Processable aqueous dispersions of graphene nanosheets. *Nature Nanotechnology*, 3:101–105, 2008.

[36] L. Yang, J. Deslippe, C.-H. Park, M. L. Cohen, and S. G. Louie. Excitonic effects on the optical response of graphene and bilayer graphene. *Phys. Rev. Lett.*, 103:186802, 2009.

[37] D.-H. Chae, T. Utikal, S. Weisenburger, H. Giessen, K. v. Klitzing, M. Lippitz, and J. Smet. Excitonic fano resonance in free-standing graphene. *Nano Letters*, 11(3):1379–1382, 2011.

[38] U. Fano. Effects of configuration interaction on intensities and phase shifts. *Phys. Rev.*, 124:1866–1878, 1961.

[39] A. Bianconi. Ugo fano and shape resonances. *X-RAY AND INNER-SHELL PROCESSES. AIP Conference Proceedings*, 652:13–18, 2003.

[40] L.M. Malard, M.A. Pimenta, G. Dresselhaus, and M.S. Dresselhaus. Raman spectroscopy in graphene. *Physics Reports*, 473(5?6):51 – 87, 2009.

[41] F. Tuinstra and J. L. Koenig. Raman spectrum of graphite. *The Journal of Chemical Physics*, 53(3), 1970.

[42] D. Graf, F. Molitor, K. Ensslin, C. Stampfer, A. Jungen, C. Hierold, and L. Wirtz. Spatially resolved raman spectroscopy of single- and few-layer graphene. *Nano Letters*, 7(2):238–242, 2007.

[43] Y. Hao, Y. Wang, L. Wang, Z. Ni, Z. Wang, R. Wang, C. K. Koo, Z. Shen, and J. T. L. Thong. Probing layer number and stacking order of few-layer graphene by raman spectroscopy. *Small*, 6(2):195–200, 2010.

[44] I. H.Baek, H. W. Lee, S. Bae, B. H. Hong, Y. H. Ahn, D.-I. Yeom, and F. Rotermund. Efficient mode-locking of sub-70-fs ti:sapphire laser by graphene saturable absorber. *Applied Physics Express*, 5(3):032701, 2012.

[45] J.-C. Charlier, X. Blase, and S. Roche. Electronic and transport properties of nanotubes. *Rev. Mod. Phys.*, 79:677–732, 2007.

[46] C. L. Kane and E. J. Mele. Size, shape, and low energy electronic structure of carbon nanotubes. *Phys. Rev. Lett.*, 78:1932–1935, 1997.

[47] J. W. Mintmire and C. T. White. Universal density of states for carbon nanotubes. *Phys. Rev. Lett.*, 81:2506–2509, 1998.

[48] M P Anantram and F Léonard. Physics of carbon nanotube electronic devices. *Reports on Progress in Physics*, 69(3):507, 2006.

[49] S.-i. Hamada, N.and Sawada and A. Oshiyama. New one-dimensional conductors: Graphitic microtubules. *Phys. Rev. Lett.*, 68:1579–1581, 1992.

[50] R. Saito, M. Fujita, G. Dresselhaus, and M. S Dresselhaus. Electronic structure of chiral graphene tubules. *Applied Physics Letters*, 60(18):2204–2206, 1992.

[51] J.-C. Charlier and Ph. Lambin. Electronic structure of carbon nanotubes with chiral symmetry. *Phys. Rev. B*, 57:R15037–R15039, 1998.

[52] J. W. G. Wildöer, Ll C. Venema, A. G. Rinzler, R. E. Smalley, and C. Dekker. Electronic structure of atomically resolved carbon nanotubes. *Nature*, 1998.

[53] T. W Odom, J. L. Huang, P. Kim, and C. M. Lieber. Atomic structure and electronic properties of single-walled carbon nanotubes. *Nature*, 391:62–64, 1998.

[54] A.M. Rao, E. Richter, S. Bandow, B. Chase, P. C. Eklund, K. A. Williams, S. Fang, K. R. Subbaswamy, M. Menon, A. Thess, R. E. Smalley, G. Dresselhaus, and M. S. Dresselhaus. Diameter-selective raman scattering from vibrational modes in carbon nanotubes. *Science*, 1997.

[55] H. Kataura, Y. Kumazawa, Y. Maniwa, I. Umezu, S. Suzuki, Y. Ohtsuka, and Y. Achiba. Optical properties of single-wall carbon nanotubes. *Synthetic Metals*, 103:2555 – 2558, 1999. International Conference on Science and Technology of Synthetic Metals.

[56] J. W. Mintmire, B. I. Dunlap, and C. T. White. Are fullerene tubules metallic? *Phys. Rev. Lett.*, 68:631–634, 1992.

[57] C. L. Kane and E. J. Mele. Ratio problem in single carbon nanotube fluorescence spectroscopy. *Phys. Rev. Lett.*, 90:207401, 2003.

[58] E. Chang, G. Bussi, A. Ruini, and E. Molinari. Excitons in carbon nanotubes: An *Ab Initio* symmetry-based approach. *Phys. Rev. Lett.*, 92:196401, 2004.

[59] C. D. Spataru, S. Ismail-Beigi, L. X. Benedict, and S. G. Louie. Excitonic effects and optical spectra of single-walled carbon nanotubes. *Phys. Rev. Lett.*, 92:077402, 2004.

[60] V. Perebeinos, J. Tersoff, and P. Avouris. Scaling of excitons in carbon nanotubes. *Phys. Rev. Lett.*, 92:257402, 2004.

[61] F. Wang, G. Dukovic, L.E. Brus, and T. F. Heinz. The optical resonances in carbon nanotubes arise from excitons. *Science*, 308(5723):838–841, 2005.

[62] J. Maultzsch, R. Pomraenke, S. Reich, E. Chang, D. Prezzi, A. Ruini, E. Molinari, M. S. Strano, C. Thomsen, and C. Lienau. Exciton binding energies in carbon nanotubes from two-photon photoluminescence. *Phys. Rev. B*, 72:241402, 2005.

[63] J. Maultzsch, R. Pomraenke, S. Reich, E. Chang, D. Prezzi, A. Ruini, E. Molinari, M. S. Strano, C. Thomsen, and C. Lienau. Excitons in carbon nanotubes. *physica status solidi (b)*, 243(13):3204–3208, 2006.

[64] T. Ogawa and T. Takagahara. Optical absorption and sommerfeld factors of one-dimensional semiconductors: An exact treatment of excitonic effects. *Phys. Rev. B*, 44:8138–8156, 1991.

[65] F. Rossi and E. Molinari. Coulomb-induced suppression of band-edge singularities in the optical spectra of realistic quantum-wire structures. *Phys. Rev. Lett.*, 76:3642–3645, 1996.

[66] M. Fox. *Optische Eigenschaften von Festkörpern, [Übers. Karen Lippert].* München : Oldenbourg, 2012.

[67] J. M. Marulanda and A. Srivastava. Carrier density and effective mass calculations in carbon nanotubes. *physica status solidi (b)*, 245(11):2558–2562, 2008.

[68] M. S. Dresselhaus, G. Dresselhaus, R. Saito, and A. Jorio. Exciton photophysics of carbon nanotubes. *Annual Review of Physical Chemistry*, 58(1):719–747, 2007. PMID: 17201684.

[69] P. T. Araujo, A. Jorio, M. S. Dresselhaus, K. Sato, and R. Saito. Diameter dependence of the dielectric constant for the excitonic transition energy of single-wall carbon nanotubes. *Phys. Rev. Lett.*, 103:146802, 2009.

[70] A. Jorio, G. Dresselhaus, and M. S. Dresselhaus. *Carbon Nanotubes, Advanced Topics in the Synthesis, Structure, Properties, and Applications.* Springer Berlin Heidelberg, 2008.

[71] E. Malic and A. Knorr. *Graphene and Carbon Nanotubes.* Wiley-VCH, Berlin, 2013.

[72] R. B. Weisman and S. M. Bachilo. Dependence of optical transition energies on structure for single-walled carbon nanotubes in aqueous suspension:? an empirical kataura plot. *Nano Letters*, 3(9):1235–1238, 2003.

[73] M. J. O'Connell, S. M. Bachilo, C. B. Huffman, V. C. Moore, M. S. Strano, E. H. Haroz, K. L. Rialon, P. J. Boul, W. H. Noon, C. Kittrell, J. Ma, R. H. Hauge, R. B. Weisman, and R. E. Smalley. Band gap fluorescence from individual single-walled carbon nanotubes. *Science*, 297(5581):593–596, 2002.

[74] S. Reich, C. Thomsen, and P. Ordejón. Electronic band structure of isolated and bundled carbon nanotubes. *Phys. Rev. B*, 65:155411, 2002.

[75] W. B. Cho, J. H. Yim, S. Y. Choi, S. Lee, A. Schmidt, G. Steinmeyer, U. Griebner, V. Petrov, D.-I. Yeom, K. Kim, and F. Rotermund. Boosting the non linear optical response of carbon nanotube saturable absorbers for broadband mode-locking of bulk lasers. *Advanced Functional Materials*, 20(12):1937–1943, 2010.

[76] P. Nikolaev, M. J Bronikowski, R. K. Bradley, Frank R., D. T. Colbert, K.A. Smith, and R. E Smalley. Gas-phase catalytic growth of single-walled carbon nanotubes from carbon monoxide. *Chemical Physics Letters*, 313(1?2):91 – 97, 1999.

[77] M.S. Dresselhaus, G. Dresselhaus, R. Saito, and A. Jorio. Raman spectroscopy of carbon nanotubes. *Physics Reports*, 409(2):47 – 99, 2005.

[78] M. Zheng, A. Jagota, M. S. Strano, A. P. Santos, P. Barone, S. G. Chou, B. A. Diner, M. S. Dresselhaus, R. S. Mclean, G. B. Onoa, G. G. Samsonidze, E. D. Semke, M. Usrey, and D. J. Walls. Structure-based carbon nanotube sorting by sequence-dependent DNA assembly. *Science*, 302(5650):1545–1548, 2003.

[79] X. Tu, S. Manohar, A. Jagota, and M. Zheng. DNA sequence motifs for structure-specific recognition and separation of carbon nanotubes. *Nature*, 460(7252):250–253, 2009.

[80] S. Y. Choi, W. B. Cho, D.-I. Yeom, K. Kim, F. Rotermund, J.-H. Kim, K.-J. Yee, A. Schmidt, G. Steinmeyer, B. Wolter, V. Petrov, and U. Griebner. Octave spanning ultra-broadband carbon nanotube saturable absorber for bulk solid-state lasers. In *Advanced Solid-State Photonics*, page AWB4. Optical Society of America, 2011.

[81] F. X. Kärtner and U. Keller. Stabilization of solitonlike pulses with a slow saturable absorber. *Optics Letters*, 20(1):16–18, 1995.

[82] J. Shah. *Hot carriers in semiconductor nanostructures: Physics and applications*. Elsevier, 1992.

[83] M. Breusing, S. Kuehn, T. Winzer, E. Malić, F. Milde, N. Severin, J. P. Rabe, C. Ropers, A. Knorr, and T. Elsaesser. Ultrafast nonequilibrium carrier dynamics in a single graphene layer. *Phys. Rev. B*, 83:153410, 2011.

[84] M. Breusing, C. Ropers, and T. Elsaesser. Ultrafast Carrier Dynamics in Graphite. *Phys. Rev. Lett.*, 102:086809, 2009.

[85] Ultrafast relaxation dynamics via acoustic phonons in carbon nanotubes.

[86] G. N. Ostojic, S. Zaric, J. Kono, M. S. Strano, V. C. Moore, R. H. Hauge, and R. E. Smalley. Interband recombination dynamics in resonantly excited single-walled carbon nanotubes. *Phys. Rev. Lett.*, 92:117402, 2004.

[87] M. Haiml, R. Grange, and U. Keller. Optical characterization of semiconductor saturable absorbers. *Applied Physics B: Lasers and Optics*, 79:331–339, 2004. 10.1007/s00340-004-1535-1.

[88] C. Hönninger, R. Paschotta, F. Morier-Genoud, M. Moser, and U. Keller. Q-switching stability limits of continuous-wave passive mode locking. *J. Opt. Soc. Am. B*, 16(1):46–56, 1999.

[89] E. R. Thoen, E. M. Koontz, M. Joschko, P. Langlois, T. R. Schibli, F. X. Kärtner, E. P. Ippen, and L. A. Kolodziejski. Two-photon absorption in semiconductor saturable absorber mirrors. *Applied Physics Letters*, 74(26):3927–3929, 1999.

[90] . H. Baek, S. Y. Choi, H. W. Lee, W. B. Cho, V. Petrov, A. Agnesi, V. Pasiskevicius, D.-I. Yeom, Ki. Kim, and F. Rotermund. Single-walled carbon nanotube saturable absorber assisted high-power mode-locking of a ti:sapphire laser. *Opt. Express*, 19(8):7833–7838, 2011.

[91] A. Schmidt, S. Rivier, G. Steinmeyer, J. H. Yim, W. B. Cho, S. Lee, F. Rotermund, M. C. Pujol, X. Mateos, M. Aguiló, F. Díaz, V. Petrov, and U. Griebner. Passive mode locking of Yb:KLuW using a single-walled carbon nanotube saturable absorber. *Opt. Lett.*, 33(7):729–731, 2008.

[92] J. Eichler and H. J. Eichler. *Laser - Bauformen, Strahlführung, Anwendungen; 5. Auflage*. Springer Berlin Heidelberg, 2003.

[93] J. H. Yim, W. B. Cho, S. Lee, Y. H. Ahn, K. Kim, H. Lim, G. Steinmeyer, V. Petrov, U. Griebner, and F. Rotermund. Fabrication and characterization of ultrafast carbon nanotube saturable absorbers for solid-state laser mode locking near 1 μm. *Applied Physics Letters*, 93(16):161106, 2008.

[94] K. H. Fong, K. Kikuchi, C. S. Goh, S. Y. Set, R.Grange, M. Haiml, A. Schlatter, and U. Keller. Solid-state er:yb:glass laser mode-locked by using single-wall carbon nanotube thin film. *Opt. Lett.*, 32(1):38–40, 2007.

[95] T. Hertel, R. Fasel, and G. Moos. Charge-carrier dynamics in single-wall carbon nanotube bundles: a time-domain study. *Applied Physics A*, 75(4):449–465, 2002.

[96] A. Vainionpää, S. Suomalainen, A. Isomäki, O. Tengvall, M. Pessa, and O.G. Okhotnikov. Semiconductor saturable absorber mirror with wavelength tailored distributed bragg reflector. *Journal of Crystal Growth*, 278(1?4):751 – 755, 2005. 13th International Conference on Molecular Beam Epitaxy.

[97] S. Gupta, M. Y. Frankel, J. A. Valdmanis, J. F. Whitaker, G. A. Mourou, F. W. Smith, and A. R. Calawa. Subpicosecond carrier lifetime in gaas grown by molecular beam epitaxy at low temperatures. *Applied Physics Letters*, 59(25):3276–3278, 1991.

[98] Ursula Keller, Kurt J Weingarten, Franz X Kartner, Daniel Kopf, Bernd Braun, Isabella D Jung, Regula Fluck, Clements Honninger, Nicolai Matuschek, and J Aus der Au. Semiconductor saturable absorber mirrors (sesam's) for femtosecond to nanosecond pulse generation in solid-state lasers. *Selected Topics in Quantum Electronics, IEEE Journal of*, 2(3):435–453, 1996.

[99] M. Moenster, U. Griebner, W. Richter, and G. Steinmeyer. Resonant saturable absorber mirrors for dispersion control in ultrafast lasers. *Quantum Electronics, IEEE Journal of*, 43(2):174–181, 2007.

[100] W. B. Cho, J. W. Kim, H. W. Lee, S. Bae, B. H. Hong, S. Y. Choi, In H. Baek, K. Kim, D.-I. Yeom, and F. Rotermund. High-quality, large-area monolayer graphene for efficient bulk laser mode-locking near 1.25μm. *Opt. Lett.*, 36(20):4089–4091, 2011.

[101] Feng Wang, Yuanbo Zhang, Chuanshan Tian, Caglar Girit, Alex Zettl, Michael Crommie, and Y. Ron Shen. Gate-variable optical transitions in graphene. *Science*, 320(5873):206–209, 2008.

[102] S. Kivistö, T. Hakulinen, A. Kaskela, B. Aitchison, D. P. Brown, A.G. Nasibulin, E. I. Kauppinen, A. Härkönen, and O. G. Okhotnikov. Carbon nanotube films for ultrafast broadband technology. *Opt. Express*, 17(4):2358–2363, 2009.

[103] I. H. Baek, S. Y.Choi, H. W. Lee, W. B. Cho, V. Petrov, A. Agnesi, V. Pasiskevicius, D.-I. Yeom, K. Kim, and F. Rotermund. Single-walled carbon nanotube saturable absorber assisted high-power mode-locking of a Ti:sapphire laser. *Opt. Express*, 19(8):7833–7838, 2011.

[104] M.N. Cizmeciyan, J.W. Kim, S. Bae, B.H. Hong, F. Rotermund, and A. Sennaroglu. Graphene mode-locked femtosecond cr: Znse laser at 2500 nm. *Optics letters*, 38(3):341–343, 2013.

[105] C. Chudoba, J.G. Fujimoto, E.P. Ippen, H. A. Haus, U. Morgner, F.X. Kärtner, V. Scheuer, G. Angelow, and T. Tschudi. All-solid-state cr: forsterite laser generating 14-fs pulses at 1.3 μm. *Optics letters*, 26(5):292–294, 2001.

[106] K. Petermann, L. Fornasiero, E. Mix, and V. Peters. High melting sesquioxides: crystal growth, spectroscopy, and laser experiments. *Optical Materials*, 19(1):67–71, 2002.

[107] R. Peters. *Ytterbium-dotierte Sesquioxide als hocheffiziente Lasermaterialien*. Shaker, 2009.

[108] V. Petrov, M. Cinta Pujol, X. Mateos, Ò. Silvestre, S. Rivier, M. Aguiló, R.M. Solé, J. Liu, U. Griebner, and F. Díaz. Growth and properties of $KLu(WO_4)_2$, and novel ytterbium and thulium lasers based on this monoclinic crystalline host. *Laser & Photonics Reviews*, 1(2):179–212, 2007.

[109] R Solé, V Nikolov, X Ruiz, Jna Gavaldà, X Solans, M Aguiló, and F Díaz. Growth of β-$KGd_{1-x}Nd_x$ $(WO_4)_2$ single crystals in $K_2W_2O_7$ solvents. *Journal of crystal growth*, 169(3):600–603, 1996.

[110] W. Beall Fowler and D. L. Dexter. Relation between absorption and emission probabilities in luminescent centers in ionic solids. *Phys. Rev.*, 128:2154–2165, 1962.

[111] D. E. McCumber. Einstein relations connecting broadband emission and absorption spectra. *Phys. Rev.*, 136:A954–A957, 1964.

[112] L. D. DeLoach, S.A. Payne, L.L. Chase, L. K. Smith, W. L. Kway, and W. F. Krupke. Evaluation of absorption and emission properties of yb3+ doped crystals for laser applications. *Quantum Electronics, IEEE Journal of*, 29(4):1179–1191, 1993.

[113] W. J. Miniscalco and R. S. Quimby. General procedure for the analysis of er^{3+} cross sections. *Opt. Lett.*, 16(4):258–260, 1991.

[114] L. D. DeLoach, S.A. Payne, L.L. Chase, L. K. Smith, W. L. Kway, and W. F. Krupke. Evaluation of absorption and emission properties of yb3+ doped crystals for laser applications. *Quantum Electronics, IEEE Journal of*, 29(4):1179–1191, 1993.

[115] S. J. Strickler and Robert A. Berg. Relationship between absorption intensity and fluorescence lifetime of molecules. *The Journal of Chemical Physics*, 37(4), 1962.

[116] B. E. A. Saleh and M. C. Teich. *Fundamentals of Photonics*. John Wiley & Sons, Hoboken, New Jersey, second edition edition, 2007.

[117] P. Agrawal. *Nonlinear Fiber Optics*. Academic Press San Diego, 2001.

[118] R. Trebino. *Frequency-Resolved Optical G ating: The Measurement of ultrashort Laser Pulses*. Kluwer academic publishers, 2000.

[119] F. Gires and P. Tournois. Interferometre utilisable pour la compression d'impulsions lumineuses modulees en frequence. *C. R. Acad. Sci. Paris*, (258):6112, 1964.

[120] R. Szipöcs, C. Spielmann, F. Krausz, and K. Ferencz. Chirped multilayer coatings for broadband dispersion control in femtosecond lasers. *Opt. Lett.*, 19(3):201–203, 1994.

[121] R. L. Fork, O. E. Martinez, and J. P. Gordon. Negative dispersion using pairs of prisms. *Opt. Lett.*, 9(5):150–152, 1984.

[122] R. E. Sherriff. Analytic expressions for group-delay dispersion and cubic dispersion in arbitrary prism sequences. *J. Opt. Soc. Am. B*, 15(3):1224–1230, 1998.

[123] M. G. Littman and H. J. Metcalf. Spectrally narrow pulsed dye laser without beam expander. *Appl. Opt.*, 17(14):2224–2227, 1978.

[124] J.-C. Diels and W. Rudolph. *Ultrashort Laser Pulse Phenomena*. Academic Press San Diego, second edition edition, 2006.

[125] R. R. Alfano and S. L. Shapiro. Observation of self-phase modulation and small-scale filaments in crystals and glasses. *Phys. Rev. Lett.*, 24:592–594, 1970.

[126] C. Lin and R. H. Stolen. New nanosecond continuum for excited?state spectroscopy. *Applied Physics Letters*, 28(4), 1976.

[127] *The elements of nonlinear optics (Reprint ed.)*. Cambridge University Press, 1991.

[128] Guido H.M. van Tartwijk and Govind P Agrawal. Laser instabilities: a modern perspective. *Progress in Quantum Electronics*, 22(2):43 – 122, 1998.

[129] Hermann A. Haus. Theory of mode locking with a fast saturable absorber. *Journal of Applied Physics*, 46(7):3049–3058, 1975.

[130] H. A. Haus, J. G. Fujimoto, and E. P. Ippen. Structures for additive pulse mode locking. *J. Opt. Soc. Am. B*, 8(10):2068–2076, 1991.

[131] H. A. Haus. Mode-locking of lasers. *Selected Topics in Quantum Electronics, IEEE Journal of*, 6(6):1173–1185, 2000.

[132] C. S. Gardner, J. M. Greene, M. D. Kruskal, and R. M. Miura. Method for solving the korteweg-devries equation. *Phys. Rev. Lett.*, 19:1095–1097, 1967.

[133] C. S. Gardner, J. M. Greene, M. D. Kruskal, and R. M. Miura. Korteweg-devries equation and generalizations. vi. methods for exact solution. *Communications on Pure and Applied Mathematics*, 27(1):97–133, 1974.

[134] F. X. Kärtner, J. Aus der Au, and U. Keller. Mode-locking with slow and fast saturable absorbers - what's the difference? *IEEE Journal of Selected Topics in Quantum Electronics (invited paper)*, 4:159–168, 1998.

[135] V. L. Kalashnikov, A. Fernández, and A. Apolonski. High-order dispersion in chirped-pulse oscillators. *Opt. Express*, 16(6):4206–4216, 2008.

[136] F. X. Kärtner, J. Aus der Au, and U. Keller. Mode-locking with slow and fast saturable absorbers-what's the difference? *IEEE Journal of Selected Topics in Quantum Electronics*, 4(2):159 – 168, 1998.

[137] J.-C. M. Diels, J. J. Fontaine, .n C. McMichael, and F. Simoni. Control and measurement of ultrashort pulse shapes (in amplitude and phase) with femtosecond accuracy. *Appl. Opt.*, 24(9):1270–1282, 1985.

[138] A. E. Siegman. *Lasers*. University Science Books, 1986.

[139] N. N. Akhmediev, A. Ankiewicz, M. J. Lederer, and B. Luther-Davies. Ultrashort pulses generated by mode-locked lasers with either a slow or a fast saturable-absorber response. *Opt. Lett.*, 23(4):280–282, 1998.

[140] J. Aus der Au, D. Kopf, F. Morier-Genoud, M. Moser, and U. Keller. 60-fs pulses from a diode-pumped nd:glass laser. *Opt. Lett.*, 22(5):307–309, 1997.

[141] D. V. Khudyakov, A. S. Lobach, and V. A. Nadtochenko. Passive mode locking in a Ti:sapphire laser using a single-walled carbon nanotube saturable absorber at a wavelength of 810 nm. *Opt. Lett.*, 35(16):2675–2677, 2010.

[142] T. Schibli, K. Minoshima, H. Kataura, E. Itoga, N. Minami, S. Kazaoui, K. Miyashita, M. Tokumoto, and Y. Sakakibara. Ultrashort pulse-generation by saturable absorber mirrors based on polymer-embedded carbon nanotubes. *Opt. Express*, 13(20):8025–8031, 2005.

[143] A. Schmidt, S. Rivier, W. B. Cho, J. H. Yim, S. Y. Choi, S. Lee, F. Rotermund, D. Rytz, G. Steinmeyer, V. Petrov, and U. Griebner. Sub-100 fs single-walled carbon nanotube saturable absorber mode-locked Yb-laser operation near 1 μm. *Opt. Express*, 17(22):20109–20116, 2009.

[144] A. Agnesi, A. Greborio, F. Pirzio, G. Reali, S. Y. Choi, F. Rotermund, U. Griebner, and V. Petrov. 99 fs Nd:Glass Laser Mode-Locked with Carbon Nanotube Saturable Absorber Mirror. *Applied Physics Express*, 3(11):112702, 2010.

[145] A. Agnesi, L. Carrà, F. Pirzio, G. Reali, A. Toncelli, M. Tonelli, S. Y. Choi, F. Rotermund, U. Griebner, and V. Petrov. Diode-pumped Nd:BaY2F8 picosecond laser mode-locked with carbon nanotube saturable absorbers. *J. Opt. Soc. Am. B*, 27(12):2739–2742, 2010.

[146] W. D. Tan, F. Chen, R. J. Knize, J. Zhang, D. Tang, and L.-J. Li. Passive mode locking of ceramic Nd: YAG using (7, 5) semiconducting single walled carbon nanotubes. *Optical Materials*, 33(5):679 – 683, 2011. ¡ce:title¿5th Laser Ceramics Symposium: International Symposium on TRANSPARENT CERAMICS FOR PHOTONIC APPLICATIONS (LCS?09) Bilbao, Spain, December 9-11, 2009¡/ce:title¿ ¡ce:subtitle¿5th- LCS 2009¡/ce:subtitle¿.

[147] H.-R. Chen, Y.-G. Wang, C.-Y. Tsai, K.-H. Lin, T.-Y. Chang, J. Tang, and W.-F. Hsieh. High-power, passively mode-locked Nd:$GdVO_4$laser using single-walled carbon nanotubes as saturable absorber. *Opt. Lett.*, 36(7):1284–1286, 2011.

[148] K. Yang, S. Zhao, G. Zhang, K. Cheng, B. Zhao, J. Xu, J. He, and Y. Wang. Diode-pumped passively mode-locked Nd:$Lu_{0.15}Y_{0.85}VO_4$ laser with a single-walled carbon nanotube saturable absorber. *Optics Communications*, 285(2):158 – 161, 2012.

[149] C.-C. Liu, Y.-G. Wang, J. Liu, L.-H. Zheng, L.-B. Su, and J. Xu. Ultrafast laser performance of Yb^{3+}: Sc_2SiO_5 crystal with a single-walled carbon nanotube absorbers. *Optics Communications*, 285(6):1352 – 1355, 2012.

[150] W. B. Cho, J. H. Yim, S. Y. Choi, S. Lee, U. Griebner, V.-Petrov, and F. Rotermund. Mode-locked self-starting Cr:forsterite laser using a single-

walled carbon nanotube saturable absorber. *Opt. Lett.*, 33(21):2449–2451, 2008.

[151] W.-B. Cho, S.-Y. Choi, J.-W. Kim, D.-I. Yeom, K.-H. Kim, F. Rotermund, and H.-J. Lim. Solid-state laser mode-locking near 1.25 μm employing a carbon nanotube saturable absorber mirror. *Journal of the Optical Society of Korea*, 15(1):56–60, 2011.

[152] H. Iliev, I. Buchvarov, S. Choi, K. Kim, F. Rotermund, U. Griebner, and V. Petrov. Steady state mode-locking of a 1.34 μm Nd:YVO_4 laser using a single-walled carbon nanotube saturable absorber. *Applied Physics B: Lasers and Optics*, 106:1–4, 2012. 10.1007/s00340-011-4836-1.

[153] W. B. Cho, A. Schmidt, S. Y. Choi, V. Petrov, U. Griebner, G. Steinmeyer, S. Lee, D.-I. Yeom, and F. Rotermund. Mode locking of a Cr:YAG laser with carbon nanotubes. *Opt. Lett.*, 35(16):2669–2671, 2010.

[154] W. B. Cho, A. Schmidt, J. H. Yim, S. Y. Choi, S. Lee, F. Rotermund, U. Griebner, Günter Steinmeyer, V. Petrov, Xavier Mateos, Maria C. Pujol, Joan J. Carvajal, Magdalena Aguiló, and Francesc Díaz. Passive mode-locking of a Tm-doped bulk laser near 2 µmusing a carbon nanotube saturable absorber. *Opt. Express*, 17(13):11007–11012, 2009.

[155] A. Schmidt, P. Koopmann, G. Huber, P. Fuhrberg, S. Y. Choi, D.-I. Yeom, F. Rotermund, V. Petrov, and U. Griebner. 175 fs Tm:Lu_2o_3 laser at 2.07 µm mode-locked using single-walled carbon nanotubes. *Opt. Express*, 20(5):5313–5318, 2012.

[156] A. Schmidt, S. Y. Choi, D.-I. Yeom, F. Rotermund, Xavier Mateos, Martha Segura, Francesc Diaz, Valentin Petrov, and U. Griebner. Femtosecond pulses near 2 μm from a Tm:KLuW laser mode-locked by a single-walled carbon nanotube saturable absorber. *Applied Physics Express*, 5(9):092704, 2012.

[157] Q. Bao, H. Zhang, Y. Wang, Z. Ni, Y. Yan, Z. X. Shen, K. P. Loh, and D. Y. Tang. Atomic-layer graphene as a saturable absorber for ultrafast pulsed lasers. *Advanced Functional Materials*, 19(19):3077–3083, 2009.

[158] Z.i Sun, T. Hasan, F. Torrisi, D. Popa, F. Privitera, G.and Wang, F. Bonaccorso, D. M. Basko, and A. C. Ferrari. Graphene mode-locked ultrafast laser. *ACS Nano*, 4(2):803–810, 2010. PMID: 20099874.

[159] Y. M. Chang, H. Kim, J. H. Lee, and Y.-W. Song. Multilayered graphene efficiently formed by mechanical exfoliation for nonlinear saturable absorbers in fiber mode-locked lasers. *Applied Physics Letters*, 97(21):211102, 2010.

[160] J. Liu, Y.G. Wang, Z.S. Qu, L.H. Zheng, L.B. Su, and J. Xu. Graphene oxide absorber for 2 μm passive mode-locking Tm:$YAlO_3$ laser. *Laser Physics Letters*, 9(1):15–19, 2012.

[161] W. D. Tan, C. Y. Su, R. J. Knize, G. Q. Xie, L. J. Li, and D. Y. Tang. Mode locking of ceramic Nd:yttrium aluminum garnet with graphene as a saturable absorber. *Applied Physics Letters*, 96(3):031106, 2010.

[162] C.-C. LEE, T. R. SCHIBLI, G. ACOSTA, and J. S. BUNCH. Ultra-short optical pulse generation with single-layer graphene. *Journal of Nonlinear Optical Physics & Materials*, 19(04):767–771, 2010.

[163] J.-L. Xu, X.-L. Li, Y.-Z. Wu, X.-P. Hao, J.-L. He, and K.-J. Yang. Graphene saturable absorber mirror for ultra-fast-pulse solid-state laser. *Opt. Lett.*, 36(10):1948–1950, 2011.

[164] J.-L. Xu, X.-L. Li, J.-L. He, X.-P. Hao, Y.-Z. Wu, Y. Yang, and K.-J. Yang. Performance of large-area few-layer graphene saturable absorber in femtosecond bulk laser. *Applied Physics Letters*, 99(26):261107, 2011.

[165] J. Ma, G. Q. Xie, P. Lv, W. L. Gao, P. Yuan, L. J. Qian, H. H. Yu, H. J. Zhang, J. Y. Wang, and D. Y. Tang. Graphene mode-locked femtosecond laser at 2μm wavelength. *Opt. Lett.*, 37(11):2085–2087, 2012.

[166] E. Ugolotti, A. Schmidt, V. Petrov, Jun Wan Kim, D.-I. Yeom, F. Rotermund, Sukang Bae, Byung Hee Hong, A. Agnesi, Christian Fiebig, Götz Erbert, Xavier Mateos, Magdalena Aguiló, Francesc Diaz, and U. Griebner. Graphene mode-locked femtosecond Yb:KLuW laser. *Applied Physics Letters*, 101(16):161112, 2012.

[167] A. A. Lagatsky, Z. Sun, T. S. Kulmala, R. S. Sundaram, S. Milana, F. Torrisi, O. L. Antipov, Y. Lee, J. H. Ahn, C. T. A. Brown, W. Sibbett, and A. C. Ferrari. 2 μm solid-state laser mode-locked by single-layer graphene. *Applied Physics Letters*, 102(1):013113, 2013.

[168] S. D. Di Dio Cafiso, E. Ugolotti, A. Schmidt, V. Petrov, U. Griebner, A. Agnesi, W. B. Cho, B. H. Jung, F. Rotermund, S. Bae, B. H. Hong, G. Reali, and F. Pirzio. Sub-100-fs cr:yag laser mode-locked by monolayer graphene saturable absorber. *Opt. Lett.*, 38(10):1745–1747, 2013.

[169] CW Luo, YT Wang, FW Chen, HC Shih, and T Kobayashi. Eliminate coherence spike in reflection-type pump-probe measurements. *Optics express*, 17(14):11321–11327, 2009.

[170] F. Saas, G. Steinmeyer, U. Griebner, M. Zorn, and M. Weyers. Exciton resonance tuning for the generation of subpicosecond pulses from a mode-locked semiconductor disk laser. *Applied Physics Letters*, 89(14):–, 2006.

[171] S. Winnerl, M. Orlita, P. Plochocka, P. Kossacki, M. Potemski, T. Winzer, E. Malic, A. Knorr, M. Sprinkle, C. Berger, W. A. de Heer, H. Schneider, and M. Helm. Carrier relaxation in epitaxial graphene photoexcited near the dirac point. *Phys. Rev. Lett.*, 107:237401, 2011.

[172] K. Seibert, G. C. Cho, W. Kütt, H. Kurz, D. H. Reitze, J. I. Dadap, H. Ahn, M. C. Downer, and A. M. Malvezzi. Femtosecond carrier dynamics in graphite. *Phys. Rev. B*, 42:2842–2851, 1990.

[173] G. Moos, C. Gahl, R. Fasel, M. Wolf, and T. Hertel. Anisotropy of quasiparticle lifetimes and the role of disorder in graphite from ultrafast time-resolved photoemission spectroscopy. *Phys. Rev. Lett.*, 87:267402, 2001.

[174] C.-J. Chen, P. K. A. Wai, and C. R. Menyuk. Self-starting of passively modelocked lasers with fast saturable absorbers. *Opt. Lett.*, 20(4):350–352, 1995.

[175] S. Kivistö, T.Hakulinen, A.Kaskela, B. Aitchison, D. P. Brown, A. G. Nasibulin, E. I. Kauppinen, A. Härkönen, and O. G. Okhotnikov. Carbon nanotube films for ultrafast broadband technology. *Opt. Express*, 17(4):2358–2363, 2009.

[176] E. R. Thoen, E. M. Koontz, M. Joschko, P. Langlois, T. R. Schibli, F. X. Kärtner, E. P. Ippen, and L. A. Kolodziejski. Two-photon absorption in semiconductor saturable absorber mirrors. *Applied Physics Letters*, 74(26), 1999.

[177] A. Baum, P. J Scully, W. Perrie, M. Sharp, K. G. Watkins, D. Jones, R. Issac, and D. A. Jaroszynski. Nuv and nir femtosecond laser modification of pmma. *Proc. LPM2007*, 2007.

[178] D.M. Kane. Astigmatism compensation in off-axis laser resonators with two or more coupled foci. *Optics Communications*, 71(3?4):113 – 118, 1989.

[179] I. Amat-Roldán, I. Cormack, P. Loza-Alvarez, E. Gualda, and D. Artigas. Ultrashort pulse characterisation with shg collinear-frog. *Opt. Express*, 12(6):1169–1178, 2004.

[180] K. W. DeLong, Rick Trebino, and Daniel J. Kane. Comparison of ultrashort-pulse frequency-resolved-optical-gating traces for three common beam geometries. *J. Opt. Soc. Am. B*, 11(9):1595–1608, 1994.

[181] Z. Sun, T. Hasan, and A.C. Ferrari. Ultrafast lasers mode-locked by nanotubes and graphene. *Physica E: Low-dimensional Systems and Nanostructures*, 44(6):1082 – 1091, 2012. ¡ce:title¿The proceedings of the European Materials Research Symposium on Science and Technology of Nanotubes, Nanowires and Graphene¡/ce:title¿.

[182] J. W. Nicholson, R. S. Windeler, and D. J. DiGiovanni. Optically driven deposition of single-walled carbon-nanotube saturable absorbers on optical fiber end-faces. *Opt. Express*, 15(15):9176–9183, 2007.

[183] S.Y. Set, H. Yaguchi, Y.Tanaka, and M. Jablonski. Ultrafast fiber pulsed lasers incorporating carbon nanotubes. *IEEE Journal of Selected Topics in Quantum Electronics*, 10(1):137 – 146, 2004.

[184] Y.-W. Song, S. Yamashita, C. S. Goh, and S. Y. Set. Carbon nanotube mode lockers with enhanced nonlinearity via evanescent field interaction in d-shaped fibers. *Opt. Lett.*, 32(2):148–150, 2007.

[185] U. Griebner, S. Rivier, V. Petrov, M. Zorn, G. Erbert, M. Weyers, X. Mateos, M. Aguiló, J. Massons, and F. Díaz. Passively mode-locked Yb:KLu$(WO_4)_2$ oscillators. *Opt. Express*, 13(9):3465–3470, 2005.

[186] M. Schellhorn. A comparison of resonantly pumped ho:ylf and ho:llf lasers in cw and q-switched operation under identical pump conditions. *Applied Physics B*, 103(4):777–788, 2011.

[187] S. Banerjee, J. Koerner, M. Siebold, Q. Yang, K. Ertel, P. D. Mason, P. J. Phillips, M. Loeser, H. Zhang, S. Lu, J. Hein, U. Schramm, M. C. Kaluza, and J. L. Collier. Temperature dependent emission and absorption cross section of yb3+ doped yttrium lanthanum oxide (ylo) ceramic and its application in diode pumped amplifier. *Opt. Express*, 21(S4):A726–A734, 2013.

[188] H. Eilers, W.M. Dennis, W. M. Yen, S. Kuck, K. Peterman, G. Huber, and W. Jia. Performance of a cr:yag laser. *Quantum Electronics, IEEE Journal of*, 29(9):2508–2512, 1993.

[189] P. J. Conlon, Y. P. Tong, P. M. W. French, J. R. Taylor, and A. V. Shestakov. Passive mode locking and dispersion measurement of a sub-100-fs $Cr4^+$:YAG laser. *Opt. Lett.*, 19(18):1468–1470, 1994.

[190] Y. Ishida and K. Naganuma. Characteristics of femtosecond pulses near 1.5 µm in a self-mode-locked Cr4+:YAG laser. *Opt. Lett.*, 19(23):2003–2005, 1994.

[191] R.Trebino, K. W. DeLong, D. N. Fittinghoff, J. N. Sweetser, M. A. Krumbügel, B. A. Richman, and D. J. Kane. Measuring ultrashort laser pulses in the time-frequency domain using frequency-resolved optical gating. *Review of Scientific Instruments*, 68(9):3277–3295, 1997.

[192] O. E. Martinez, R. L. Fork, and J. P. Gordon. Theory of passively mode-locked lasers including self-phase modulation and group-velocity dispersion. *Opt. Lett.*, 9(5):156–158, 1984.

[193] V. L. Kalashnikov and E. Sorokin. Mode-locked oscillators in the positive and negative dispersion regimes: scenarios of destabilization. 2008.

[194] G.E. Walrafen and Elijah Pugh. Raman combinations and stretching overtones from water, heavy water, and nacl in water at shifts to ca. 7000 cm^{-1}. *Journal of Solution Chemistry*, 33(1):81–97, 2004.

[195] Hayduk M.J., Johns S.T., Krol M.F., Pollock C.R., and Leavitt R.P. Self-starting passively mode-locked tunable femtosecond cr4+:yag laser using a saturable absorber mirror. *Optics Communications*, 137(1):55–58, 1997.

[196] A.V Shestakov, N.I Borodin, V.A Zhitnyuk, A.G Ohrimtchyuk, and V.P Gaponstev. In *Conference on Lasers and Electro-Optics/Quantum Electronics and Laser Science Conference and Photonic Applications Systems Technologies*, volume 10, paper CPDP11. Optical Society of America), 1991.

[197] S.A. Payne, L.L. Chase, Larry K. Smith, Wayne L. Kway, and William F. Krupke. Infrared cross-section measurements for crystals doped with er3+, tm3+, and ho3+. *Quantum Electronics, IEEE Journal of*, 28(11):2619–2630, 1992.

[198] A.A. Lagatsky, S. Calvez, J. A. Gupta, V. E. Kisel, N. V. Kuleshov, C. T. A. Brown, M. D. Dawson, and W. Sibbett. Broadly tunable femtosecond mode-locking in a Tm:KYW laser near 2 μm. *Opt. Express*, 19(10):9995–10000, 2011.

[199] Various. Matbase - the material database online.

[200] X. Mateos, V.Petrov, Junhai Liu, M.C. Pujol, U. Griebner, M. Aguilo, F. Diaz, M. Galan, and G. Viera. Efficient 2 µm Continuous-Wave Laser Oscillation of Tm^{3+} :$KLu(WO_4)_2$. *IEEE Journal of Quantum Electronics*, 42:1008–1015, 2006.

[201] J. Peatross and A. Rundquist. Temporal decorrelation of short laser pulses. *JOSA B*, 15(1):216–222, 1998.

[202] J. W. Nicholson, J. Jasapara, W. Rudolph, F. G. Omenetto, and A. J. Taylor. Full-field characterization of femtosecond pulses by spectrum and cross-correlation measurements. *Opt. Lett.*, 24(23):1774–1776, 1999.

[203] P. Koopmann, R. Peters, K. Petermann, and G. Huber. Crystal growth, spectroscopy, and highly efficient laser operation of thulium-doped lu_2o_3 around 2 µm. *Applied Physics B*, 102(1):19–24, 2011.

[204] C. Fiebig, G. Blume, C. Kaspari, D. Feise, J. Fricke, M. Matalla, W. John, H. Wenzel, K. Paschke, and G. Erbert. 12w high-brightness single-frequency dbr tapered diode laser. *Electronics Letters*, 44(21):1253–1255, 2008.

[205] G. Stibenz and G. Steinmeyer. Interferometric frequency-resolved optical gating. *Opt. Express*, 13(7):2617–2626, 2005.

[206] O. E. Martinez, R. L. Fork, and J. P. Gordon. Theory of passively mode-locked lasers for the case of a nonlinear complex-propagation coefficient. *J. Opt. Soc. Am. B*, 2(5):753–760, 1985.

[207] R Saito, M_ Fujita, G Dresselhaus, and u MS Dresselhaus. Electronic structure of chiral graphene tubules. *Applied Physics Letters*, 60(18):2204–2206, 1992.

[208] Glen A. Slack, D. W. Oliver, R. M. Chrenko, and S. Roberts. Optical absorption of $y_3al_5o_{12}$ from 10- to 55 000-cm^{-1} wave numbers. *Phys. Rev.*, 177:1308–1314, 1969.

[209] Yong-Nian Xu and WY Ching. Electronic structure of yttrium aluminum garnet (y 3 al 5 o 12). *Physical Review B*, 59(16):10530, 1999.

[210] M. Sheik-Bahae, D. C. Hutchings, D. J. Hagan, and E. W. Van Stryland. Dispersion of bound electron nonlinear refraction in solids. *Quantum Electronics, IEEE Journal of*, 27(6):1296–1309, 1991.

[211] A. Cabasse, G. Martel, A. Hideur, and J-L. Oudar. High modulation depth sesam for high power dissipative soliton in an erbium-doped fiber laser. In *CLEO Europe and EQEC 2009 Conference Digest*, page CJ10.5. Optical Society of America, 2009.

[212] A. Gordon, O. Gat, B. Fischer, and F. X. Kärtner. Self-starting of passive mode locking. *Opt. Express*, 14(23):11142–11154, 2006.

[213] D. Welford and M. A. Jaspan. Single-frequency operation of a cr:yag laser from 1332 to 1554 nm. *J. Opt. Soc. Am. B*, 21(12):2137–2141, 2004.

[214] S. Fan, W. Liang, H. Dang, N. Franklin, T. Tombler, M.l Chapline, and H. Dai. Carbon nanotube arrays on silicon substrates and their possible application. *Physica E: Low-dimensional Systems and Nanostructures*, 8(2):179 – 183, 2000.

[215] H. Dai. Carbon nanotubes: opportunities and challenges. *Surface Science*, 500(1?3):218 – 241, 2002.

Danksagung

Hiermit möchte ich folgenden Weggefährten, Kollegen und Freunden danken, die mich die letzten fünf Jahre abschnittsweise bzw. durchgängig begleitet haben:

- ◇ Prof. Dr. Thomas Elsässer für die Möglichkeit diese Dissertation zu schreiben und für seine *Geduld* mit mir,
- ◇ Dr. Uwe Griebner für die Betreuung meiner Promotion, die Hilfe bei fachlichen Problemen und die Korrektur dieser Arbeit,
- ◇ Dr. Günter Steinmeyer für seine Aufklärung messtechnischer Fragestellungen, die Korrektur dieser Arbeit und die *zugeworfenen* Fachbbegriffe beim *Theorie-Ping-Pong*,
- ◇ Dr. Martin Bock, der sowohl als Freund, als auch als Studien-, und Arbeitskollege durch nichts in der Welt ersetzbar wäre,
- ◇ Dr. Martin Hempel für die Korrektur meiner Arbeit, die er mit akribischem Blick auf Feinheiten in Angriff nahm, und für den Austausch bei *Babyfragen*,
- ◇ Dr. Valentin Petrov, der auch noch spät abends bereit ist, seine *hands-on* Fähigkeiten zur Verfügung zu stellen,
- ◇ allen Kollegen der Abteilung C2, darunter u.a. *Cabriolege* Dr. Bastian Borchers, der jetzt bei Coherent sein *Unwesen* treibt und Simon Birkholz,
- ◇ Simon Rivier, der bei meinem Start am MBI gerne dazu bereit war Know-How aus seinem Fundus an Laborerfahrung zu teilen,
- ◇ sowie allen Angestellten des MBI, die für den laufenden Betrieb sorgen, wie z.B. die EDV, die Betriebstechnik und die Sekretariate.

Ferner gilt mein Dank all jenen Wissenschaftlern, mit denen ich am MBI oder bei Forschungsaufenthalten zusammenarbeiten durfte: Francesc Díaz, Xavier Mateos, Martha Segura, Maria-Cinta Pujol, Julien LeClech, Mauro Tonelli, Daniela Parisi, Stefano Veronesi, Samuele Di Dio Cafiso, Elena Ugolotti, Akira Yoshida, Fabian Rotermund und Won-Bae Cho. Vor allem letzterer beschert mir ein lachendes Auge ob seiner Bekanntschaft und ein weinendes Auge, weil Südkorea so verdammt weit weg ist. Euch allen muchas gracias, merci beaucoup, molte grazie, ありがとう und 감사합니다.

Last but not least möchte ich meiner eigenen kleinen Familie

Lydia und Isabel

von Herzen für ihre stete Unterstützung danken.